



**MSc in Physics**

# **Microlensing by dark substructure**

**- At high optical depth**

**Rasmus Staugaard Thomsen**

Supervised by Oleg Ruchayskiy

**August 2024**



**Rasmus Staugaard Thomsen**

*Microlensing by dark substructure*

MSc in Physics, August 2024

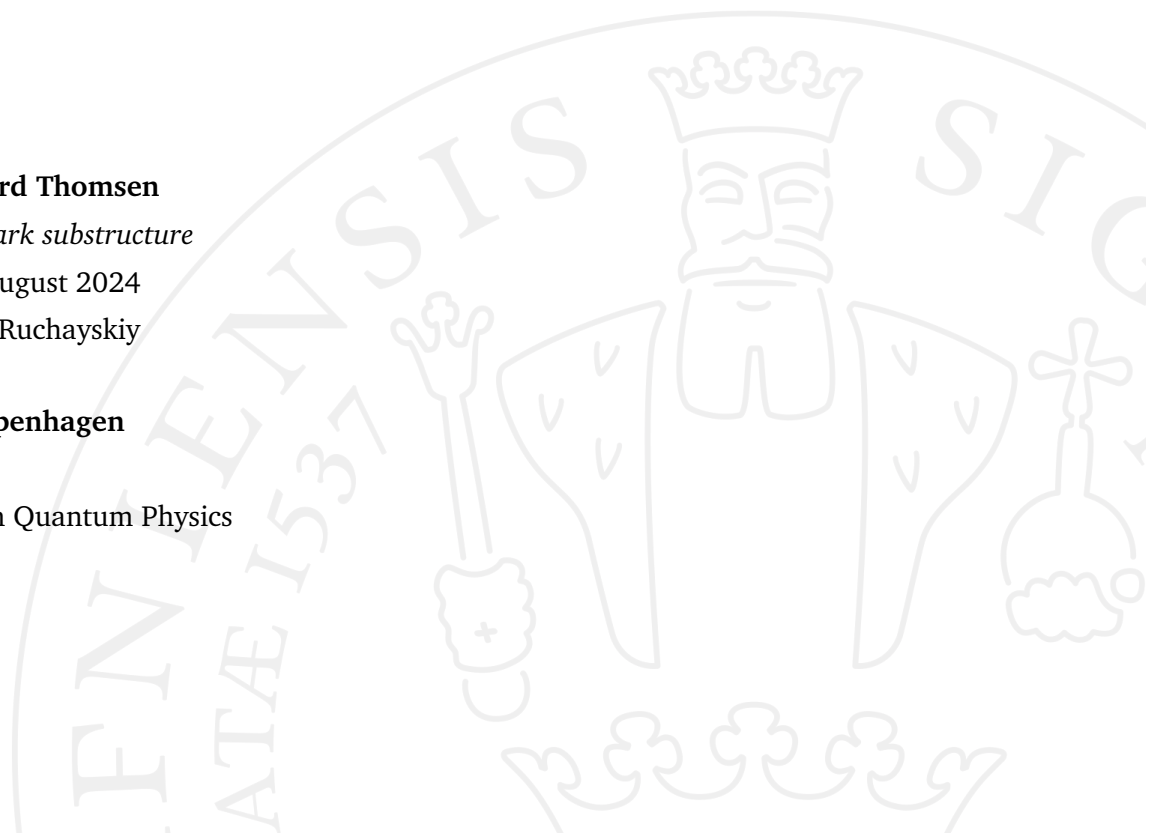
Supervisor: Oleg Ruchayskiy

**University of Copenhagen**

*Faculty of Science*

Masters Degree in Quantum Physics

Copenhagen



# Acknowledgements

First and foremost I would like to thank my principal supervisor, Oleg Ruchayskiy, for his immense help and support. We had many great discussions during the project and although they sometimes went in many different directions, I think we converged on something interesting at the end. As he remarked at one of the meetings, this project was much like a random walk both in essence and material. I had many doubts about the project, and myself, throughout, but I really appreciated Oleg's steadfast support in my work. His encouragement gave me the confidence to finish the project.

Next, I would also like to thank Johan Samsing from NBIA. Even though we only talked a couple of times, I appreciate his openness and willingness to spend some time talking about this project with me.

On a very personal note, I would also like to thank my friends and family. Without them, I would have never been able to start and eventually hand in this thesis. I have gotten a lot of support from some very special people and it means the world to me. Things were looking quite bleak at times last fall and I can only thank them for bringing me to a better place.

Finally, although she never got to see it, I would like to thank my mother for everything. I know she would have been proud of me regardless of my work.

# Abstract

Dark matter is a mysterious form of matter that does not interact electromagnetically making it invisible to most modern observational probes. According to our modern understanding, it plays a crucial role in the expansion of the Universe and the formation of structure. In particular, all galaxies and galaxy clusters are thought to reside within dark matter halos, which provide the dominant contribution to their mass. While dark matter is recognized to have a significant impact on our Universe, its microscopic properties remain largely unknown. It is however well established that none of the known elementary particles can account for the majority of dark matter. Consequently, the dark matter hypothesis suggests the existence of new, yet-discovered particles. Little is still known about the properties of these hypothetical particles.

One of the few model-independent characteristics of dark matter relates to their primordial velocities. If the particles were ever relativistic in the early Universe, such models are referred to as 'warm dark matter' (WDM). In contrast, dark matter particles that were produced in a non-relativistic state are known as 'cold dark matter' (CDM). This characteristic has significant implications for structure formation as a whole. Specifically, this distinction leads to differing predictions for sub-galactic structures between CDM and WDM models. As the Universe's structure forms hierarchically under gravitational influence — small collapsed structures merging to form larger ones — each galaxy or galaxy cluster is anticipated to host numerous dark substructures of varying masses. The distribution of these structures over masses remains a subject of active debate within the cosmological community. Consequently, measuring these properties could provide a way to differentiate between particle physics models of warm and cold dark matter.

In this thesis, I propose novel methods for searching for such structures, namely, utilizing microlensing at high optical depth. Microlensing refers to the bending of light from a distant star or quasar by a compact object, such as a star or a dark matter clump, leading to a temporary magnification of the background source. This phenomenon is

particularly effective for detecting compact objects, as it does not rely on the emission of light from the lensing object itself. This makes it an ideal tool for probing dark matter substructures. Particularly, in high-optical depth microlensing, the gravitational interaction of many objects plays a role in the light's deflection. This can possibly lead to fluctuations in the magnification of a source. While numerous studies have investigated high-optical depth microlensing by stars, there has been significantly less research on high-optical depth microlensing by substructure. We therefore try to adapt an existing model for high-optical depth microlensing, referred to as 'The random star-field model' in literature, to microlensing by substructure. Another formalism is also developed utilizing a ratio distribution to devise the probability of scattering. This new formalism reveals that discreteness effects likely impose an effective upper limit on the masses involved in microlensing. Despite this limit, adapting the 'random-star field model' to dark matter subhalos indicates that their microlensing effects are considerably greater than that of stars. This suggests further research into high-optical depth microlensing by dark substructure might be warranted. Although our models indicate that microlensing is primarily influenced by the largest masses, a conclusion that has also been reached in other inquiries, it is also found that if the subhalos are not distributed uniformly around the line-of-sight, then this may potentially lead to a small dependence on the lower mass bound.

# Contents

<b>0</b>	<b>Introduction</b>	<b>1</b>
<b>1</b>	<b>Cosmology</b>	<b>3</b>
1.1	The early universe . . . . .	3
1.1.1	FLRW metric . . . . .	3
1.1.2	The Hot Big Bang and cosmic relics . . . . .	6
1.2	Structure formation . . . . .	11
1.2.1	Fluid equations . . . . .	11
1.2.2	Linear perturbation . . . . .	14
1.2.3	The transfer function and the power spectrum . . . . .	19
1.3	Dark matter . . . . .	21
1.3.1	Dark matter evidence . . . . .	22
1.3.2	Particle dark matter . . . . .	23
1.3.3	The CDM and WDM paradigm . . . . .	26
<b>2</b>	<b>Gravitational lensing</b>	<b>29</b>
2.1	A general relativistic approach . . . . .	30
2.2	The lens equation . . . . .	34
2.2.1	Point mass lens . . . . .	36
2.2.2	Magnification . . . . .	39
2.3	The dominant lens approximation . . . . .	40
<b>3</b>	<b>Microlensing</b>	<b>43</b>
3.1	The random star-field . . . . .	44
3.1.1	Holtmark–Markov method . . . . .	45
3.1.2	The characteristic function of a single scattering . . . . .	45
3.1.3	Probability distribution of scattering angle after N-deflections . . . . .	48
3.1.4	Introducing a mass spectrum . . . . .	50
3.2	Surface brightness distribution . . . . .	52
<b>4</b>	<b>Substructure Microlensing</b>	<b>56</b>

4.1	Mass spectrum considerations . . . . .	57
4.1.1	A new formalism for stochastic scattering . . . . .	59
4.1.2	The non-Gaussian behaviour for small $N$ . . . . .	62
4.1.3	The high $N$ -behaviour . . . . .	64
4.2	Non-uniformity of impact parameter distribution . . . . .	66
4.3	An order of magnitude estimation of substructure microlensing . . . . .	69
<b>5</b>	<b>Discussion and outlook</b>	<b>71</b>
<b>6</b>	<b>Appendix</b>	<b>74</b>
6.1	The ratio-distribution deflection function for any $N$ . . . . .	74
6.2	Extended substructure lensing . . . . .	75
6.2.1	Fourier transform . . . . .	76
6.2.2	Probability density function for $N$ -deflections . . . . .	77
<b>7</b>	<b>Bibliography</b>	<b>78</b>

# Introduction

Dark matter remains one of the most puzzling pieces of modern physics. While many models of dark matter currently exist it remains very difficult to gain experimental evidence, which favours a particular model. This provides a strong incentive to develop new methods for probing dark matter models or identifying areas where the models differ in their predictions. Particle dark matter models can broadly be separated into two distinct classes. They are known as respectively warm dark matter (WDM) and cold dark matter (CDM) and are differentiated by their behavior during the early universe. Although both types of dark matter have been considered, CDM models are historically more favored by cosmologists due to their initial success. The current standard model of cosmology called  $\Lambda$ CDM, is also based on cold dark matter particles. Warm dark matter however still remains a very real possibility and it can potentially also explain a few discrepancies in CDM models [37]. For this reason, it is of great importance in dark matter research to find ways to test, whether CDM or WDM models best fit with our Universe. The distinct behavior of CDM and WDM particles in the early universe influences the formation of structure. Specifically, this leads to varying predictions regarding the amount of sub-galactic substructure. The initial section on cosmology aims to give an overview of why this is the case. It simultaneously also covers any background material in cosmology deemed relevant for the rest of the thesis. For any person well-acquainted with cosmology, I recommend skipping Section 1.1. It is mostly there for completeness' sake and is likely prior knowledge. The following sections on structure formation and dark matter are, however, important motivations for the main investigation of this thesis. These sections culminate in an explanation of the predictable differences between cold and warm dark matter models. As mentioned the distinctions between these models' predictions become apparent, when looking at sub-galactic substructures. Any probe of such substructure could therefore shed light on which models are worth considering.

The most obvious direct probe of dark substructure is gravitational lensing. Consequently, the primary focus of this thesis was to investigate whether the cumulative gravitational effects of substructure could be detected using gravitational lensing. Over the course of the project, it became apparent that the subset of gravitational lensing known as microlensing might present an avenue to find such a probe. As the reader might not be



familiar with either gravitational lensing or microlensing, the second section concerns itself with the general formalism of gravitational lensing. It starts off with a derivation heavily inspired by Carroll [8] motivating how general relativity leads to the bending of light and gravitational lensing. After this, the basic theory of gravitational lensing is introduced, particularly with the main aim of motivating microlensing. Microlensing explores how the gravitational lens affects the surface brightness of a source. It generally is divided into a low-optical depth regime, where only one object along the line-of-sight participates in the lensing, and a high-optical depth regime, where the influence of many objects is felt and must be taken into account. As such, we turned towards the high-optical depth microlensing as a possibly interesting probe of substructure.

While we do not work with a very concrete lens model, a phenomenological model of microlensing, sometimes referred to as 'The random star-field model' was devised by Katz *et al.* [21]. This is therefore the focus of the the third chapter. The chapter seeks to clarify and extend the original derivation presented in Katz *et al.* [21]. In Section 3.2, the ideas of a related paper by Deguchi and Watson [12] are presented. These concern how one might actually observe high-optical depth microlensing of a source by looking at the moments of its surface brightness distribution.

Finally, the fourth chapter is comprised of original work. Most articles concerning high-optical depth microlensing are about how stars in a galaxy might affect the lens system. We instead consider this effect in the case of microlensing by dark matter subhalos. This is done by trying to adapt the random star-field models for subhalos. When modifying the random star-field for subhalos, several factors need to be considered. Notably, the broad and steep mass spectrum of dark matter subhalos is a significant consideration, as it likely cannot be directly incorporated into the model. This is looked at in Section 4.1, where a new formalism, similar to Katz *et al.* [21] is developed to address this problem. In Section 4.2, the assumption of a uniform distribution of subhalos is examined. Deviations from this assumption could introduce novel effects. Lastly, Section 4.3 provides an order-of-magnitude estimate for substructure microlensing based on the considerations from Section 4.1.

# Cosmology

## 1.1 The early universe

Contemporary cosmology has largely been founded on the cosmological principle. This principle asserts that on the largest scales, the universe has two key spatial properties (See e.g. [8, Chap. 8] or [19, Chap. 4]):

- **Homogeneity:** Every point in the considered space shares the same geometric characteristics. This implies the space is invariant under spatial translations.
- **Isotropy:** Given a point  $x^i$  in the space, it is said to be isotropic, if the space looks the same in every direction from this point. This implies that the space is spherically symmetric around this point.

Combining these properties implies that if we have a cosmological clock that parametrizes the evolution of the universe,  $t_{\text{cos}}$ , then at every time slice of  $t_{\text{cos}}$ , the cosmological principle would dictate that the universe should be spherically symmetric around every point. It is quite obvious that these assumptions do not hold on smaller scales, as we intuitively already know that there, for instance, is a large difference between being in a galaxy or a void. However, this description turns out to be very valid on the largest scales, as local variations in density are averaged over. This is best exemplified in measurements of the cosmic microwave background (CMB), which is incredibly smooth and uniform, up to a factor of  $10^{-5}$  from the mean density [8]. Such a description is therefore very adequate when describing the early universe and while structure formation introduces local inhomogeneities later on, then these cannot be seen on the largest scale.

### 1.1.1 FLRW metric

According to general relativity, the metric tensor  $g_{\mu\nu}$  defines the geometry of spacetime. Determining the metric of the universe on the largest scales will thus provide insights into the geometry of the universe and how it is influenced by its content. The cosmological

principle, which assumes spatial homogeneity and isotropy, significantly restricts the permissible forms of the metric tensor, as it must satisfy these symmetry requirements. In particular, symmetry arguments can be utilized to argue that the spatial part of the metric must be described by the metric of a maximally symmetric space. Such a maximally symmetric space, in three dimensions, takes the form [8]:

$$d\sigma^2 = \frac{dr^2}{1 - kr^2} + r^2 d\Omega^2, \quad (1.1.1)$$

where  $k \in \{-1, 0, 1\}$  is the curvature of the three dimensional space. The three different values of  $k$  correspond to three distinct types of spaces. For  $k = -1$ , the space is hyperbolic (open), for  $k = 0$ , it is a flat Euclidean space, and for  $k = 1$ , it is a spherical (closed) space. If this is to be extended to 4-dimensional spacetime, then since this metric is only valid for constant time slices,  $t_{\text{cos}} = \text{const.}$ , the spatial entries in the metric could also depend on a function of time,  $a(t)$ , referred to as the scale factor. In terms of the temporal and mixed components of the metric tensor, isotropy and homogeneity immediately implies that  $g_{ti} = 0$  and  $g_{tt} = f(t)$ .  $g_{ti}$  must be equal to zero because otherwise there would be a preferred direction in the universe thereby contradicting isotropy. Whereas  $g_{tt}$  can only be a function of time because of homogeneity. Finally, by redefining the time coordinate one can choose it such that  $g_{tt} = -1$ . This would therefore fix the metric as:

$$ds^2 = -dt^2 + a(t)^2 \left[ \frac{dr^2}{1 - kr^2} + r^2 d\Omega^2 \right]. \quad (1.1.2)$$

The usual ten independent components of the metric have in this way been reduced to only one function of time,  $a(t)$  and a free parameter  $k$ . An important distinction of this new coordinate system is the fact that  $r$  is no longer the physical radial distance. Instead, it is known as the co-moving distance. The physical distance,  $x = a(t)r$ , will depend on the scale factor, whereas the co-moving distance between two objects will be independent of the value of the scale factor.

In order to resolve the dynamics of the universe, general relativity requires us to solve the Einstein field equations:

$$G_{\mu\nu} = 8\pi G T_{\mu\nu}. \quad (1.1.3)$$

The Einstein field equations describe how the energy-momentum content of the universe curve spacetime. Consequently, they will explain how the scale factor,  $a(t)$ , depends on the content of the universe. On the largest scales, the energy-momentum tensor can be modelled after a perfect fluid [5][19]:

$$T_{\nu}^{\mu} = (\rho + P)U^{\mu}U_{\nu} - P\delta_{\nu}^{\mu}. \quad (1.1.4)$$

As the average matter is at rest,  $U^\mu = (1, 0, 0, 0)$ , according to our main assumptions of homogeneity and isotropy, then this turns out to be a valid description of the content of the universe. Since the energy-momentum tensor is conserved in general relativity, the particular form of (1.1.4) can be used to derive the equation for the conservation of energy:

$$\frac{\dot{\rho}}{\rho} = -3\frac{\dot{a}}{a}(\rho + P). \quad (1.1.5)$$

This equation together with the equations of state for various fluid species can be

	Scale factor dependence
Radiation	$a^{-4}$
Matter / Dark matter	$a^{-3}$
Dark energy	$a^0$

**Table 1.1:** Energy density dependence on the scale factor for various fluids.

used to establish a relationship between the energy density and the scale factor for the considered fluid. In general, it can be shown to follow the pattern  $\rho \propto a^{3(1+w)}$  and is summarized in the table (see Tab. 1.1). Interestingly, for an expanding universe, the matter and radiation energy density will be diluted, as the universe becomes older and their dilution is different. This has huge implications for the thermal history of the universe, which will be considered in the next subsection.

Apart from finding the energy density dependence on the scale factor, using (1.1.4) as the source term for the Einstein tensor,  $G_{\mu\nu}$ , leads to the two Friedmann equations [8]:

$$H^2 = \frac{8\pi G}{3} \sum_i \rho_i - \frac{k}{a^2}, \quad (1.1.6)$$

$$\dot{H} = -4\pi G \sum_i (1 + w_i) \rho_i, \quad (1.1.7)$$

where  $H = \frac{\dot{a}}{a}$  is the Hubble parameter and  $w_i$  is the equation of state proportionality constant for the specific fluid. These equations describe how the scale factor evolves in time depending on the current content of the universe. Assuming  $k = 0$ , which observational evidence suggests is the most likely geometry of the universe [1], the first Friedmann equation in this case indicates that  $H > 0$ . This suggests that the universe will be ever-expanding. Exactly how fast the expansion of the universe is, will however depend on the energy content of the universe. On the other hand, the second Friedmann equation indicates that  $\dot{H} \leq 0$ , so the Hubble parameter will never increase with time. A particularly interesting scenario is when the universe is totally dominated by dark matter  $\rho_{\text{tot}} \sim \rho_\Lambda$ , as this will happen eventually in an ever expanding universe, according to the scale factor dependence in (see Tab. 1.1). In this case, the second Friedmann equation

Dominant component	Time dependence
Radiation	$t^{\frac{1}{2}}$
Matter / Dark matter	$t^{\frac{3}{2}}$
Dark energy	$\exp(H_{\Lambda}t)$

**Table 1.2:** The time dependence of the scale factor in universes dominated by various components.

is  $\dot{H} = 0$ , which will turn out to yield an exponential scale factor. This indicates that the future expansion of our universe will be exponential. The behaviour of the scale factor in universes dominated by various components is summarized in (see Tab. 1.2).

A quick consequence of the expansion of the universe is the fact that distant sources of radiation will gradually redshift [5]. This can be seen as a sort of Doppler effect, where, due to the expansion of the universe, the source emitting light will move further away from the observer during its emission. The redshift can be related to the scale factor:

$$1 + z = \frac{1}{a(t)}. \quad (1.1.8)$$

It is often more convenient to parameterize the evolution of the universe in terms of this redshift scale. In this case,  $z = 0$  is the universe at the present day, while as  $z \rightarrow \infty$  we would be going back to the beginning of the universe.

### 1.1.2 The Hot Big Bang and cosmic relics

The Hot Big Bang model describes the early universe as an extremely hot and dense mixture of energy and particles (See D. Baumann [5, Chap. 3]). Within this thermal bath, consisting mainly of photons and light fermions, every particle rapidly reached thermodynamic equilibrium. According to thermodynamics, every particle species may therefore be described by macroscopic quantities such as their temperature  $T_i$ , entropy  $S_i$ , and chemical potential  $\mu_i$ . Since almost all particle species in the Standard Model interact via the weak interaction, they will initially all be in the same equilibrium, as they all interact, at least indirectly, with each other. This means in particular that the temperature and the chemical potential of all the individual particle species must be equal to that of the thermal bath. However, as the universe expands energy will be dispersed and so the temperature of the thermal bath gradually decreases. This will eventually mean that some particle species will end up no longer being in equilibrium with the thermal bath. This decoupling from equilibrium, referred to as 'freeze-out',

happens at different times for the various species and, in some cases, leaves behind certain imprints on the universe called cosmic relics. These cosmic relics are still observable to this day and are some of the main evidence for the Hot Big Bang model. They include the cosmic microwave background, the cosmic neutrino background and the abundance of Hydrogen and Helium in our universe.

To understand this decoupling mechanism, we imagine some particle physics process with interaction rate  $\Gamma = n\sigma v$ . From the previous section, we know the rate of expansion of the universe can be described by the Hubble parameter,  $H$ . The relative ratio  $\frac{\Gamma}{H}$  will then describe whether or not a process is in equilibrium. A process can in this case be described as being in equilibrium<sup>1</sup> as long as  $\frac{\Gamma}{H} \gg 1$  since this would indicate that the process happens many times before the universe has a chance to expand further. However, when  $\frac{\Gamma}{H} \sim 1$  the process decouples from the thermal bath. Once all processes that used to allow a particular particle species to interact with the thermal bath have ceased, the particle species will undergo freeze-out. As a result, its macroscopic thermodynamic quantities will no longer be forced to match those of the thermal bath. The mechanism itself can be described by tracking the number density of one of the interacting particles. For a non-interacting (stable) particle it is clear that its co-moving number density is conserved since it cannot be created nor destroyed. This can be thought of as a continuity equation and is the statement [5][23]:

$$\frac{1}{a^3} \frac{d(n(t)a^3)}{dt} = 0 \iff \frac{dn(t)}{dt} + 3H(t)n(t) = 0. \quad (1.1.9)$$

Adding in interaction terms would in this case correspond to adding a source term and it allows the co-moving number density to change. For a two-particle interaction ( $1 + 2 \leftrightarrow 3 + 4$ ) this statement may be written:

$$\frac{dn_1}{dt} + 3H(t)n_1 = -\Gamma n_1 \left[ 1 - \left( \frac{n_1 n_2}{n_3 n_4} \right)_{\text{eq}} \left( \frac{n_3 n_4}{n_1 n_2} \right) \right], \quad (1.1.10)$$

where if the right-hand side was zero the number density would be constant. The right hand side has exactly an annihilation term ( $\propto -n_1 \Gamma$ ) and a production term ( $\propto n_1 c_{\text{eq}} \left( \frac{n_3 n_4}{n_1 n_2} \right) \Gamma$ ). While the process is in equilibrium ( $\Gamma \gg H$ ), the above expression will tend toward the equilibrium values, since if  $\left( \frac{n_1 n_2}{n_3 n_4} \right) > \left( \frac{n_1 n_2}{n_3 n_4} \right)_{\text{eq}}$  then the annihilation terms dominates, while when  $\left( \frac{n_1 n_2}{n_3 n_4} \right) < \left( \frac{n_1 n_2}{n_3 n_4} \right)_{\text{eq}}$  the production term dominates. However, once the equilibrium is eventually disrupted and freeze-out occurs ( $H \gg \Gamma$ ), then the

---

<sup>1</sup>Formally equilibrium is described as a limit, where the process has occurred an infinite amount of times. It is, however, a very good approximation as long as the process has occurred an number of times  $N \gtrsim N_A$

right-hand side may completely be ignored, resulting in a constant co-moving number density.

With the above picture in mind, it then becomes very important to understand how the ratio  $\frac{\Gamma}{H}$  changes. As temperature drops this happens in quite a few ways, as both changes in  $\Gamma$  and  $H$  occur.  $H$  can be described as only depending on  $\rho_r$ . This is because of the relative suppression of non-relativistic particles in the early universe. This 'Boltzmann suppression' happens, because the distribution function behaves differently for relativistic and non-relativistic particles. While the distribution function  $f$  in general is a function of phase-space variables  $\vec{x}, \vec{p}$  and  $t$ , then due to the assumptions of homogeneity and isotropy in the early universe, then it can only depend on  $f(p, t)$ . If the time dependence is left implicit, then this means  $f(p)$  is completely determined for both fermions and bosons as resp. the Fermi-Dirac and the Bose-Einstein distributions:

$$f(p) = \begin{cases} \frac{1}{\exp(\frac{E-\mu}{T})-1} & \text{Bosons} \\ \frac{1}{\exp(\frac{E-\mu}{T})+1} & \text{Fermions.} \end{cases} \quad (1.1.11)$$

As is well known from statistical mechanics, these two distributions coincide with the Maxwell-Boltzmann distribution, when  $E - \mu \gg T$ . As the distribution function is akin to the density of the phase space, then it can be used to calculate various thermodynamic quantities including  $n(T)$ ,  $\rho(T)$  and  $P(T)$ . The argument of 'Boltzmann suppression' can be presented by looking at the number density [5]:

$$n(T) \propto \begin{cases} T^3 & \text{Relativistic} \\ T^{\frac{3}{2}} \exp(-\frac{m}{T}) & \text{Non-relativistic} \end{cases}. \quad (1.1.12)$$

When the temperature of the thermal bath drops below the mass of a heavier particle, that particle becomes non-relativistic. In this situation, if a non-relativistic particle is in equilibrium with a relativistic particle, the equilibrium will be significantly skewed towards the relativistic particle. The equation (1.1.12) suggests that the non-relativistic particle will be exponentially suppressed. Physically, this occurs because the thermal bath starts lacking the energy to pair-produce the heavier particles, thereby greatly reducing their production rate. This means the expansion of the universe can, in the early universe, be considered to be completely dominated by radiation. It can therefore reasonably be asserted that  $H$  should behave as:

$$H \sim \left( \frac{8\pi G}{3} \rho_r \right)^{\frac{1}{2}} = \frac{\pi}{3} \left( \frac{g_*}{10} \right)^{\frac{1}{2}} \frac{T^2}{M_{\text{Pl}}}, \quad (1.1.13)$$

where  $g_*$  is the effective number of degrees of freedom for all relativistic species in equilibrium. The variation in  $\Gamma$  is more complicated as it is very dependent on the type of process. For weak interaction processes, which are mediated by massive gauge bosons, the interaction strength decreases once the gauge bosons can no longer be considered fully relativistic. The cross-section for weak interactions, at energies  $s \lesssim M_W$ , can be argued to be proportional to  $\sigma = G_F^2 T^2$  using dimensional analysis, where  $G_F$  is the fermi-constant. In this case, the decoupling would be expected to occur around:

$$\frac{\Gamma}{H} \sim G_F^2 M_{\text{Pl}} T^3 = \left( \frac{T}{1\text{MeV}} \right)^3 \implies T_{\text{Dec}} = 1\text{MeV}. \quad (1.1.14)$$

Therefore, particles that interact only weakly are expected to decouple from the thermal bath at around  $T \sim 1\text{MeV}$ . Interestingly, since  $H$  is dependent on  $g_*$ , then this decoupling temperature is partly determined by the number of relativistic species still in equilibrium. This is very important since it will turn out to put bounds on beyond standard model physics. The only stable particle that solely reacts weakly is the neutrino. The decoupling of the weak force, therefore implies that one would expect to be able to find relic neutrinos with their temperature determined by this decoupling temperature. This point will be returned to shortly.

Due to the conservation of both energy and entropy, the decoupling of species turns out to have an important effect on the thermal bath. As the energy and entropy of non-relativistic species can largely be ignored (again due to the temperature dependence of the number density) then the decoupled species must transfer most of their energy and entropy back to the thermal bath when decoupling. Particularly, the energy and entropy densities are [5]:

$$\rho_r = \sum_i \rho_{r,i} = \frac{\pi^2}{30} g_*(T) T^4 \quad (1.1.15)$$

$$s_r = \sum_i s_{r,i} = \frac{2\pi^2}{45} g_{*S}(T) T^3, \quad (1.1.16)$$

where  $g_*$  and  $g_{*S}$  are the effective number of relativistic species. They are temperature-dependent due to the eventual decoupling of different species, which would make the effective numbers smaller. Since these quantities are densities they are *not* conserved. The co-moving entropy is however conserved  $s_r a^3 = \text{const.}$  as the expansion of the universe can be taken to be adiabatic in the early universe. This implies that for the most part, the relation  $T \propto a^{-1}$  holds, however when a relativistic species decouples, then  $g_{*S}(T)$  becomes smaller and so in order for the co-moving entropy to remain constant,



then the temperature must go up resulting in a slightly slower temperature decay than  $T \propto a^{-1}$ .

For the previous example of neutrinos, this means that once they decouple their temperature will behave like  $T \propto a^{-1}$ , as they will still be relativistic. This is the exact behaviour of the thermal bath, which would exclusively consist of photons and the lightest fermions (e.g.  $e^-$ ,  $e^+$ ) at this point. However, eventually, the light fermions will also decouple, which heats the remaining photons. The photons themselves will continue to interact with matter until protons and electrons come together to form neutral hydrogen. This event is referred to as 'recombination' and happens around  $z = 1100$ . After this event, the leftover photons will freeze out. These relic photons are expected to have a slightly higher temperature than the relic neutrinos, due to them being reheated by the decoupling of the light fermions. Today the relic photons are typically referred to as the cosmic microwave background (CMB), as they have redshifted into the microwave part of the electromagnetic spectrum. The hot Big Bang model therefore predicts the existence of the cosmic microwave background and the neutrino cosmic background. The CMB has been experimentally verified with a temperature of  $T_\gamma = 2.73K$  following a near-perfect black body spectrum. It is among the most convincing arguments for the hot Big Bang [5]. While only indirect evidence exists of the neutrino cosmic background, in the form of measurements of  $\rho_r$ , it is also a major prediction of the model. In particular, it is expected to have a temperature related to the CMB,  $\frac{T_\nu}{T_\gamma} = (4/11)^{\frac{1}{3}}$ .

When the weak force decouples, then neutrons and protons are also expected to exit equilibrium with each other. This means in particular that their ratio can be determined at freeze-out as:

$$\frac{n_n(T_{\text{Dec}})}{n_p(T_{\text{Dec}})} = \left(\frac{m_n}{m_p}\right) \exp\left(-\frac{(m_n - m_p)}{T_{\text{Dec}}}\right). \quad (1.1.17)$$

The ratio of protons to neutrons is important in Big Bang Nucleosynthesis — the theory of how the lightest elements came to be — as neutrons are eventually fused with other baryons to make helium. The ratio of hydrogen to helium is predicted by Big Bang Nucleosynthesis to be around  $\frac{1}{16}$ , which is consistent with current observations [5]. This ratio is in particular very influenced by the decoupling temperature and the decoupling temperature is in turn sensitive to changes in  $g_*$ . In this way, the introduction of new particles can end up distorting the current ratio. Results from Big Bang Nucleosynthesis therefore pose very relevant constraints for potential dark matter particles.

## 1.2 Structure formation

Until now we have assumed the early universe to be homogeneous and isotropic. However, as is evident by measurements today, this assumption is only applicable on the largest scales. Therefore, there must exist a mechanism whereby local inhomogeneities grow larger during the evolution of the universe. This turns out to be a consequence of the 'tug-of-war' happening between gravity, which tries to pull matter together, and the expansion of the universe, which tries to pull matter away. Locally, gravity wins this battle resulting in pockets of higher matter density, but also pockets of lower matter density since matter has been removed from these regions. While globally it is the expansion that remains the victor, forcing the pockets of matter to be separated.

Although measurements of the CMB indicate a very uniform early universe, there are observed small inhomogeneities on the order of  $\delta \sim 10^{-5}$  from the mean density  $\bar{\rho}$ . These small inhomogeneities are thought to come from quantum fluctuations from when the universe just came into being. The process of inflation — a short period of very accelerated expansion — is conjectured to have separated these fluctuations causing the inhomogeneities in the CMB. Since inflation is a complicated subject and not immediately necessary for the work in this thesis, it will not be further explored. It should however be mentioned that it stands on very solid theoretical grounds, as it is currently the most comprehensive way to explain several other mysteries in the early universe, including the flatness problem and the horizon problem [5, See e.g. Chap. 2].

### 1.2.1 Fluid equations

While a completely satisfying theory of structure formation has to be done in the framework of general relativity, we can come a long way by just considering Newtonian gravity. This is because, in the case of non-relativistic matter (i.e. dark matter and baryons after decoupling), Newtonian perturbation theory gives a decent description of structure formation on smaller scales (See D. Baumann [5, Chap. 4] and D. Tong [36]). Structure formation is largely based on the field of fluid mechanics. As a good approximation, all the (non-relativistic) matter in the universe can be described as being collisionless with its primary energy content stemming from the energy density of the

matter ( $\rho \gg P$ ). The dynamics of such a fluid can then be described by the following three equations:

$$\textbf{Continuity Equation: } \partial_t \rho + \nabla \cdot (\rho \vec{u}) = 0 \quad (1.2.1)$$

$$\textbf{Euler Equation: } (\partial_t + \vec{u} \cdot \nabla) \vec{u} = \frac{-\nabla P}{\rho} - \nabla \Phi \quad (1.2.2)$$

$$\textbf{Poisson Equation: } \nabla^2 \Phi = 4\pi G \rho \quad (1.2.3)$$

where  $\vec{u}(x, t)$  is the velocity of the fluid,  $\rho(x, t)$  is the mass density and  $P(x, t)$  is the pressure. The Poisson equation should be familiar to anyone, who has studied Newtonian gravity. It tells how a mass distribution gives rise to a gravitational field. To understand where the first two equations come from, let's take a short look at them individually.

### Continuity equation:

In essence, the continuity equation tells that mass is conserved. This means the only way for mass to change in a given region is if it simultaneously disappears from some other region (See [15, Chap. 9]). To see this, let's imagine a cylindrical tube with cross-sectional area  $d\vec{A}$ . The amount of mass flowing out through this area during a time  $\Delta t$  is  $-\Delta t \int_A d\vec{A} \cdot \vec{u}(x, t) \rho(x, t)$ . This means we can write the instantaneous change as:

$$\frac{dm}{dt} = - \int_A d\vec{A} \cdot \vec{u}(x, t) \rho(x, t) = - \int_V d^3x \nabla \cdot (\rho \vec{u}(x, t)), \quad (1.2.4)$$

where in the final step the divergence theorem was used. The mass change can also be written as:

$$\frac{dm}{dt} = \frac{d}{dt} \int_V d^3x \rho(x, t) = \int_V d^3x \frac{\partial}{\partial t} \rho(x, t), \quad (1.2.5)$$

where we have differentiated under the integral<sup>2</sup>. Combining (1.2.4) and (1.2.5) gives the continuity equation:

$$\int_V d^3x \left[ \partial_t \rho(x, t) + \nabla \cdot (\rho(x, t) \vec{u}(x, t)) \right] = 0, \quad (1.2.6)$$

as the integrand must be zero in order to ensure this relation holds.

### Euler equation:

The Euler equation is a bit more complex. We again consider some fluid flowing through a cylindrical tube. The Euler equation tells about the conservation of momentum in this fluid. Changes in momentum can however come from a few different sources. First, there can be an external force that acts upon the fluid and subsequently changes its

---

<sup>2</sup>This is at the very least correct, if the considered time interval is infinitesimal

momentum. This change can be written as  $-\Delta t \int_V d^3x \rho (\nabla \Phi)_i$ ,  $i = 1, 2, 3$ , where  $(\nabla \Phi)_i$  is the force per unit mass. The pressure from the surrounding medium also impacts the momentum, this time by a factor  $-\Delta t \int_A dA_i P$ . Finally, as in the case of the continuity equation, the momentum might also flow in a given direction, this is referred to as the convective flow. The corresponding change of momentum reflects that from the continuity equation  $-\Delta t \int_A d\vec{A} \cdot \vec{v} \rho v_i$ . Again the total change of momentum can be written [15]:

$$\frac{dp_i}{dt} = - \int_V d^3x \rho (\nabla \Phi)_i - \int_A dA_i P - \int_A d\vec{A} \cdot \vec{v} \rho v_i. \quad (1.2.7)$$

It can be written in a more compact form by introducing the stress tensor,  $T_{ij} = P\delta_{ij} + \rho v_i v_j$ :

$$\frac{dp_i}{dt} = - \int_V d^3x \rho (\nabla \Phi)_i - \int_A dA_i T_{ij}. \quad (1.2.8)$$

Using the divergence theorem on the surface integral term and arguing that  $\frac{dp_i}{dt}$  can be written similarly as (1.2.5), but with  $\rho$  replaced by  $\rho v_i$ , we get:

$$\int_V d^3x \left[ \partial_t (\rho v_i) + \partial_j T_{ij} - \rho (\nabla \Phi)_i \right] = 0 \quad (1.2.9)$$

This can easily be shown to be equivalent to:

$$(\partial_t + \vec{u} \cdot \nabla) \vec{u} = - \frac{\nabla P}{\rho} - \nabla \Phi, \quad (1.2.10)$$

by inserting  $T_{ij}$  into (1.2.9) and using the continuity equation.

The fluid equations considered so far, are only valid in a static space. The expansion of the universe therefore has to be taken into account in order for it to be a valid description of matter in the universe. The simplest way to incorporate the expansion of the universe is to switch to co-moving coordinates  $\vec{x}$ . This is because the proper distance,  $\vec{r} = a(t)\vec{x}$ , and the time coordinate,  $t$ , are not independent when space is expanding. Therefore their derivatives will also be somewhat more convoluted. Using co-moving coordinates, however, will untangle the space and time coordinates making them more straightforward. The derivative of the physical coordinates can be written in terms of the co-moving coordinates using the chain-rule:

$$\frac{\partial}{\partial r} = \frac{\partial x}{\partial r} \frac{\partial}{\partial x} = \frac{1}{a(t)} \frac{\partial}{\partial x}. \quad (1.2.11)$$

Similarly, for the time-derivative at fixed  $\vec{r}$  and fixed  $\vec{x}$ , we have:

$$\left(\frac{\partial}{\partial t}\right)_r = \left(\frac{\partial}{\partial t}\right)_x + \left(\frac{\partial x}{\partial t}\right)_r \cdot \frac{\partial}{\partial x} = \left(\frac{\partial}{\partial t}\right)_x - \frac{\dot{a}(t)}{a(t)^2} \vec{r} \cdot \frac{\partial}{\partial x} = \left(\frac{\partial}{\partial t}\right)_x - H(t) \vec{x} \cdot \frac{\partial}{\partial x}. \quad (1.2.12)$$

Finally, we also need to express the velocity in terms of the co-moving velocity,  $\vec{v}$ :

$$\vec{u} = \partial_t(a(t)\vec{x}) = H(t)a(t)\vec{x} + a(t)\dot{\vec{x}} = H(t)a(t)\vec{x} + \vec{v}. \quad (1.2.13)$$

Inserting these relations into the fluid equations gives us [5]:

$$\textbf{Continuity Equation:} \quad (\partial_t - H(t)\vec{x} \cdot \nabla)\rho + \frac{1}{a(t)}\nabla \cdot (\rho[H(t)a(t)\vec{x} + \vec{v}]) = 0 \quad (1.2.14)$$

$$\textbf{Euler Equation:} \quad (\partial_t + H(t) + \frac{1}{a(t)}\vec{v} \cdot \nabla)\vec{v} = \frac{-\nabla P}{\rho a(t)} - \frac{\nabla \phi}{a(t)} \quad (1.2.15)$$

$$\textbf{Poisson Equation:} \quad \nabla^2 \Phi = 4\pi G \rho a(t)^2, \quad (1.2.16)$$

With all the fluid equations now accounted for, we can move on to see how these three equations can be used to describe how structure evolved during the early universe.

## 1.2.2 Linear perturbation

We imagine an on-average homogeneous space but with small matter perturbations. These perturbations are very small and so, to first order, we can write the mass density in terms of a background solution and a small perturbation term [5]:

$$\rho(x, t) = \bar{\rho}(t) + \delta\rho(x, t) = \bar{\rho}(1 + \delta), \quad (1.2.17)$$

and similarly for  $\phi(x, t)$  and  $P(x, t)$ . As the background solution is homogeneous, it cannot depend on spatial coordinates. We will now insert them into the fluid equations, starting with (1.2.14):

$$(\partial_t - H(t)\vec{x} \cdot \nabla)\bar{\rho}(1 + \delta) + \frac{1}{a(t)}\nabla \cdot (\bar{\rho}(1 + \delta)[H(t)a(t)\vec{x} + \vec{v}]) = 0. \quad (1.2.18)$$

This can now be solved order-by-order, so in the zeroth order equation we have:

$$\partial_t \bar{\rho} + 3H(t)\bar{\rho} = 0. \quad (1.2.19)$$

This equation should be very well known by now, as it tells how the density of the universe evolves with respect to the scale factor (i.e. for matter  $\rho \propto a^{-3}$ ). This was to

be expected since the zeroth order term should describe the evolution of matter in a completely homogeneous universe and this was covered in section 1.1. Now to first order, we have:

$$(\partial_t - H(t)\vec{x} \cdot \nabla)[\bar{\rho}\delta] + \frac{1}{a(t)}\nabla \cdot (\bar{\rho}\delta H(t)a(t)\vec{x} + \bar{\rho}\vec{v}) = 0, \quad (1.2.20)$$

which, by using (1.2.19), can be simplified to:

$$\dot{\delta} = -\frac{1}{a(t)}\nabla \cdot \vec{v}. \quad (1.2.21)$$

We can do a similar perturbative expansion of (1.2.15) and (1.2.16) to first order. These are quite simple and end up being respectively:

$$\dot{v} + H(t)v = -\frac{\nabla\delta P}{a(t)\bar{\rho}} - \frac{\nabla\delta\Phi}{a(t)} \quad (1.2.22)$$

$$\nabla^2\delta\Phi = 4\pi G\bar{\rho}\delta a(t)^2 \quad (1.2.23)$$

Finally, all the first-order equations can be used to find a differential equation for  $\delta$ . To do this, the three equations need to be used to eliminate  $\vec{v}$  and  $\delta\Phi$ . For the pressure term, a relation for adiabatic processes can be used, as the expansion of the universe can be argued to be adiabatic at least early on [5]. This relation relates the pressure fluctuations with density fluctuations and looks the following way:

$$\delta P = c_s^2\delta\rho = c_s^2\bar{\rho}\delta, \quad (1.2.24)$$

where  $c_s$  is the speed of sound in the given medium. Returning to the three equations. If the equation (1.2.21) is differentiated with respect to time, then this will give:

$$\ddot{\delta} = \frac{H}{a}\nabla \cdot \vec{v} - \frac{1}{a}\nabla \cdot \dot{v}, \quad (1.2.25)$$

which is dependent on  $\dot{v}$ . This allows the insertion of (1.2.22) into the above equation:

$$\ddot{\delta} = \frac{2H}{a}\nabla \cdot \vec{v} + \frac{\nabla^2\delta P}{a\bar{\rho}} + \frac{\nabla^2\delta\Phi}{a^2} \quad (1.2.26)$$

Finally, inserting all the equations (1.2.23), (1.2.24) and (1.2.21) into our expression gives:

$$\boxed{\ddot{\delta} = -2H\dot{\delta} + \frac{c_s^2}{a^2}\nabla^2\delta + 4\pi G\bar{\rho}\delta} \quad (1.2.27)$$

This equation is typically referred to as Jeans' equation and it governs the evolution of deviations of the mean matter density in the early universe. It is a partial differential equation as  $\delta$  depends on both  $\vec{x}$  and  $t$ . In order to solve it, it is usually Fourier transformed into  $\vec{k}$ -space and assumed separable:

$$\delta(\vec{x}, t) = \int e^{i\vec{k}\vec{x}} \delta(\vec{k}, t) \quad \text{with} \quad \delta(\vec{k}, t) = D(t) \delta(\vec{k}) \quad (1.2.28)$$

where  $\vec{k}$  is the co-moving wavenumber and  $D(t)$  is the growth function. In this way, the solutions to equation (1.2.27) can be separated into modes with varying  $\vec{k}$  values. As the growth of the different modes is independent of their wavenumber to first order, then we may solve for the growth function. The growth function would then allow us to take some initial distribution  $\delta(\vec{k})$  and evolve it in time.

From now on  $\delta$  will therefore be assumed to be a specific mode and will only depend on time. We will also ignore the pressure term in the Jeans' equation. This is a fairly decent assumption for non-relativistic matter, where it generally holds that  $\rho \gg P$ . This means the Jeans' equation becomes:

$$\ddot{\delta}_m = -2H\dot{\delta}_m + 4\pi G\bar{\rho}\delta, \quad (1.2.29)$$

where I have added a subscript  $m$  to emphasize, which densities only pertain to matter. As the growth function depends on the Hubble parameter, then it will look different for the various cosmological epochs. This will now be explored (See e.g. D. Tong [36] or D. Baumann [5, Sec. 4.1]).

### Radiation-dominated epoch

The total fluctuations in matter density will be  $\delta\rho = \delta\rho_r + \delta\rho_m$ . It can however be argued that on sub-horizon scales  $\delta\rho_r$  fluctuations do not grow, but instead oscillate as sound waves [36]. As such relativistic matter does not cluster and the contribution from  $\delta\rho_r$  can essentially be ignored. The equation then reads:

$$\ddot{\delta}_m = -2H\dot{\delta}_m + 4\pi G\bar{\rho}_m\delta_m. \quad (1.2.30)$$

The first Friedman equation, (1.1.6), tells that  $H^2 \propto \bar{\rho}$ . In this case  $H^2 \sim \bar{\rho}_r \gg \bar{\rho}_m$ , since this occurs in the radiation-dominated universe. This means the general relation  $-2H\dot{\delta}_m \gg 4\pi G\bar{\rho}_m\delta_m$  holds. Therefore the final term may be ignored:

$$\ddot{\delta}_m + 2H\dot{\delta}_m = 0 \quad (1.2.31)$$

From cosmology, it is known that the scale factor in the RD universe grows as  $a(t) \propto t^{\frac{1}{2}}$ , so  $H(t) = \frac{1}{2t}$ . The equation therefore takes the form of an ODE:

$$\ddot{\delta}_m + \frac{1}{t}\dot{\delta}_m = 0. \quad (1.2.32)$$

This can simply be solved by doing separation of variables twice. A very obvious solution is the constant solution,  $\delta_m = c$ , as the equation only depends on derivatives. Another solution is  $\delta_m \propto \log(t)$ . We therefore see that the matter density fluctuations barely grow during the RD epoch.

### Matter-dominated epoch

In the MD epoch, we can also ignore the contribution from radiation  $\delta\rho_r \sim 0$ . This again means the equation (1.2.30) is valid. This time however Friedmann's first equation is used to rewrite  $4\pi G\bar{\rho}_m = \frac{3}{2}H^2$ . This will give:

$$\ddot{\delta}_m + 2H\dot{\delta}_m - \frac{3}{2}H^2\delta_m = 0. \quad (1.2.33)$$

From cosmology, the scale factor in the MD epoch is known to be  $a(t) \propto t^{\frac{2}{3}}$ , which implies  $H(t) = \frac{2}{3t}$ . Assuming a power-law solution,  $\delta_m = t^n$ , then means an equation for  $n$  can be found:

$$\begin{aligned} n(n-1)t^{n-2} + \frac{4}{3t}nt^{n-1} - \frac{3}{2}\frac{4}{9t^2}t^n &= 0 \quad \Longleftrightarrow \quad n(n-1) + \frac{4}{3}n - \frac{2}{3} = 0 \\ &\Longleftrightarrow \quad (n+1)(n-\frac{2}{3}) = 0. \end{aligned}$$

There are two solutions. The first,  $n = -1$ , is unphysical, as we know that density fluctuations cannot have become smaller since the CMB. Therefore, the second solution,  $n = \frac{2}{3}$ , will be the physical solution. This tells us that the growth of structure in the MD epoch follows the power-law  $t^{\frac{2}{3}}$ . This is exactly the same behaviour as the scale factor. A quick comparison between the growth of  $\delta$  during the radiation and the matter-dominated epoch shows that  $\delta$  grows much faster in the matter-dominated epoch. This implies most of the structure growth is expected to occur during the matter-dominated universe.

Finally, as the  $\Lambda$ -dominated epoch is just beginning to happen today, it is not very important for us. However, it can be shown, following an argument similar to the radiation-dominated epoch, that  $\delta \sim \text{const.}$  [36].



The relations derived up until this point cannot be extrapolated beyond the horizon,  $\lambda > \frac{c}{H}$ , due to Newtonian perturbation theory only being an adequate description for smaller regions of spacetime. The modes encapsulated by this description are therefore referred to as 'sub-horizon' modes. There are however also 'super-horizon' modes, which need to be described. It is not immediately obvious that such modes with  $\lambda > \frac{c}{H}$  should even be meaningful, since if the early universe had only undergone the radiation period,  $\frac{c}{H}$  would precisely represent the particle horizon [36]. This implies that the two ends of these modes could not be causally connected making it illogical to suggest that they were part of the same fluctuation. However, due to the inflationary period, the actual particle horizon would be larger than  $\frac{c}{H}$  allowing such matter perturbation waves to exist in this scenario. Therefore it is important to consider these modes, as they turn out to be very physically relevant.

	Radiation-Epoch	Matter-Epoch
Sub-horizon	$\log(a)$	$a$
Super-horizon	$a^2$	$a$

**Table 1.3:** A summary of the growth of matter perturbations throughout the different epochs as a function of the scale factor. It is separated for modes below the size of the apparent horizon ( $\lambda < \frac{c}{H}$ ) and those larger than the apparent horizon

### Super-horizon modes

A simple argument may be made for the result of 'super-horizon' modes. It goes as follows: In the super-horizon regime, we can effectively ignore the action of gravity and focus only on the expansion of the universe. The expansion can be found using the Friedmann equation  $H_{\text{avg}}^2 = \frac{8\pi G\bar{\rho}}{3}$ . An over-dense region of spacetime  $\rho > \bar{\rho}$  would create a local positive curvature:

$$H_{\text{avg}}^2 = \frac{8\pi G}{3}(\bar{\rho} + d\rho) - \frac{k}{a^2} \quad (1.2.34)$$

$$\implies \delta = \frac{d\rho}{\bar{\rho}} = \frac{3k}{8\pi G a^2 \bar{\rho}}. \quad (1.2.35)$$

From this argument it is evident that  $\delta \propto (\bar{\rho} a^2)^{-1}$ . Since  $\bar{\rho}$  is known for respectively the radiation-dominated epoch ( $\bar{\rho} \propto a^4$ ) and the matter-dominated epoch ( $\bar{\rho} \propto a^3$ ), then we can summarize the results of the behaviour of the various modes (see Tab. 1.3).

### 1.2.3 The transfer function and the power spectrum

Our main interest is to find out how some initial perturbations at an early time  $\delta(k, t_0)$  evolve. This behaviour is encapsulated by the transfer function:

$$\delta(k, t) = T(k)\delta(k, t_0), \quad (1.2.36)$$

where  $t_0$  is some time in the early universe. As long as  $\delta$  is small, then linear perturbation will give us the correct answer to this equation. It won't hold for later times, where non-linear effects will affect the gravitationally collapsed regions.

Since the universe is not static, then the co-moving horizon will also expand over time. This means in particular that any mode, which starts off being outside the horizon will eventually enter the horizon. Precisely when the modes enter the horizon matters much due to the difference in the growth of modes inside and outside the horizons. The delimiter of modes first entering during the matter-dominated epoch can be found as those with  $k > k_{\text{eq}}$  where:

$$k_{\text{eq}} = \frac{2\pi}{c}(aH)_{\text{eq}}. \quad (1.2.37)$$

Here  $(aH)_{\text{eq}}$  denotes the value at matter-radiation equality, which is around  $z = 3400$ . By tracking each mode, its growth according to Table 1.3 and when it enters into horizon it is possible to come up with the following expression for the transfer function:

$$T(k) \propto \begin{cases} 1 & k \leq k_{\text{eq}} \\ \frac{1}{k^2} & k > k_{\text{eq}} \end{cases} \quad (1.2.38)$$

The transfer function is typically used in tandem with the power spectrum, as the power spectrum is the most convenient way to phrase the problem of matter perturbations. The power spectrum,  $P(k)$ , is defined through the correlation function [36]:

$$\langle \delta(k)\delta(k') \rangle = (2\pi)^3 \delta_D(\vec{k} + \vec{k}') P(k), \quad (1.2.39)$$

where due to isotropy, the power spectrum will not be dependent on the direction of  $\vec{k}$ . The power spectrum tells us about how likely it is to find large clumps of matter together. It can generally be written as  $P(k) \propto k^n$  in the case of matter perturbations. The power-law power spectrum  $P(k)$  can be thought of as giving rise to the real-space correlation function  $\varepsilon(r) \propto r^{-(n+3)}$  at least for larger values of  $r$  [36]. Due to the cosmological principle, we know the spatial correlation should drop for far separated points if we wish to retain homogeneity and isotropy on large-scales. Consequently, we may ignore

any power spectrum with  $n < -3$ , since these would imply spatial correlations that grows with distance. Now for  $n = -3$  the correlation function is constant and this leads to a so-called 'scale-free' distribution since the correlation between two points will be independent of their distance. This means clusters of any size are (in theory) attainable and it can be shown that their probability to form follows a power-law.

For  $n > -3$ , it becomes increasingly probable that neighboring points are related, while points that are further apart are less likely to be related. This results in the formation of many small clusters and progressively fewer large clusters as  $n$  grows.

The observed behaviour of the power spectrum is  $n \sim 0.96$  [18]. This fits closely with the prediction from inflation, which is  $n = 1$ . The power spectrum  $n = 1$  is somewhat special since this produces scale-free correlations for the gravitational potential. The correlation function for the gravitational power spectrum can be shown to be related to the power spectrum of density fluctuations as  $P_\phi(k) \propto k^{-4}P(k)$  so if  $P(k) \propto k$ , then this exactly becomes scale-invariant [36]. We will assume that  $n = 1$  for the remainder of this section.

Adding the transfer function to the power spectrum tells how each mode is affected by the structure formation:

$$P(k) \rightarrow T(k)^2 P(k) = \begin{cases} k & k \leq k_{\text{eq}} \\ \frac{1}{k^3} & k > k_{\text{eq}} \end{cases}, \quad (1.2.40)$$

when assuming  $P(k) \propto k$ . This is therefore our major prediction of structure formation. The way to interpret this distribution is that  $k$  is inversely proportional to the wavelength of the collapsed or decoupled regions (over-dense or under-dense regions of matter). Therefore large  $k$  behaviour of (1.2.40) will describe the amount of small-scale structure, while the small  $k$  behaviour describes the amount of large-scale structure. As only linear perturbation theory has been looked at, this only works for early times to give an idea of the sizes of various clusters. It cannot be taken to give direct predictions on the mass spectrum of our universe, since these processes are very non-linear. Statements about the mass spectrum are therefore often left to simulations.

Due to the abundance of dark matter in the universe, and the fact that it must decouple earlier from equilibrium than baryonic matter, it will be the main driving force in structure formation. As such another subtlety needs to be discussed. This is the question of whether dark matter is relativistic (warm or hot) or non-relativistic (cold) when it decouples from the primordial equilibrium. The importance of the nature of dark matter stems from the fact that relativistic dark matter will not cluster as easily as

non-relativistic dark matter. None of these types of dark matter are however ruled out by experiments, so they are both important to describe.

When dark matter is relativistic it is 'freely streaming', which means it generally does not interact with other particles until it has travelled some mean length and so does not cluster below this scale [7]. The intuition for this is that smaller gravitational potentials will not be able to 'catch' the fast-moving relativistic particles and so only the large gravitational potentials lead to clustering. The free-streaming scale can be found as:

$$\lambda_{\text{fs}}(t) = a(t) \int_{t_i}^t dt' \frac{v(t')}{a(t')}, \quad (1.2.41)$$

where  $v(t)$  is the velocity distribution of the dark matter particles and  $a(t)$  is the scale factor of the universe. Since dark matter won't cluster below the free-streaming length, then this means the behaviour of the power spectrum (1.2.40) will differ for large  $k$  depending on the free-streaming length. Consequently, this implies that different models of dark matter can be distinguished through their predictions for the free-streaming length. This will be further explored during the next section on dark matter.

## 1.3 Dark matter

Dark matter has gradually become a standard prediction of every cosmological model. It serves as an explanation for a broad array of phenomena, which otherwise would not fit with our current models of the early universe and structure formation. The evidence for dark matter comes from various observations in astronomy and cosmology, these include:

- The behaviour of galaxies
- The behaviour of galaxy clusters
- Processes in the early universe leading to an inhomogeneous universe

It is not immediately obvious that the introduction of dark matter would be able to explain unaccounted behaviour on so many scales of our universe. This is however exactly what makes dark matter such a strong hypothesis. While any one of the phenomena could perhaps be explained by an alternative hypothesis, as of yet, only dark matter is able to account for them all. This makes it much more useful and predictively strong, than any of the alternative models that exist. To get a sense of the extent of the

problems dark matter may solve, I will go through some of the most important evidence of dark matter.

### 1.3.1 Dark matter evidence

One of the classic pieces of evidence for dark matter is the anomalous behavior of galactic rotation curves. According to Newtonian gravitation, the circular velocity can be found by solving Newton's second law in the presence of a gravitational field:

$$v_c(r) \propto \sqrt{\frac{GM(r)}{r}}, \quad (1.3.1)$$

with  $r$  being measured from the center of the galaxy and  $M(r)$  being the mass encapsulated within this region. For distances beyond the galactic disk, then Gauss' law suggests that  $M$  should become constant. Therefore the behaviour of  $v_c$  around the disk should start following  $r^{-\frac{1}{2}}$ . This is however contrary to observations, which instead suggest that the rotation curves remain constant around the galactic disk, i.e.  $M(r) \propto r$  (See e.g. [17] or [23]). The simplest possible explanation for this phenomenon is the existence of unaccounted-for mass within and around the galaxy. The unaccounted mass cannot interact electromagnetically, as then it would be visible to us, therefore it would have to be some form of neutral (or dark) matter.

Similar to the story of galactic rotation curves, it has also been observed that there must be much missing mass in galaxy clusters. For galaxy clusters, this observation comes from the existence of hot intra-cluster gas, as without dark matter, the gravitational potential of the cluster should not be strong enough to hold onto it to such a degree [17]. Both the evidence for dark matter in galaxies and clusters is further corroborated by gravitational lensing experiments. Gravitational lensing will be introduced in the next section, but it is a powerful probe of mass distributions in the cosmos. It also remains the simplest way to probe the existence of non-luminous material. It is therefore, for instance, the main way to probe non-luminous matter outside of a galactic disk.

As for dark matter evidence in cosmology, then this comes partly in the form of the CMB. In particular, anisotropies in the CMB are used to fit the cosmological contents of the universe, this includes the non-baryonic content [17]. Additional experimental sources are required to accurately determine this value, including estimates of light element abundances from Big Bang Nucleosynthesis, which provide insights into the universe's total baryonic content. Finally, our current models of structure formation also

require more mass than what baryons alone can provide in order to accurately predict the local inhomogeneities observed today. This therefore also suggests the existence of non-baryonic matter.

Altogether, these observations give a coherent picture of a universe, where the matter content is completely dominated by dark matter. It is estimated that dark matter constitutes nearly 27% of the universe's energy density, while ordinary matter accounts for only about 5%.

### 1.3.2 Particle dark matter

To this day, the microscopic nature of dark matter remains a total mystery. Most models posit that dark matter can be characterized as a particle, since non-particle descriptions are generally less persuasive, especially concerning structure formation. Consequently, only particle-based models will be discussed here.

A common feature of all particle descriptions of dark matter is that they must be neutral and highly stable<sup>3</sup> particles, since otherwise they would have left very distinct traces that would have been observed by now. Additionally, their stability is essential for them to play a role in structure formation. Dark matter particles must also be massive because relativistic particles do not cluster, as was stated in the previous section. The clustering of dark matter is crucial, as all evidence for dark matter's existence is gravitational, indicating that dark matter particles must exert a significant collective gravitational influence on the structure of the universe. While it is by no means impossible for dark matter to be relativistic in the early universe, it must eventually become non-relativistic to form clusters as the universe expands. Despite the fact that dark matter is known to be massive, the exact size of its mass remains highly model-dependent possibly spanning many orders of magnitude (See Figure 1.1).

Another very model-dependent aspect of dark matter is the extent to which it interacts with standard model particles. This is because it is not prohibited for dark matter to interact with the Standard Model through the weak force. Most models of dark matter therefore allow for such interactions. In this case, the introduction of a weakly interacting particle can potentially have an impact on the primordial equilibrium depending on

---

<sup>3</sup>Dark matter is actually not prohibited from decaying, however, its decay rate has to be very small,  $\Gamma \sim t_{\text{universe}}$ , in order to fit with current observations

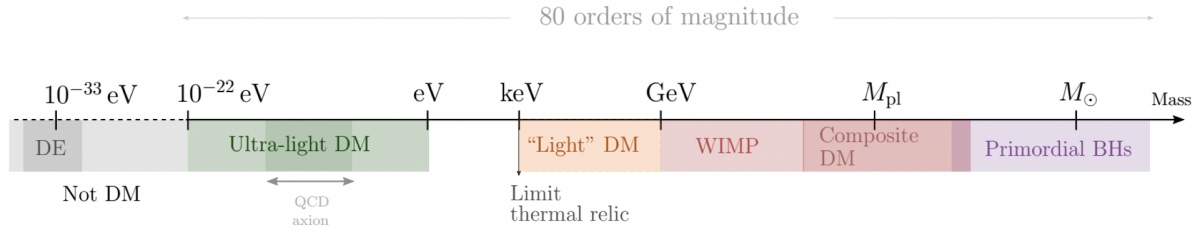


**Figure 1.1:** An illustration that showcases the numerous orders of magnitude that dark matter models may encompass. In this thesis, we are mainly concerned with 'Light-DM' and 'WIMPs (weakly interacting massive particles)'. Image credit to Ferreira [14, Fig. 1]

its interaction strength. Big Bang Nucleosynthesis is thus used to constrain, which interaction strengths are realistic for a given particle model.

The only standard model particle, which possesses all of these traits is the neutrino. Historically, the neutrino was also one of the first perceived dark matter particle candidates [6]. This was particularly the case when the mass bounds of the three neutrinos were less certain, and measurements suggested that neutrinos could play a significant role in structure formation. However, it eventually became clear that neutrinos were insufficient to account for all the dark matter in the universe, resulting in their dismissal as dark matter candidates. Today, there are three major reasons why neutrinos are not considered viable dark matter candidates. First, modern measurements of the neutrino masses have verified them to be very small ( $\sum m_{\nu} < 2\text{eV}$  [28]). Thus, using estimates of the expected energy density of neutrinos in the late universe will not be sufficient to account for the known energy density of dark matter [7]. Second, the structure formation predicted by neutrinos deviates much from current observations [18]. This can be seen as a consequence of it being very relativistic, when the weak force decouples, due to its small mass (see next subsection). Finally, there is also a lower bound for the mass of fermionic dark matter particles, called the Tremaine-Gunn bound. This is based on the exclusion principle and it asserts that the mass of fermionic dark matter must be on the order of a few hundred eV to account for the mass in dwarf galaxies [7]. This bound actually contradicts the first bound from cosmology meaning even if the mass of the neutrino was a little larger, it still likely could not be a proper dark matter candidate. It is therefore expected that dark matter must be a non-Standard Model particle.

Many extensions to the Standard Model have been proposed over the years. Some of them deliver new particles that could play the role of dark matter. However, instead of focusing too much on individual models, I will try and split it up into two categories of dark matter, namely cold dark matter (CDM) and warm dark matter (WDM). Each of these categories will be explored through a specific dark matter candidate, which

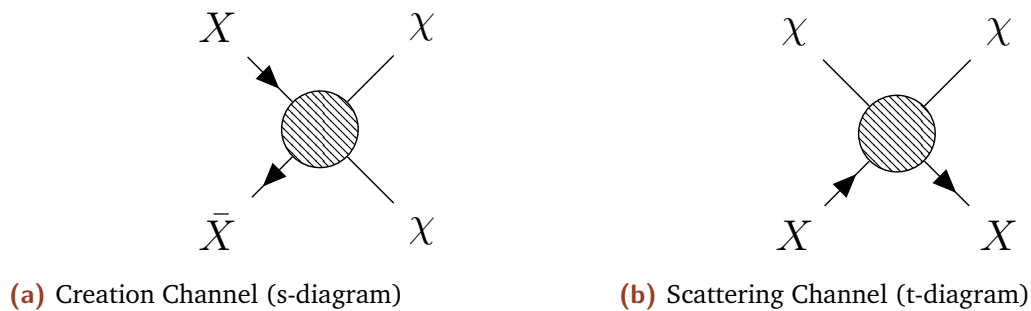


**Figure 1.2:** An illustration of possible processes involving dark matter in the early universe. **Left:** The creation/annihilation channel of dark matter. Two Standard Model particles ( $X/\bar{X}$ ) meet and create two dark matter particles ( $\chi$ ). **Right:** The scattering channel of dark matter. A dark matter particle ( $\chi$ ) encounters a Standard Model particle ( $X$ ) and scatters off it.

encapsulates the common features of the category. For CDM the representative will be WIMPs (weakly interacting massive particles), while for WDM the representative will be sterile neutrinos. Both of these types of dark matter also have the advantage of being very akin to neutrinos in various respects. This makes it simple to draw parallels between them and neutrinos.

For our purposes, WIMPs can be thought of as heavy neutrinos. Although they possess additional characteristics compared to neutrinos<sup>4</sup>, when considering only their interactions with the Standard Model, they are essentially just much heavier versions of neutrinos. Due to them being much heavier than neutrinos, then they freeze out non-relativistically thereby evading all the criteria, which ruled out the neutrino's candidacy. One of the initially compelling arguments for WIMPs is actually the fact that they can reproduce the energy density associated with dark matter. This phenomenon is typically referred to as the 'WIMP-miracle'. It states that if we assume reactions like those presented in Figure 1.2, mediated by the weak force, then their cross-sections can be used to predict a value for the observed abundance of dark matter. As the cross-section depends on the mass of the dark matter particle,  $m_\chi$ , then it specifically requires  $m_\chi \sim 100\text{GeV}$  for the critical density associated with dark matter to align with predictions from our current cosmological models (See e.g. [4, Sec. 3.2] and [23, Sec. 2.2]).

Sterile neutrinos, on the other hand, can be thought of as heavier and more dormant neutrinos. They are conjectured to be right-handed neutrinos, which may explain both the origin and the smallness of the neutrino mass [7]. Since the mass of sterile neutrinos is only on the orders of KeV, they would normally be expected to freeze out in a manner akin to neutrinos. However, due to their incredibly tiny interaction strength, they do

<sup>4</sup>This includes an explanation as to why they do not decay. Such an explanation is typically associated with a new symmetry prohibiting them from decaying. This is however not immediately relevant here



not actually participate in the primordial equilibrium. In this way, they too are able to evade criteria that dismisses neutrinos as dark matter candidates, particularly regarding structure formation.

### 1.3.3 The CDM and WDM paradigm

The main distinction between CDM and WDM particles is whether or not the dark matter particle is relativistic or non-relativistic when the particle is produced. For CDM this will be around when the weak force decouples from the primordial equilibrium. This is because the velocity distribution of dark matter will have an effect on its free-streaming length. As CDM particles decouple while being non-relativistic, they start to cluster immediately. They have a small free-streaming length, as their average velocity will not be very high in comparison to WDM particles. As mentioned in the previous section, the free-streaming length affects the power spectrum, with a large free-streaming length specifically suppressing the highest  $k$  modes. Since these  $k$  modes are reciprocally related to the size of the collapsed regions, statements about the suppression of the highest  $k$  modes can be interpreted as statements about the smallest expected collapsed regions. While it remains impossible to analytically extrapolate this result directly to its impact on structure formation, due to the numerous non-linear effects involved in the later stages of structure formation, then this can be accomplished through numerical simulations. Large-scale simulations are therefore employed to verify the effect of dark matter on the production of structure. In this way, the free-streaming length of CDM can, through simulations, be shown to mostly affect the production of structure below the mass of the Earth [18].

For WDM the story is quite different. WDM will have a much larger free-streaming length, resulting in the suppression of much larger substructures. Specifically, this suppression is expected to affect the production of structure just below the scales of galaxies [18]. This includes for instance dwarf galaxies and other types of galactic substructure. The suppression of the power spectrum for both CDM and WDM is showcased in Figure 1.3. It is clear from the figure that for large  $k$  the results for CDM and WDM differ and it specifically happens for  $k$ 's corresponding to sub-galactic structure. As can also be seen the mass of the WDM particle also plays quite an important role in exactly, which type of galactic substructure is suppressed. This is natural because a higher mass leads to the particle being slightly less relativistic in the early universe.

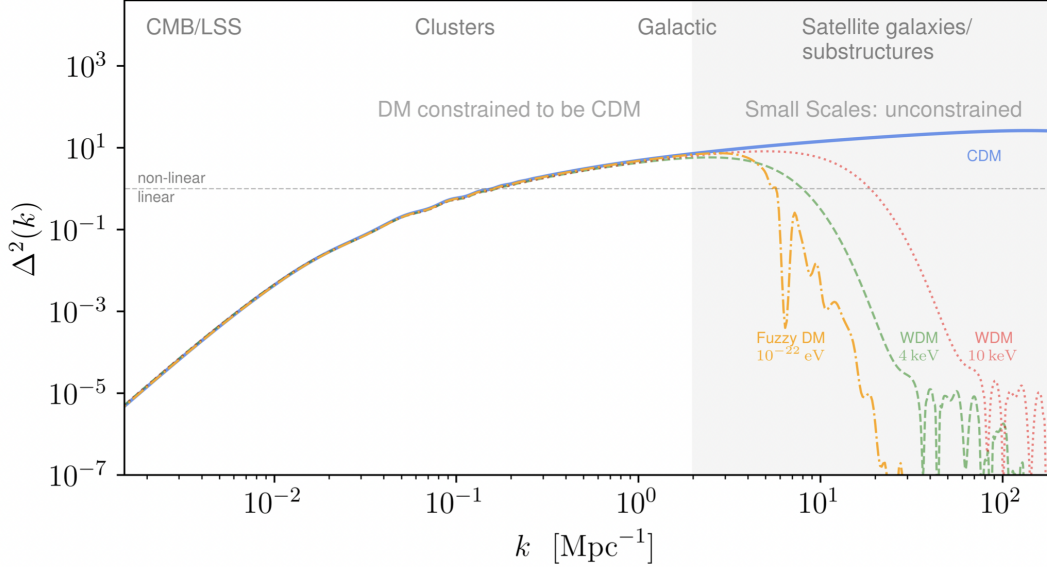


**Figure 1.3:** This figure shows the (dimensionless) power spectrum as a function of  $k$ . The blue curve shows the CDM prediction, while the green and red curves show the predictions for WDM models with resp.  $m = 4\text{KeV}$  and  $m = 10\text{KeV}$ . As is evident, the CDM and WDM predictions differ for large  $k$ . The regions with large  $k$  will be exactly those that are responsible for the sub-galactic structure, as  $k$  can be interpreted as the wavenumber of the collapsed regions. According to simulations, WDM therefore predicts much fewer sub-galactic structures than CDM. Image credit to Ferreira [14, Fig. 2].

Altogether, this suggests that WDM models predict much less sub-galactic structure compared to CDM models. Our current simulations and models suggest that structure is formed hierarchically for both CDM and WDM models [18], meaning small collapsed structures merge together to form larger ones. It is therefore expected that the larger collapsed regions, like dark matter halos around galaxies or clusters, host many smaller subhalos within them. The number of the smaller subhalos will in this case depend on whether the dark matter model is warm or cold. Simulation suggests the mass spectrum of dark matter subhalos should follow  $\frac{dN}{dM} \propto m^{-\beta}$  with  $\beta = 1.9$  [34]. In this case, CDM and WDM will differ by their lower mass bound. The value of this lower mass bound depends on the specific CDM/WDM model and the simulation itself, so we can only discuss it in terms of orders of magnitude. In general, the bounds will be thought of as:

$$\text{For CDM: } M_{\text{Min}} \lesssim 1M_{\text{Sun}}$$

$$\text{For WDM: } M_{\text{Min}} \sim 10^6 M_{\text{Sun}}$$

Therefore, a probe of sub-galactic structure is needed to distinguish between CDM and WDM models. This is consequently the main motivation of this thesis. Since CDM and

WDM predict the exact same mass spectrum on scales equal to or larger than galaxies, then this feat requires a probe, which is specifically sensitive to the lower part of the mass spectrum. The simplest way to envision how to probe dark matter is through gravity itself. This therefore directs us to the field of gravitational lensing.

# Gravitational lensing

Gravitational lensing is one of the major predictions of general relativity. It was first observed during the Eddington experiment in 1919, where two astronomers took advantage of a total solar eclipse to measure the apparent positions of stars near the sun [13]. They observed that the apparent positions of the stars differed from their usual positions when the sun was not near the stars' field of vision. This was therefore clear evidence that the sun had bent the light of the background stars. Thus opening the doors to an entirely new experimental discipline in physics. At the time, this was considered a major triumph for the general theory of relativity, as it accurately predicted a phenomenon that Newtonian gravity did not immediately predict.

Since then, with the development of more sophisticated equipment, the phenomena of gravitational lensing has been seen in countless observations [32, See e.g. Chap. 2]. Most notable are the cases of strong gravitational lensing, where the bending of light is so strong that a source is displayed at multiple different positions on the image of a telescope. However, also weaker forms of gravitational lensing are used for measurements. A notable case is the statistical measurement of weak gravitational lensing, where a cluster sits in the foreground of a field of galaxies and influences their shape. This makes the galaxies appear somewhat more elliptical, which becomes a measurable effect if there are enough distorted galaxies [32]. Finally, gravitational microlensing is also a prominent use of gravitational lensing. This is the main topic of this thesis and so it will be explored in depth in the next section.

While, at first, gravitational lensing may just appear as an interesting natural phenomenon, it has gained much prominence in astronomy for being a probe of mass distributions in the cosmos (See e.g. Bartelmann and Schneider [3] or Schneider *et al.* [32] for a review). This is because the resulting image of a lensed source is heavily influenced by the intervening lens. Consequently, analyzing these lensed images can reveal information about the lens itself, thus giving us an indirect way to probe this object. This is especially relevant for dark matter, as it is not directly probable using light, which almost all astronomical equipment is based on. As such gravitational lensing is a crucial method for experimentally evaluating the properties of dark matter, especially concerning its effect on cosmic structure. Enhancing our understanding of gravitational

lensing and developing new techniques to leverage this tool are therefore crucial for gaining deeper insights into dark matter.

In the following, general relativity will be used to derive a general expression for the deflection angle. This derivation is heavily inspired by S. Carroll [8, See sec. 7.3] (an alternative derivation can be found in Schneider *et al.* [32, See sec. 4.1-4.3]). Then it will be shown how the deflection angle determines the lensing geometry and in particular will determine a key observable for microlensing: the magnification.

## 2.1 A general relativistic approach

To determine how a massive body affects a light ray through gravitational lensing, one must compute the geodesic of the light ray. Since geodesics are entirely determined by the metric tensor, the first step is to find an appropriate expression for the metric tensor. Given the complexity of this task without any assumptions, we typically somewhat simplify the situation<sup>1</sup>:

- The energy-momentum tensor  $T_{\mu\nu}$  can be represented as that of a perfect fluid. Specifically, we assume that the gravitational sources are predominantly dust, meaning that  $\rho \gg P$ .
- The weak-field assumption is made, which implies that the metric can be expanded around flat spacetime to the first-order as  $g_{\mu\nu} = \eta_{\mu\nu} + h_{\mu\nu}$  with  $|h_{\mu\nu}| \ll 1$  being a small perturbation.
- Finally, it will also be assumed that the gravitational sources are static, meaning  $\partial_t h_{\mu\nu} = 0$ .

Combining all these assumptions allows us to express the metric solely in terms of  $h_{00}$ . In the Newtonian limit, it can be shown that  $h_{00} = -2\Phi$ , where  $\Phi$  is the Newtonian gravitational potential, which obeys the Poisson equation. Thus, the metric takes the following form ([8, Eq. 7.59], [32, Similar to Eq. 4.13]):

$$ds^2 = -(1 + 2\Phi)dt^2 + (1 - 2\Phi)(dx^2 + dy^2 + dz^2). \quad (2.1.1)$$

---

<sup>1</sup>These assumptions are very similar to the well-known 'Newtonian limit'. The main difference however is that the speed of test particles is not restricted.

With an explicit form of the metric, it then becomes possible to calculate a null geodesic. However, since the field  $\Phi$  depends heavily on the photon's position along its trajectory, this calculation remains very challenging. One way to address this issue is by decomposing the geodesic into a background path and a perturbation [8]:

$$x^\mu(\lambda) = x^{(0)\mu}(\lambda) + x^{(1)\mu}(\lambda), \quad (2.1.2)$$

all evaluated along the path of the unperturbed trajectory. This simplifies things very much, as the unperturbed trajectory will be a null geodesic in flat spacetime. In this case, the perturbation expression  $x^{(1)\mu}(\lambda)$  will be the cause of the deflection and so our main goal will be to calculate its contribution along the unperturbed trajectory. In order for this procedure to be valid it is implicitly assumed that  $\Phi$  is not significantly different when following the true or the unperturbed trajectory. In most cases, this is a fairly solid assumption, however especially in cases where there are many deflectors along the line-of-sight such an approximation will possibly not suffice. Instead, the actual trajectory should be divided into many smaller segments, each justifying the use of the above method. The total deflection can then be determined by summing the deflection contributions from all these smaller segments. This therefore legitimizes the use of (2.1.2) even in these cases.

In order to find the deflection caused by  $x^{(1)\mu}(\lambda)$ , then we have to solve the null-geodesic equation order by order. Let's follow the same notation as Carroll [8]:

$$k^\mu \equiv \frac{dx^{(0)\mu}}{d\lambda}, \quad l^\mu \equiv \frac{dx^{(1)\mu}}{d\lambda}. \quad (2.1.3)$$

Before expanding the geodesic equation, we need to determine the conditions required for the geodesic to be null. These conditions can also be expanded order by order, resulting in:

$$(\eta_{\mu\nu} + h_{\mu\nu})(k^\mu + l^\mu)(k^\nu + l^\nu) = 0 \quad (2.1.4)$$

Solving the above equation to first-order then amounts to solving the following two equations:

$$(0) \quad \eta_{\mu\nu} k^\mu k^\nu = 0 \quad (2.1.5)$$

$$(1) \quad h_{\mu\nu} k^\mu k^\nu + 2\eta_{\mu\nu} k^\mu l^\nu = 0. \quad (2.1.6)$$

The zeroth order equation tells that  $k^2 = 0$ , which is simply the equation for a null-geodesic in flat spacetime. In particular it implies  $k_0 = |\vec{k}| \equiv k$ . From our initial

assumptions of the metric we also have (2.1.1)  $h_{\mu\nu} = -2\Phi\delta_{\mu\nu}$ . Using these two facts simplifies the first-order equation as follows:

$$(\vec{k} \cdot \vec{l}) - kl_0 = 2k^2\Phi \quad (2.1.7)$$

With this condition in mind, the geodesic equation itself can be solved order by order. The geodesic equation can be written in coordinates as:

$$\frac{d^2x^\mu}{d\lambda^2} + \Gamma_{\rho\sigma}^\mu \frac{dx^\rho}{d\lambda} \frac{dx^\sigma}{d\lambda} = 0. \quad (2.1.8)$$

As the background solution is merely that of a null geodesic in flat spacetime, then this will be the result to the zeroth order. If we stay in the Cartesian spatial coordinate system, which (2.1.1) is written in, then the Christoffel symbol for the Minkowski background vanishes. This means the Christoffel symbol would be zero unless it is taken to first-order. Therefore we may write the first-order equation as:

$$\frac{dl^\mu}{d\lambda} + \Gamma_{\rho\sigma}^{(1)\mu} k^\rho k^\sigma = 0. \quad (2.1.9)$$

The Christoffel symbols for the metric (2.1.1) then need to be computed. I will just refer to them here [8, Eq. 7.69]:

$$\begin{aligned} \Gamma_{0i}^0 &= \Gamma_{00}^i = \partial_i \Phi \\ \Gamma_{jk}^i &= \delta_{jk} \partial_i \Phi - \delta_{i[k} \partial_{j]} \Phi \end{aligned}$$

Inserting these equations into the first-order geodesic equation then gives:

$$\frac{dl^0}{d\lambda} = -2\Gamma_{0i}^0 k^0 k^i = -2k(\partial_i \Phi) k^i = -2k(\vec{k} \cdot \nabla \phi)$$

and,

$$\begin{aligned} \frac{dl^i}{d\lambda} &= -2\Gamma_{jk}^i k^j k^k = 2(k^2 \partial_i \Phi - k^i k^j \partial_j \Phi) \\ \implies \frac{d\vec{l}}{d\lambda} &= 2k^2 \nabla \Phi - k^{-2} (\vec{k} \cdot \nabla \Phi) \vec{k}. \end{aligned}$$

Where in both computations the symmetry of the lower indices of the Christoffel symbol was used  $\Gamma_{\nu\rho}^\mu = \Gamma_{\rho\nu}^\mu$ . The operator  $\nabla_\perp = \nabla - \frac{\vec{k}(\vec{k} \cdot \nabla)}{k^2}$  is often utilized to simplify the second expression.

It is now possible to calculate  $l^0$  and  $\vec{l}$ . It can simply be shown that  $l^0 = -2k\Phi$  by integrating  $\frac{dl^0}{d\lambda}$ . This is an important result as plugging it into (2.1.7) immediately implies orthogonality between  $\vec{k}$  and  $\vec{l}$  ( $\vec{k} \cdot \vec{l} = 0$ ). The vector  $\vec{k}$  points directly along the line-of-sight from the source to the observer, representing the path light would travel if undisturbed by any gravitational fields. This orthogonality then reflects that  $\vec{l}$  is exactly the component of the velocity, which deviates from the line-of-sight due to the gravitational fields along the trajectory. This means the deflection angle can be defined as<sup>2</sup>  $\alpha = -\frac{\Delta \vec{l}}{k}$ .

$$\Delta \vec{l} = \int \frac{d\vec{l}}{d\lambda} d\lambda = -2k^2 \int \nabla_{\perp} \Phi d\lambda = -2k \int \nabla_{\perp} \Phi ds, \quad (2.1.10)$$

where in the final step the integration was redefined as being along the physical distance  $s = k\lambda$ . This finally leaves us with a result for the deflection angle:

$$\boxed{\alpha = \frac{2}{c^2} \int \nabla_{\perp} \Phi ds} \quad (2.1.11)$$

The formula above can be used to derive one of the most famous results in general relativity: the deflection of light by a point source. To do this, let's assume, without loss of generality, the photon trajectory is along the  $z$ -axis. Furthermore, the point mass may then be placed in the plane  $z = 0$  such that its distance from the origin will be its impact parameter  $b = \sqrt{x^2 + y^2}$ . In this case, the gravitational field along the trajectory can be described by  $\Phi(z) = -\frac{GM}{(z^2 + b^2)^{\frac{1}{2}}} \mathbf{x}$ . This means the perpendicular gradient,  $\nabla_{\perp} = \hat{x}\partial_x + \hat{y}\partial_y$ , acting on the potential will give:

$$\nabla_{\perp} \Phi(z) = \frac{GM}{(z^2 + b^2)^{\frac{3}{2}}} \vec{b}. \quad (2.1.12)$$

Now, if the light is sufficiently far away from the source, the trajectory can be well approximated as the unperturbed trajectory and if it is viewed by an observer far away we may put the integration bounds as  $z = -\infty$  to  $z = \infty$ . Thus the deflection angle becomes:

$$\vec{\alpha} = \frac{2}{c^2} \int_{-\infty}^{\infty} \frac{GM}{(b^2 + z^2)^{\frac{3}{2}}} \vec{b} = \frac{4GM}{bc^2} \hat{b}. \quad (2.1.13)$$

This famous result, predicted by general relativity, was the formula Eddington's experiment sought to test back in 1919. Particularly, using the solar mass and radius it predicts a deflection angle of about 1.73 arcseconds. This prediction aligned with the experimental findings [13] and provided crucial support for the theory of general relativity.

---

<sup>2</sup>This expression comes directly from the geometry of the setup. The minus sign is a matter of convention, as the path is measured from the observer to the source



The above result will turn out to be important, especially in the next section on microlensing. The reason for this is due to Birkhoff's theorem (or the shell theorem in Newtonian gravity). This theorem states that spacetime outside and sufficiently far away<sup>3</sup> from a gravitating body has to coincide with the Schwarzschild spacetime (See e.g [8, Sec. 5.2]). Since the above deflection angle is precisely the deflection angle of a Schwarzschild metric (the metric (2.1.1) is more general than the Schwarzschild metric), then it implies that this equation can be used to calculate the deflection of light by a gravitating body virtually any time the light doesn't enter the body's perimeter. This is therefore a very useful result, particularly in non-strong lensing regimes.

## 2.2 The lens equation

In most cases, the extent of the gravitational bodies can be considered very negligible in comparison to the length of the light trajectory. This means that as long as the deflection angle is not taken to be too large, then there should be a very minimal difference between calculating the deflection along the perturbed and unperturbed light trajectories [24]. This is because the majority of the deflection occurs within a very narrow region, typically approximated as a single plane called the lens plane. The lens plane is located at the point where the trajectory is closest to the body it is scattering off, corresponding to the impact parameter distance. This approximation, often referred to as the 'thin-lens' approximation is extremely useful as it allows the calculation of more complex mass distributions. For a collection of point sources, it implies that the total deflection may be written simply as the sum [24]:

$$\alpha_{\text{tot}} = \sum_i \frac{4GM_i}{b_i c^2} \hat{b}_i. \quad (2.2.1)$$

It can also be used to define a continuum version of the above equation, which would allow for the calculation of the deflection of extended mass distributions. This is however not relevant to this thesis, so it won't be explored here. The above result is however very interesting in our endeavour, as it suggests a simple way to calculate the cumulative deflection of many point sources. The challenge, however, will become evident, when we try to describe how the light actually reaches the observer. This is governed by the lens equation.

The lens equation is another very important feature of the thin-lens approximation. It

---

<sup>3</sup>Far away as to avoid strong tidal forces due non-spherical symmetry

creates a direct relationship between the angle of the unlensed position ( $\vec{\beta}$ ) and the angle of the lensed position ( $\vec{\theta}$ ). It takes the following form:

$$\vec{\beta} = \vec{\theta} - \frac{D_{ds}}{D_s} \vec{\alpha}(\theta) \quad (2.2.2)$$

with  $\vec{\alpha}(\theta)$  being the deflection angle. The lens equation can be derived through a geometric argument presented in Figure 2.1. All the angles are two-dimensional and in general, the equation is non-linear due to the deflection angles' dependence on  $\theta$ . As  $\beta$  can be considered fixed, the roots of the lens equation will be the apparent angle of the source. The non-linearity of the equation is therefore precisely what allows multiple images to form.

The lens equation is often thought of as a mapping between the lensed and the unlensed coordinates. It is usually put into dimensionless form by defining scale  $x_0$  and  $y_0$  and their mutual relation ( $y_0 = \frac{D_s}{D_d} x_0$ ):

$$\vec{y} = \vec{x} - \frac{D_{ds} D_d}{x_0 D_s} \vec{\alpha}(x_0 x). \quad (2.2.3)$$

The action of the lens at every point is completely specified by  $\alpha(x)$ . While the above matrix equation will specify the mapping on the whole lens plane, it is often somewhat cumbersome to use. This is because of the non-linearity of the equation. Luckily, it is often enough to only know the mapping locally meaning it can be linearized using the Jacobian without many issues:

$$y_j = \frac{\partial y_j}{\partial x_i} x_i + o(x^2) = \left( \delta_{ij} + \frac{\partial \alpha(x)_{ij}}{\partial x_i} \right) x_i + o(x^2). \quad (2.2.4)$$

From this perspective, we now have a linear map between lensed and unlensed coordinates given by the Jacobian  $\frac{\partial y_j}{\partial x_i}$ . This mapping is valid as long as the Jacobian is not degenerate. The points and/or curves, where the Jacobian is degenerate are referred to as critical points/curves. They divide regions where multiple images of the source form and those with only a single image of the source. The description of lensing at, or very close to, these curves cannot be described by the linear mapping. The geometric optics employed to find the lens equation, i.e. Figure 2.1, would also not be correct here. Therefore we will try to refrain from describing these points through this formalism.

The Jacobian is usually decomposed into a diagonal matrix containing the trace and a trace-free matrix [24]:

$$\frac{\partial y}{\partial x} = \mathbb{I} - M(x) = \begin{pmatrix} 1 - \kappa & 0 \\ 0 & 1 - \kappa \end{pmatrix} + \begin{pmatrix} \gamma_1 & \gamma_2 \\ \gamma_2 & -\gamma_1 \end{pmatrix}, \quad (2.2.5)$$

where  $M(x) = \frac{\partial \alpha}{\partial x}$  and its decomposition consists of  $\kappa$  being called the 'convergence' and  $\gamma_1, \gamma_2$  being the two components of 'shear'. As their names suggest, the convergence describes whether the lens has a tendency to focus or defocus the light beam locally, whereas the shear components describe how the light beam is deformed. If the size of the two shear components is different this would, for instance, lead to an ellipsoidal stretching of the beam. Matching the above decomposition it can be shown how these quantities relate to the derivatives of the deflection angle:

$$\kappa = -\frac{1}{2}(\partial_1 \alpha_1 + \partial_2 \alpha_2) \quad , \quad \gamma_1 = \frac{1}{2}(\partial_1 \alpha_1 - \partial_2 \alpha_2) \quad , \quad \gamma_2 = \partial_1 \alpha_2 = \partial_2 \alpha_1. \quad (2.2.6)$$

As there will not be any lens modelling in this thesis, then this type of lens description will not be very prevalent throughout. However, another feature of the mapping, which will be very important, is the magnification. This is how the cross-sectional area of the beam is affected by gravitational lensing. It can be defined as the determinant of the inverse Jacobian:

$$\mu = \det \left[ \left( \frac{\partial y}{\partial x} \right)^{-1} \right] = \frac{1}{(1 - \kappa)^2 - \gamma_1^2 - \gamma_2^2}. \quad (2.2.7)$$

As is evident both the convergence and the shear will in general affect the magnification. The magnification allows us to describe how the apparent flux of light is changed due to lensing. This turns out to be the main observable in microlensing, which is central to this thesis. To illustrate the concepts of magnification and the lens equation, we will use the simple example of a point mass lens.

### 2.2.1 Point mass lens

In general, for a circularly symmetric lens, the lens equation can be reduced to a one-dimensional problem by aligning one of the axes with the deflection direction. This means the lens equation for a point mass can be simplified to the one-dimensional lens equation:

$$y = x - \frac{4GM}{x_0^2 c^2} \frac{D_{ds} D_d}{D_s} \frac{1}{x}.$$

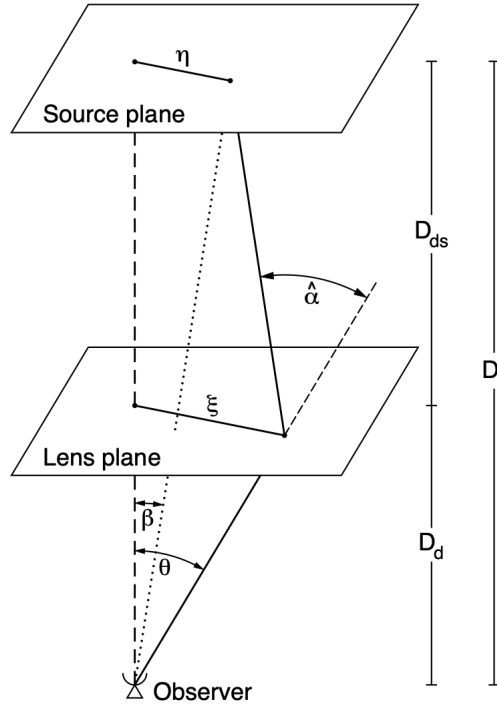


**Figure 2.1:** The geometric setup above demonstrates the geometry of gravitational lensing. As light is emitted from the source it is bent in the lens plane making the observer see the light coming from a different location. The lens plane is placed at a distance  $D_d$  from the observer, while the source plane lies at  $D_s$ . A principle axis is drawn from the observer to the lens (gravitational body) perpendicular to both the lens and source plane. The source itself makes the angle  $\beta$  with the principle axis, while the observer sees the source at an angle  $\theta$  due to lensing. The bending that occurs at the lens plane ( $\alpha$ ) will precisely be the angle between the line from the lens position to the actual source position and the line from the lens position to the lensed source position. This explains the setup. If it is assume that all angles  $\beta, \theta$  and  $\alpha$  are small, then using the small angle approximation ( $\sin(\phi) = \phi$ ) then:

$$D_s \theta = D_s \beta + D_{ds} \alpha(\xi), \quad (2.2.8)$$

by simply connecting the angular distances in the source plane (i.e  $D_s \beta = \eta$  on the diagram). The above equation is typically rewritten as:

$$\beta = \theta - \frac{D_{ds}}{D_s} \alpha(\xi). \quad (2.2.9)$$

This equation is known as the lens equation and is one of the cornerstones of gravitational lensing. It is usually thought of as a mapping between the lensed and unlensed coordinates. The gravitational lensing setup is in general specified by the deflection angle, the actual source position and the distances. The main variable is taken to be  $\theta$  and since  $\xi$  is the impact parameter, then there is a relationship between  $\xi$  and  $\theta$ . This means the equation is generally non-linear even for simple deflection angles. Image credit to Bartelmann and Schneider [3, See Fig. 11]

It is custom to define the scale as the Einstein angle  $x_0^2 = \frac{D_{ds}D_d}{D_s} \frac{4GM}{c^2}$  since this would leave us with the clean dimensionless equation (See [24, Sec. 3.1] or [32, Sec. 8.1.2]):

$$y = x - \frac{1}{x} \implies x^2 - 1 - yx = 0.$$

As showcased, this is a second-degree polynomial and so the lensed position of the images can be found as:

$$x_{\pm} = \frac{y \pm \sqrt{y^2 + 4}}{2}. \quad (2.2.10)$$

The point source lens thus creates two images one at  $x_-$  and one at  $x_+$ . For the specific value of  $y$ , where both roots are identical the image is instead mapped into a circular arc, called an Einstein ring, with a radius determined by the Einstein angle. To truly understand the images of the point source, an understanding of the magnification of the two images is also needed. This can be calculated by considering how an area-element in the source plane compares to an area-element in the lens plane<sup>4</sup> [32]:

$$\mu^{-1} = \frac{dA_s}{dA_l} = \frac{y dy d\theta}{x dx d\theta} = \frac{y}{x} \frac{dy}{dx} = \left(1 - \frac{m(x)}{x^2}\right) \left(1 + \frac{m(x)}{x^2} - \frac{1}{x} \frac{dm(x)}{dx}\right)$$

For a point-source lens, we have  $m(x) = 1$  (in proper units). So we are left with:

$$\mu = \left[ \left(1 - \frac{1}{x^2}\right) \left(1 + \frac{1}{x^2}\right) \right]^{-1} = \left(1 - \frac{1}{x^4}\right)^{-1}$$

The magnification at the respective images is then:

$$\mu_{\pm} = \left| 1 - \frac{1}{x_{\pm}^4} \right|^{-1} = \left| \frac{x_{\pm}^4}{x_{\pm}^4 - 1} \right|. \quad (2.2.11)$$

To gain some intuition of the mapping, then let's assume  $y > 0$  for the moment. If we start separating the lens and the source and look at the asymptotic behaviour of the magnification as  $y \rightarrow \infty$ , then this will make  $x_+ \rightarrow 1$  and  $x_- \rightarrow 0$  implying that the magnification goes like  $\mu_+ \rightarrow 1$  and  $\mu_- \rightarrow 0$ . So asymptotically effectively only one image can be seen, as the other will be extremely demagnified. This makes sense since, in this limit, lensing should become progressively weaker and so asymptotically we would effectively see an untampered image of the source at its actual location.

For smaller  $y$ 's however, both images are visible and their position will also be shifted

---

<sup>4</sup>You can also go the route presented in the previous subsection by finding the Jacobian of the full two-dimensional deflection. This is however needlessly complicated and so a simpler way was chosen here

from the position of the actual source. In general, one of the images will be magnified, while the other will be demagnified by the act of the lens. This opens up the opportunity to study the lens by tracking the magnification of its images. Depending on the strength of the lens, which is encapsulated in the Einstein angle, the images might be able to be resolved separately. In this case, a possible observable is the magnification ratio of the two images  $\frac{\mu_-}{\mu_+}$ . However, when the images cannot be resolved independently all you will see is the total magnification [24]:

$$\mu_p = |\mu_-| + |\mu_+| = \left|1 - \frac{1}{x_-^4}\right|^{-1} + \left|1 - \frac{1}{x_+^4}\right|^{-1} = \frac{y^2 + 2}{y\sqrt{y^2 + 4}}.$$

The total magnification is, in particular, the main observable in microlensing. Since it varies according to  $y$ , then this means an object passing by the line-of-sight will induce magnification of a background source. Tracking the variation of the brightness of a source, through the light curve of that source, then allows the discovery of possible microlensing events. These kinds of microlensing events are rare, however, due to the sheer number of background stars, they can be found by tracking the light curves of a large sample of bright objects. This was particularly done for the large Magellanic cloud — a dwarf galaxy — in order to find evidence of compact sources of dark matter (see e.g. [2]). The microlensing that was just described, will in the rest of the thesis be referred to as 'low-optical depth' microlensing. It distinguishes itself from 'high-optical depth' microlensing by the number of lenses contributing to the microlensing effect. This will be further clarified in the next chapter.

As should now be evident, calculating the magnification is therefore of utmost importance when dealing with microlensing in particular. Consequently, it is important to establish a framework of magnification, which can also be extended to more complex physical setups. This includes extended brightness profiles.

## 2.2.2 Magnification

Another way to define the magnification, which also allows it to be generalized to sources of finite size, is to use the surface brightness distribution. This definition utilizes an important result in gravitational lensing, namely the fact that gravitational lensing does not change the surface brightness of the source [32, See sec. 4.5.1]. Instead, it only changes the apparent surface brightness, i.e. it doesn't create or destroy photons, it only

redistributes them. This means if we have some general surface brightness distribution  $I(y, y_0)$  with  $y_0$  being the center location of the source. Then it holds:

$$I(y, y_0) = I(y(x), y_0), \quad (2.2.12)$$

where  $y(x)$  is the corresponding lens equation. The magnification quantifies the increase or decrease in light reaching the observer due to gravitational lensing. Hence, it should be expressed as the ratio of the flux with lensing to the flux without lensing. It can therefore be written as the ratio [27]:

$$\mu(y_0) = \frac{\int d^2x I(y(x), y_0)}{\int d^2y I(y, y_0)} = \int d^2x I(y(x), y_0), \quad (2.2.13)$$

where in the final step we have chosen the normalization of the surface brightness distribution such that  $\int d^2x I(y(x), y_0) = 1$ . Let's quickly show that this definition coincides with the previous expression for point sources. In the case of a point source, then  $I(y, y_0) = \delta(y - y_0)$ . The magnification will consequently be:

$$\mu(y_0) = \int d^2x \delta(y(x) - y_0) = \sum_i \frac{\delta(x - x_i)}{\det \left[ \frac{\partial y}{\partial x}(x_i) \right]} = \sum_i \delta(x - x_i) \mu(x_i), \quad (2.2.14)$$

where the delta function of a composite function has been reformulated. The  $x_i$  represent the roots of this composite function and are therefore the solutions to the lens equation. The formula indicates that only the locations where the lens equation maps the source's image will contribute to the magnification. This is exactly what we have already seen in our previous definition of the total magnification.

## 2.3 The dominant lens approximation

Apart from describing the magnification, another relevant thing for us is to describe microlensing with lenses consisting of multiple different objects. As we have already seen the lensing of an image can be described through the lens equation (2.2.2). This assumes only the presence of one lens plane with one lens in it. The formula can however easily be generalised to multiple lenses in multiple lens planes [16]:

$$\vec{\beta} = \vec{\theta} - \vec{\alpha} \quad , \quad \vec{\alpha} = \sum_{l=1}^N \frac{D_{ls}}{D_{os}} \vec{\alpha}_l(x_l) \quad (2.3.1)$$

$\beta$  is the unlensed angular position,  $\theta$  is the position of the lensed image and  $\alpha$  is the total deflection angle. As can be seen, the total deflection angle  $\alpha$  is the sum of the deflection of all  $N$  lenses. It is tricky to find since  $x_l$  is immediately dependent on the previous lens position ( $x_{l-1}$ ). This dependence can itself be written in terms of an iteration of lens equations:

$$\vec{x}_l = D_{ol}\vec{\theta} - \sum_{m=1}^{l-1} D_{ml}\vec{\alpha}_m(x_m) \quad (2.3.2)$$

One way to deal with this non-linear recursion is to assume that one lens dominates. This breaks down the total deflection as (See Fleury *et al.* [16]):

$$\vec{\alpha} = \sum_{l < d} \vec{\alpha}_{ols}(\xi_{ol}) + \vec{\alpha}_{ods}(\xi_{od}) + \sum_{l > d} \vec{\alpha}_{ols}(\xi_{ol}) \quad \text{with} \quad \xi_{ol} = \frac{x_l}{D_{ol}}, \quad (2.3.3)$$

where the action of the combined lenses has been decomposed into respectively a background, main and foreground contribution. The background contribution will not be a leading term, as all these lenses perturb the beam much less than the main lens. Therefore their perturbation of the position can be ignored. This lets us use the unperturbed trajectory:

$$\sum_{l < d} \vec{\alpha}_{ols}(\xi_{ol}) \approx \sum_{l < d} \vec{\alpha}_{ols}(\theta) \quad (2.3.4)$$

Similarly, the main lens may also be evaluated on the unperturbed trajectory:

$$\vec{\alpha}_{ods}(\xi_{od}) \approx \vec{\alpha}_{ods}(\theta) \quad (2.3.5)$$

Finally, the foreground contribution does have to take into account how the main lens perturbs the trajectory, it can however ignore the rest:

$$\sum_{l > d} \vec{\alpha}_{ols}(\xi_{ol}) \approx \sum_{l > d} \vec{\alpha}_{ols}(\vec{\theta} - \vec{\alpha}_{odl}(\theta)). \quad (2.3.6)$$

In this way, multi-plane lensing becomes a simpler problem, but it still remains very tough to work with analytically. Therefore we try to make even more simplifying assumptions. In this thesis, we focus on microlensing involving a single galaxy as the primary lens. We also assume that the galaxy's structure contributes to the deflection of light. Given that all perturbers are considered to be located within the galaxy, we treat our problem as one involving multiple perturbers within a single lens plane. This approximation should be somewhat justified by the negligible effect of the galaxy's extent relative to the length of the light trajectory. We will therefore ignore the possible



contribution of potential foreground lenses. In this case, our lens equation is expected to become:

$$\vec{\beta} = \vec{\theta} - \left[ \vec{\alpha}_d(\theta) + \sum_i \vec{\alpha}_i(\theta) \right] \quad (2.3.7)$$

This will be the exact model that is considered in the next section.

# Microlensing

Microlensing is a specific subsection of gravitational lensing that studies how the light curve of a source is affected by gravitational lensing. Unlike strong lensing, which typically produces multiple images of the same source due to a massive gravitational body being close to the line-of-sight, microlensing effects are observed through apparent changes in surface brightness. This is because the gravitational lens(es) causing microlensing is only strong enough to create so-called 'microimages'. Microimages are images being mapped near the source image, also referred to as the 'macroimage', usually on a scale of micro-arcsecond, which means they cannot be resolved individually (See e.g. [21] or [29]). In theory, with perfect resolution, you would be able to see how a macroimage splits up into many microimages, however since this is never the case when discussing microlensing, then the effect of these microimages is instead detectable via changes in the apparent surface brightness. Typical ways of studying microlensing will therefore include monitoring the apparent surface brightness of very luminous objects. This is usually achieved through either a time-series analysis of the source's apparent brightness or, when multiple images can be resolved, by examining whether microlensing affects the flux variance of these images differently.

Microlensing is broadly divided into two regimes [29]:

- **The low-optical depth** regime occurs when a single main perturber is very close to the line-of-sight. This dominant perturber significantly influences the total deflection, allowing the effects of other perturbers to be largely ignored.
- **The high-optical depth regime** is, in contrast, a regime, where the effects of many perturbers play a role. While the influence of each individual perturber is very minimal, their cumulative effect is important. For this reason, this regime tends to be Gaussian in nature, similar to the process of a random walk.

There are multiple ways of trying to describe microlensing mathematically. One particularly popular way is a stochastic model usually referred to as<sup>1</sup> 'the random-star field

---

<sup>1</sup>The name was borrowed by Schneider *et al.* [32]

model'. This approach was in particular pioneered by the works of Katz *et al.* [21], who originally drew inspiration from the work of Chandrasekhar [9], which, among other things, concerns random gravitational fields. Their methods rely on the stochastic description of random flights and a specific solution method called the Holtsmark-Markov method. I will now summarize the idea of this method as well as describe the overall model.

### 3.1 The random star-field

The random star-field gravitational lens system has been studied by numerous authors (see e.g. [11], [12], [21],[27], [32], [33]). This model usually comprises a main (or background) lens perturbed by  $N$  compact objects. Its lens equation can be written as:

$$y = \begin{pmatrix} 1 - \kappa - \gamma_1 & \gamma_2 \\ \gamma_2 & 1 - \kappa + \gamma_1 \end{pmatrix} x + \lambda^2 \sum_{i=1}^N m_i \frac{x - x_i}{|x - x_i|^2}, \quad (3.1.1)$$

where everything has been normalized to appropriate units,  $\lambda^2 = \frac{4GD}{c^2}$ . The main lens, usually taken to be a galaxy, will create one or more macroimages, while the stochastic component, usually thought of as perturbing stars, will split them into microimages. The random star-field model is typically studied in the context of quasars, as these are the brightest sources at high redshift. This makes them some of the most likely objects to be lensed by intervening galaxies. Quasars also have a relatively small extent, which proves to be highly significant in the context of microlensing effects. This is further explored in the next section on surface brightness distributions.

There are many lens models, which could be used as the main lens and which one to use depends on the lensing system. Choosing the correct main lens is particularly important when dealing with strong-lensing systems, in order to account for the correct amount of images and their magnification. The main lens will however not be explicitly dealt with in this thesis. Although it does influence the final observables, these effects are not directly calculated in the thesis, as the relevant expressions are non-analytic and would necessitate numerical simulations.

Since the main lens is *not* stochastic we may completely ignore it for now and move on to explain how we can deal with the stochastic part of this model.

### 3.1.1 Holtsmark–Markov method

We imagine some probability distribution of deflecting with an angle  $\phi$ ,  $P(\phi)$ . In this case,  $\phi$  is a random variable, whose value is unknown to us. As there are many stars in the star-field, we would expect the light ray to scatter multiple times, while traversing through the field. The total deflection of the light ray would then be:

$$\phi = \sum_{i=1}^N \phi_i. \quad (3.1.2)$$

As the  $\phi_i$ 's are stochastic in nature, then we are not able to compute the above sum exactly. However, what we *are* able to do, is to find the probability distribution of  $\phi$ , which in the case of the  $\phi_i$ 's being identically distributed, we may denote  $P_N(\phi)$ . According to probability theory, the distribution of the sum of two random variables is given by the convolution of their probability density functions [31, Chap. 16]:

$$P_{N+1}(\phi) = \int P_1(\phi) P_N(\phi - \theta) d^2\theta, \quad (3.1.3)$$

where since  $\theta$  lies in the lens-plane it needs to be integrated over the entire lens-plane region. In order to compute  $P_N(\phi)$  using the formula above, we would have to conduct  $(N - 1)$  integrals. Fortunately, there is a clever trick to simplify things. This comes from the observation that in Fourier-space, convolutions are simple products:

$$\tilde{\rho}_{N+1} = \tilde{\rho}_N \tilde{\rho}. \quad (3.1.4)$$

Thus simple recursion implies  $\tilde{\rho}_N = (\tilde{\rho}_1)^N$ . This means we can avoid doing all the integrals by instead finding  $\tilde{\rho}_1$ , known in probability theory as the characteristic function, raising it to the N'th power and then transforming it back by an inverse Fourier transformation.

### 3.1.2 The characteristic function of a single scattering

In order to find the probability density function of a single scattering, an expression for the scattering angle as a function of the impact parameter is needed. The cross-section of scattering with an angle greater than  $\phi$  is given by:

$$\sigma(\phi) = \pi b(\phi)^2. \quad (3.1.5)$$

We assume that the star-field has some radius  $R$ , so we only probe regions  $b \leq R$ . This will set the scale for the minimal allowed deflection in our model. This can be denoted  $\phi(R) = \phi_{\text{Min}}$ . Then we can find a cumulative probability density function by a simple area comparison:

$$F(\phi \geq \phi_{\text{Min}}) = \frac{\sigma(\phi)}{\pi R^2} = \frac{b(\phi)^2}{R^2}. \quad (3.1.6)$$

Given an expression for  $b(\phi)$  we can then easily find a probability density function of scattering with an angle  $\phi$  by differentiating the cumulative probability density function. As it will be expected that most of the scatterings will occur with a respectable impact parameter size, then we may assume the deflection angle can be given by that of a point-mass. This is especially true for stars, which will have a very small extent in comparison to the size of their impact parameter. The scattering of a light ray by a point-mass was found in the previous section (2.1.13):

$$\phi_{\text{point}} = \frac{4GM}{bc^2}. \quad (3.1.7)$$

Inverting this relation therefore allows us to find the cumulative distribution:

$$F(\phi \geq \phi_{\text{Min}}) = \frac{b(\phi)^2}{R^2} = \frac{(\frac{4GM}{\phi c^2})^2}{R^2} = (\frac{4GM}{Rc^2})^2 \frac{1}{\phi^2} = \frac{\phi_{\text{Min}}^2}{\phi^2}. \quad (3.1.8)$$

Differentiating the above cumulative distribution function leads to the following probability density function:

$$P(\phi) = \begin{cases} \frac{2\phi_{\text{min}}^2}{\phi^3} & \phi \geq \phi_{\text{min}} \\ 0 & \phi < \phi_{\text{min}} \end{cases}, \quad (3.1.9)$$

Finally, as the deflection should be a two-dimensional vector,  $\phi$  only accounts for the radial direction, we also need a direction in the transverse plane. This is taken to be uniformly distributed, which means the area element is:

$$P(\vec{\phi})d^2\vec{\phi} = P(\phi)d\phi \frac{d\alpha}{2\pi} = \frac{\phi_{\text{min}}^2}{\pi\phi^3}d\phi d\alpha, \quad (3.1.10)$$

where  $\alpha$  is the azimuthal angle and I have emphasised  $\vec{\phi}$  as the two-dimensional deflection vector and  $\phi$  as the magnitude.

We are now interested in calculating the characteristic function of (3.1.9). This can be done by Fourier transforming our probability density function:

$$\begin{aligned}\tilde{\rho}_1 &= \int_0^{2\pi} \int_{\phi_{\min}}^{\infty} P(\vec{\phi}) \exp(-i\vec{k} \cdot \vec{\phi}) d^2\vec{\phi} = \frac{\phi_{\min}^2}{\pi} \int_0^{2\pi} \int_{\phi_{\min}}^{\infty} \frac{1}{\phi^3} \exp(-ik\phi \cos(\alpha)) d\phi d\alpha \\ &= 2\phi_{\min}^2 \int_{\phi_{\min}}^{\infty} \frac{1}{\phi^3} J_0(k\phi) d\phi = 2 \int_1^{\infty} \frac{1}{x^3} J_0(cx) dx,\end{aligned}$$

where the function  $J_0$  is the zeroth Bessel function (of the first kind) and  $c = k\phi_{\min}$ . As a small side note, the Fourier transform presented above is also sometimes referred to as the 'Hankel transformation'. This is because the Hankel transformation can be interpreted as the Fourier transform of a spherically symmetric function. The above integral can be computed analytically, in particular, it can be shown that it is equal to:

$$2 \int_1^{\infty} dx \frac{J_0(xt)}{x^3} = 1 - \frac{c^2 \log(\frac{3.05}{c})}{2} - \frac{c^2}{2} \sum_{n=1}^{\infty} \frac{(-1)^n \left(\frac{c}{2}\right)^{2n}}{2n((n+1)!)^2}, \quad (3.1.11)$$

where the last power-series term is known as a hypergeometric function and the constant 3.05 is an approximation of  $2e^{1-\gamma}$ . While the above expression looks complicated, it turns out that we only need to consider it for small values of  $c$ . This significantly simplifies the result, as it can then be Taylor expanded in  $c$ :

$$\tilde{\rho}_1 = 2 \int_1^{\infty} \frac{dx}{x^3} J_0(cx) = 1 - \frac{c^2}{2} \log\left(\frac{3.05}{c}\right) + o(c^4). \quad (3.1.12)$$

The reason this expansion is justified is not immediately obvious, so I will try to give some intuition for it. The Fourier conjugate variables are  $\{k, \phi\}$  and the mapping from one to the other can be thought of as<sup>2</sup>  $\phi \rightarrow k$ . So small deflection angles correspond to small values of  $k$  and similarly for large values. This means in particular that a Taylor-expansion of  $k$  is well equipped to describe small deflection angles. As we wish to eventually find  $\tilde{\rho}_N$ , which is just  $\tilde{\rho}_1^N$ , then the shape of the function  $\tilde{\rho}_1$  becomes very important. For all values of  $c$ , then it holds that  $\tilde{\rho}_1 \leq 1$ . This means the function gets suppressed nearly everywhere once it is raised to the  $N$ 'th power. Importantly, this suppression is however smallest for the region where  $c$  is small since this is the point where  $\tilde{\rho}_1$  is closest to one. Therefore, for any realistic values of  $N$  ( $N > 10$ ), then the Taylor expansion will be a very good description of small deflection angles. This is in particular showcased in Figure 3.2. The description itself starts breaking down around  $c \sim 3.05$ , as the logarithm forces the second-order term to change signs. This is however an artifact of the neglected terms of order  $o(c^4)$  [32]. The description of larger deflection

<sup>2</sup>This is a consequence of a double inversion, since  $f(\phi) \propto \frac{1}{\phi^3}$  and the usual Fourier conjugate mapping is  $\phi \rightarrow \frac{2\pi}{k}$ .

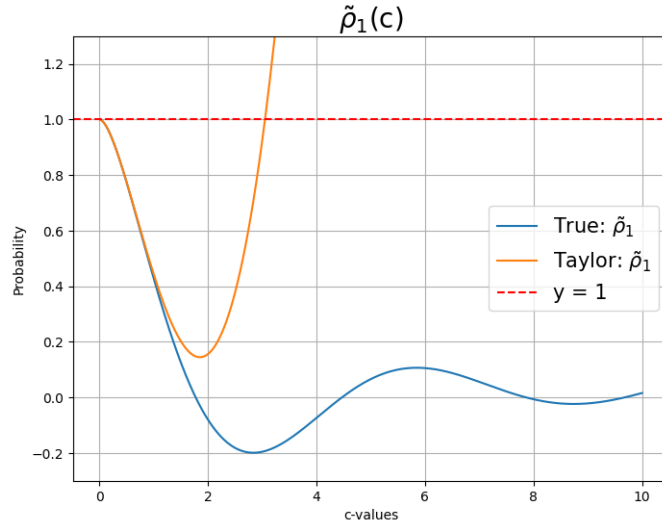


**Figure 3.1:** The behaviour of  $\tilde{\rho}_1$  is shown. As can be seen, the function always remains below one and it quickly starts oscillating around zero. For small  $c$  values the Taylor-expansion fits well, however, it clearly trails off at  $c \sim 1.7$  and completely diverges for values  $c > 2$ . This divergence is an artifact of the neglected high-order terms in the Taylor-expansion

angles can still be encapsulated by using asymptotic expansions. This thesis however mainly concerns itself with the high-optical depth of microlensing, which is precisely described by the smaller deflection angles.

### 3.1.3 Probability distribution of scattering angle after $N$ -deflections

We now return to the problem of finding the actual probability distribution  $P_N(\phi)$ . From the Holtsmark-Markov prescription, we know that we should now raise  $\tilde{\rho}_1$  to the  $N$ 'th power in order to find  $P_N(\phi)$ :

$$\tilde{\rho}_N = \left[ 1 - \frac{c^2}{2} \log \left( \frac{2e^{1-\gamma}}{c} \right) \right]^N \approx \exp \left[ - \frac{Nc^2}{2} \log \left( \frac{3.05}{c} \right) \right]. \quad (3.1.13)$$

The above approximation holds as long as  $N \gg 1$ , which should be valid in all cases. Finally, we transform it back:

$$P_N(\phi) = \frac{1}{2\pi} \int_0^\infty k dk J_0(k\phi) \exp \left[ - \frac{Nk^2\phi_{\min}^2}{2} \log \left( \frac{3.05}{k\phi_{\min}} \right) \right]. \quad (3.1.14)$$

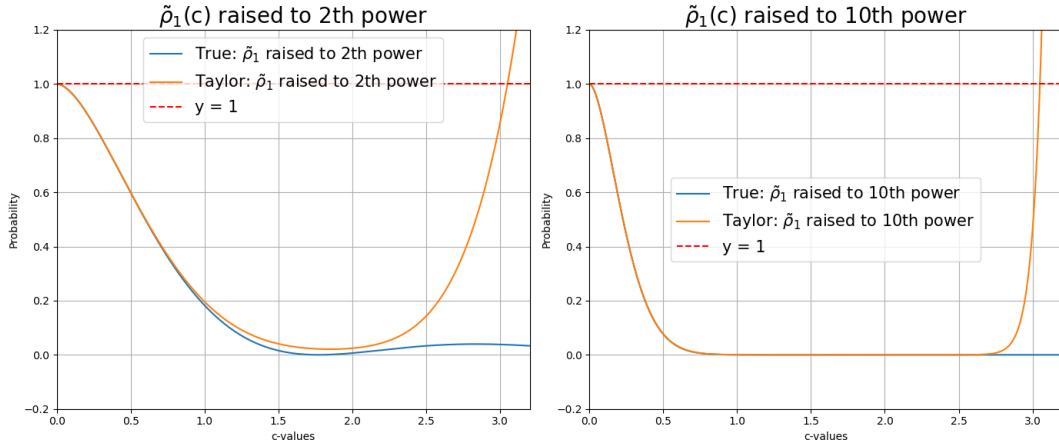


**Figure 3.2:**  $\tilde{\rho}_1$  raised to the 2nd (left) and 10th (right) power. The Taylor approximation becomes better for the smaller  $c$ -values, as  $\tilde{\rho}_1$  is raised to a higher power. Thus the Taylor expansion is an adequate substitution for the true function for any realistic powers of  $N$ . The resemblance however breaks down for larger values of  $c \sim 3.05$ . This is attributed to the truncation of the Taylor-series. Interestingly, it is also somewhat due to the lack of convergence of the probability function, since it does not have a finite variance. Had the probability function instead been  $f(\phi) = \frac{(\alpha-1)}{x^\alpha}$  with  $\alpha > 3$ , then there had been no log-expression and so the Taylor expansion  $\tilde{\rho}_{N,\text{Taylor}}$  would have converged to the  $\tilde{\rho}_{N,\text{True}}$  as  $N \rightarrow \infty$  due to the central limit theorem.

This integral can not be computed analytically, however, it can be calculated in two different regimes. In the low optical-depth regime we will have hit a large deflection angle. This means  $\phi$  will be much larger than the typical deflection, i.e.  $\phi \gg \phi_0$ , where  $\phi_0 = (N\phi_{\text{Min}})^{\frac{1}{2}}$ . In this case, the resulting deflection probability can be shown to look like [21]:

$$P_N(\phi \rightarrow \infty) = \frac{\phi_0^2}{\pi\phi^4}. \quad (3.1.15)$$

The reason it looks like this is fairly simple, as this would be the probability of one of the deflections being very large. A nice argument can be presented as follows [32, Sec. 11.2.1]. The probability of picking a scattering angle greater than  $\alpha$  is simply given by the cumulative probability density  $F(\alpha) = \frac{\phi_{\text{Min}}^2}{\alpha^2}$ . This can then be related to the probability density function by differentiation:

$$\begin{aligned} F(\alpha) &= 2\pi \int_{\alpha}^{\infty} \phi d\phi p(\phi) \\ \Rightarrow p(\alpha) &= \frac{1}{2\alpha} \frac{d}{d\phi} \left( -F(\phi) \right) \Big|_{\phi=\alpha} = \frac{\phi_{\text{Min}}^2}{\pi\alpha^4}. \end{aligned}$$

Precisely in the low-optical depth limit, where one deflection will dominate, we may linearly extrapolate this result, which means the total deflection angle will be the sum



of all the deflection angles. Therefore this explains why the result for the low-optical depth case is  $P_N(\phi) = \frac{N\phi_{\text{Min}}^2}{\pi\phi^4}$ .

On the other hand, the high-optical depth regime will instead yield a Gaussian:

$$P_N(\phi) = \frac{1}{2\pi\sigma^2} \exp\left(-\frac{\phi^2}{2\sigma^2}\right) \quad , \quad \sigma^2 = \phi_0^2 \log(3.05N) \quad (3.1.16)$$

The fact that the high-optical regime is a Gaussian should come as no surprise. As stated earlier, one might think of this regime, where the deflection of many perturbers is roughly equal, as a random walk or diffusion process. The solution to such processes is Gaussian and so this is therefore a natural explanation. More mathematically such problems can be framed in terms of the central limit theorem. The probability density function (3.1.9) does not have a finite variance. Therefore the central limit theorem would not apply to  $P_N(\phi)$ . However, in the case where you only consider the smaller deflections  $\phi \lesssim \phi_0$ , then there certainly is a finite variance. This would mean the sum of such deflections would be Gaussian in accordance with the central limit theorem.

Currently, we have only considered the case, where all the deflection masses are the same. The above results can however be generalized to an arbitrary mass spectrum.

### 3.1.4 Introducing a mass spectrum

We now turn to the situation, where each scattering center has a different mass  $M$ . This can be done quite similarly as in the previous subsection. This time we assume that there are  $N_i$  scattering centers with mass  $M_i$ . This will not change the expression in (3.1.12). Instead we can denote it as  $\tilde{\rho}_1(M_i)$ . Instead of raising this to the  $N$ 'th power, we multiply  $N$  iterations of  $\tilde{\rho}_1(M_i)$  together and collect those with the same mass:

$$\tilde{\rho}_N = \prod_{i=1}^N \tilde{\rho}_1(M_i) = [\tilde{\rho}_1(M_1)]^{N_1} [\tilde{\rho}_1(M_2)]^{N_2} \dots \quad , \quad (3.1.17)$$

where  $N_i$  designates the amount of scattering centers with the mass  $M_i$ . This can be put into a more convenient form by taking the logarithm:

$$\log(\tilde{\rho}_N) = \sum_i N_i \log(\tilde{\rho}_1(M_i)). \quad (3.1.18)$$

Taking this into the continuum-limit, we swap out the sum for an integral:

$$\log(\tilde{\rho}_N) = \int N(M) \log(\tilde{\rho}_1(M)) dM, \quad (3.1.19)$$

with  $N(M)$  being the mass-density. In this step, extra care needs to be taken as such a limit implicitly assumes that every mass in the spectrum is somewhat attainable. This, in particular, becomes important if the mass spectrum is very wide and steep like for instance  $\frac{dN}{dm} \propto m^{-\beta}$  for  $m \in [M_{\text{Min}}, M_{\text{Max}}]$ . In the context of dark matter subhalos the difference between  $M_{\text{Min}}$  and  $M_{\text{Max}}$  may span over ten orders of magnitude and it follows the aforementioned mass spectrum [34]. It is therefore a particularly relevant discussion for dark matter subhalos, which will be held in the next chapter. In the case of a star-field, the largest and smallest stars are usually within a couple of orders of magnitudes in mass. Therefore this subtlety won't be a big issue when considering the light deflection of stars.

From here, most of the work is done, since we already know that  $\tilde{\rho}(M) = 1 - \frac{c(M)^2}{2} \log\left(\frac{2e^{1-\gamma}}{c(M)}\right)$ . It is important to note that  $c$  is dependent on  $M$  because of  $\phi_{\text{Min}}$ . This therefore means:

$$\begin{aligned} \tilde{\rho}_N &= \exp \left[ \int N(M) \log \left( 1 - \frac{c(M)^2}{2} \log \left( \frac{2e^{1-\gamma}}{c(M)} \right) \right) dM \right] \\ &\approx \exp \left[ - \int N(M) \frac{k^2 \phi_{\text{Min}}(M)^2}{2} \log \left( \frac{2e^{1-\gamma}}{k \phi_{\text{Min}}(M)} \right) dM \right], \end{aligned}$$

where in the second line we used the approximation  $\log(1 - x) \approx -x$ . Finally, we want to again do a back-transform. Following similar derivations as in the previous section, this will lead to the updated version of (3.1.14):

$$P_N(\phi) = \frac{1}{2\pi \langle \phi_0^2 \rangle} \int_0^\infty x dx J_0 \left( \frac{x\phi}{\langle \phi_0^2 \rangle^{\frac{1}{2}}} \right) \exp \left[ - \frac{x}{2} \log \left( \frac{3.05 f N^{\frac{1}{2}}}{x} \right) \right]. \quad (3.1.20)$$

Again this leads to the same two regimes as those found in (3.1.16) and (3.1.15). The formulas originally derived in Katz *et al.* [21, eq. 23-24] are as follows:

$$P_N(\phi) = \begin{cases} \frac{\langle \phi_0^2 \rangle}{\pi \phi^4} & \phi \gg \phi_0 \\ \frac{1}{2\pi \sigma^2} \exp \left( - \frac{\phi^2}{2\sigma^2} \right) & \phi \lesssim \phi_0 \end{cases}, \quad (3.1.21)$$

where:

$$\sigma^2 = \langle \phi_0^2 \rangle \log(3.05f) \quad (3.1.22)$$

$$\langle \phi_0^2 \rangle = \left( \frac{4G}{c^2} \right)^2 \cdot \frac{N \langle M^2 \rangle}{R^2} \quad (3.1.23)$$

$$f = \left( N \langle M^2 \rangle \right)^{\frac{1}{2}} \exp \left( - \frac{\langle M^2 \log(M) \rangle}{\langle M^2 \rangle} \right). \quad (3.1.24)$$

These formulas' dependence on mass can be framed in terms of  $N \langle M^2 \rangle$ . This will become important once we consider microlensing for various types of substructures. Interestingly, this exact dependence on the mass variance,  $\langle M^2 \rangle$ , while being independent of, for instance, the mean mass  $\langle M \rangle$  turns out to be a consequence of the distribution (3.1.9). This will be shown in the next chapter.

Finally, it is now of particular interest to see how such a description of microlensing would appear through actual observables.

## 3.2 Surface brightness distribution

The consideration of how high-optical depth microlensing affects the surface brightness distribution was first done in the seminal paper Deguchi and Watson [12]. They used the principle of surface brightness conservation to derive the resulting equation for the flux magnification. Their equation is equivalent to the equation (2.2.13). Inserting the random star-field lens equation (3.1.1) then amounts to finding the flux magnification due to microlensing<sup>3</sup>. Given that the random star-field model consists of a main lens and an inherently stochastic component attributed to microlensing, the impact of microlensing relative to the main lens can be quantified using moments of the flux magnification. To find the various moments of the flux magnification, the brightness profile needs to be specified. The simplest profile of an extended source with size  $\sigma_W$  is a Gaussian surface brightness profile:

$$I(y, y_0) = \frac{1}{\pi \sigma_W^2} \exp \left( - \frac{(y - y_0)^2}{2 \sigma_W^2} \right). \quad (3.2.1)$$

---

<sup>3</sup>Their lens equation did not have a main lens, however, this has later been done by Dai and Pascale [11]

Embedding the lens equation into our surface brightness profile will then give the following flux magnification:

$$\mu(y) = \frac{1}{\pi\sigma_W^2} \int d^2x \exp\left(-\frac{(x-y-Mx+\phi)^2}{2\sigma_W^2}\right), \quad (3.2.2)$$

where  $M$  is the main lens matrix,  $y$  is the position of the unlensed source and  $\phi$  is the sum of all the stochastic deflections from stars. A convenient way to rewrite this is by using a Fourier transform, as this allows for the separation of the stochastic part:

$$\mu(y) = \int d^2x \int \frac{d^2l}{(2\pi)^2} \exp(-il(x-y-Mx+\phi)) \tilde{I}(l), \quad (3.2.3)$$

where  $\tilde{I}(l)$  is the Fourier transform of the surface brightness distribution. It is now feasible to find expressions for various moments of the magnification distribution. For the two first moments, they are as follows [11]:

$$\begin{aligned} \langle \mu(y) \rangle &= \int d^2x \int \frac{d^2l}{(2\pi)^2} \exp(-il(x-y-Mx)) \tilde{I}(l) \langle e^{-il\phi(x)} \rangle \\ \langle \mu(y)^2 \rangle &= \int d^2x_1 \int \frac{d^2l_1}{(2\pi)^2} \int d^2x_2 \int \frac{d^2l_2}{(2\pi)^2} e^{-i(l_1(x_1-y-Mx_1)-l_2(x_2-y-Mx_2))} \\ &\quad \times \tilde{I}(l_1) \tilde{I}(l_2) \langle e^{-i(l_1\phi(x_1)+l_2\phi(x_2))} \rangle, \end{aligned}$$

where  $\langle \dots \rangle$  denotes averaging over the probability distribution. Since  $P_N(\phi)$  was found in the previous section, it can be used immediately to find the average of the stochastic term:

$$\langle e^{-il\phi(x)} \rangle = \int d^2\phi \exp(il\phi) \frac{1}{2\pi\sigma_{\text{ML}}^2} \exp\left(-\frac{\phi^2}{\sigma_{\text{ML}}^2}\right) = \exp(-\sigma_{\text{ML}}^2 l^2). \quad (3.2.4)$$

It should be noted that in this definition of  $\sigma_{\text{ML}}$  the effective distance is included, i.e:

$$\sigma_{\text{ML}}^2 = D^2 \sigma^2 \quad \text{with} \quad D = \frac{D_{ds} D_D}{D_s}, \quad (3.2.5)$$

where  $\sigma$  is given by (3.1.22). With this in mind, we are now able to calculate  $\langle \mu(y) \rangle$ . The Fourier transform of a Gaussian is another Gaussian, which means  $\tilde{I}(l)$  will also be a Gaussian. The expression can be shown to take the form [11]:

$$\langle \mu(y) \rangle = \frac{1}{2\pi(\sigma_{\text{ML}}^2 + \sigma_W^2)} \int d^2x \exp\left(-\frac{1}{2} \frac{|x-y-Mx|^2}{\sigma_{\text{ML}}^2 + \sigma_W^2}\right). \quad (3.2.6)$$

Therefore the average of the magnification should be sensitive to microlensing if  $\frac{\sigma_{\text{ML}}^2}{\sigma_W^2} > 1$ . This is ultimately going to be the final ratio of concern to determine whether a physical

setup has a chance to be visible. Of course, the above equation is still very idealized, as it does not take into account any smearing of the telescope's picture.

The second moment can also be found if some assumptions are made in regards to the correlation function of the perturbors  $\langle \phi(x_1)\phi(x_2) \rangle$ . I will however skip this result and instead refer to the paper Dai and Pascale [11] and their equation (12) and (37) show that such a function can indeed be found after much work.

Since any actual calculation of  $\langle \mu(y) \rangle$  and  $\langle \mu(y)^2 \rangle$  would likely have to be made numerically, especially for non-simple models of the main lens, I will not go any further with these quantities in this thesis. Instead, their importance will be the fact that any fluctuations in the apparent brightness

$$\sigma_\mu = \sqrt{\langle \mu(y)^2 \rangle - \langle \mu(y) \rangle^2}, \quad (3.2.7)$$

is an actual observable that could be measured for a given quasar. As such our main concern is whether microlensing effects could play a role in the size of these fluctuations. Deguchi and Watson were the first to look into this and their conclusion was that these fluctuations were small for stars, since the average beam size of the light,  $\frac{4GMD}{c^2}$ , was very small in comparison to the typical size of quasars  $\sigma_W$ . While they do maintain the belief that such fluctuations by stars might be possible to see [12], they still stress that it will be a small effect even in an optimal setup. This is, however, predicated on the fact, that the masses of the stars are around the magnitude of  $1M_{\text{sun}}$ . This therefore brings us to dark matter subhalos.

Dark matter subhalos is another abundant source of microlenses in galaxies. Gravitational microlensing by dark matter has already been considered by many different sources, most notably the MACHO and OGLE project (see e.g. [2], [26] and [35]) and Paczynski [30]. In these experiments, they monitor the light curves of many millions of stars to see if any of them occasionally experience significant amplification. In such a case, it might be hypothesised that a compact object has crossed the line-of-sight or very close to it. Although such events are rare, then the sheer number of tracked events will compensate for their rarity. These experiments therefore use low-optical depth microlensing to try and probe dark substructure.

The use of high-optical depth microlensing is, on the other hand, much less prominent. Contrary to low-optical depth microlensing, high-optical depth microlensing events should be much more prominent. The challenge, however, is that these effects are less visible and, thus, harder to accurately identify. This difficulty arises because most

sources exhibit intrinsic variations in their surface brightness profiles. Consequently, distinguishing between fluctuations caused by microlensing and those due to intrinsic variations can be quite difficult. There are a few sources, which look at the compound effect of gravitational lensing (See e.g. [20], [22] and [25]). These do not utilize the specific framework of microlensing introduced in this chapter, but still express the same idea that the cumulative effect of many small gravitational perturbations may lead to an observable magnification of the source. Therefore their considerations have been a source of inspiration for the coming section on substructure microlensing.

# Substructure Microlensing

We will now think of a physical setup with the light from a distant Quasar being lensed by some intervening galaxy. The galaxy itself will be encompassed by a dark matter (host) halo, which itself consists of a core surrounded by many smaller subhalos dispersed within its area. The core of the host halo will be the main lens of our setup, whereas the microlensing components come from all the subhalos dispersed throughout the host halo. To distinguish this model from the random star field model, it will from now on be referred to as the 'random halo-field model'. In this halo-field model, there are some very obvious differences to the star-field model.

- **The masses** of the heaviest subhalos are significantly greater than the masses of the largest stars  $M_{\text{sub, max}} \gg M_{\text{star, max}}$ .
- **The area** of the host halo is around an order of magnitude larger than the area of the galaxy itself [23].
- **The mass spectrum** of subhalos is very steep,  $n(m) \propto m^{-\beta}$  with  $\beta \sim 1.9$  [34], and contains a large range of masses, particularly for CDM models. This is in contrast to stars, which have a smaller range of masses and probably also have a less steep mass spectrum.
- **The size** of subhalos is much larger than the size of stars. It might therefore be the case that subhalos cannot be considered point-like.

From the high-optical depth case of the random star-field (3.1.21) it was found that the dependence of mass is through  $N\langle M^2 \rangle$ . If the spectrum of subhalos is used, then this will depend on:

$$N\langle M^2 \rangle = \int_{M_{\text{Min}}}^{M_{\text{Max}}} M^2 \frac{dN}{dM} dM = \frac{10m_*(M_{\text{Max}}^{1.1} - M_{\text{Min}}^{1.1})}{11} \approx \frac{10m_*}{11} M_{\text{Max}}^{1.1}, \quad (4.0.1)$$

therefore the fact that subhalos can reach far higher masses would suggest a larger effect. This will be somewhat compensated by the subhalos being spread over a larger area making the halo-field less dense in terms of numbers than the star-field. This does

however still not change the fact that the random star field model would suggest that the subhalos should dominate the overall microlensing effects. To see this, we know that the flux magnification dependence on microlensing can be summed up in the parameter  $\sigma_{\text{ML}}$ . As such the ratio can be found:

$$\frac{\sigma_{\text{ML, halos}}}{\sigma_{\text{ML, stars}}} \approx \frac{N_{\text{halos}} \langle M_{\text{halos}}^2 \rangle}{N_{\text{stars}} \langle M_{\text{stars}}^2 \rangle} \frac{R_{\text{gal}}}{R_{\text{halo}}}. \quad (4.0.2)$$

Using the values provided in eq. 4 from the paper [34], would suggest:

$$N_{\text{halos}} \langle M_{\text{halos}}^2 \rangle = \int_{M_{\text{Min}}}^{M_{\text{Max}}} dM a_0 \left( \frac{M}{m_0} \right)^{-1.9} M^2 \sim 10^{19} M_{\odot}^2, \quad (4.0.3)$$

where it was used  $M_{\text{Max}} = 10^9 M_{\odot}$ . The number of stars in the milky-way is on the order of  $10^{11}$ , so even if  $\langle M_{\text{stars}}^2 \rangle = 100 M_{\odot}^2$ , then it would still hold that  $\frac{\sigma_{\text{ML, halos}}}{\sigma_{\text{ML, stars}}} \gg 1$ .

In order to truly adapt the random star-field model to subhalos, all of the mentioned differences between stars and subhalos need to be assessed. In the following sections, we try to account for some of these possible differences and which effect they might have on the model. Of particular interest is also whether it would be possible to use the halo-field model to distinguish between different dark matter models.

## 4.1 Mass spectrum considerations

As mentioned before, among other things, the random halo-field model deviates from the random star-field through the mass spectrum. Due to the very steep nature of the subhalo mass spectrum and especially its significantly wide length, it should be asked whether the continuum-limit taken in the star-field model (3.1.19) is actually a valid approximation in the halo-field model. This is because the random star-field model does not account for the discrete nature of this problem. Instead it, for instance, allows us to encounter a fractional amount of subhalos, which becomes problematic if the fraction is on the order of one. The justification for why this could be a potential issue is clear: the absence/addition of a higher mass subhalo from the mass spectrum has a significantly greater effect on the final deflection than the absence/addition of a smaller subhalo. Additionally, due to the scarcity of large subhalos, then the expected number of them is somewhat uncertain in a given sample. Therefore if we track the deflection of a thousand light beams going through the random halo-field it might be the case that only one of them actually encounters one of the largest subhalos. In this case, this one light



beam would be substantially more deflected than the average light beam and therefore would not show up in the diffuse (Gaussian) part of deflection probability distribution  $P_N(\phi)$ . This phenomenon has been illustrated in Figure 4.1. For this figure, a hundred random variables following the mass distribution<sup>1</sup>  $m^{-\beta}$ , where  $m \in [M_{\text{Min}}, M_{\text{Max}}]$  have been generated and summed up. The difference between the two curves is only the value of  $M_{\text{Max}}$ . It is however clear that the curve with  $M_{\text{Max}} = 100$  is very close to a Gaussian, whereas the second curve with  $M_{\text{Max}} = 1000$  has more visible tails illustrating that it is only a Gaussian for the smaller deflections. Since we only care about the diffuse part of the deflection function and its standard deviation, which encapsulates the strength of the microlensing, then we will have to compare the standard deviations of the two Gaussians. A way to do this is to find the cut-off — the point where after the deflection function can no longer be thought of as Gaussian — and compare them. The cut-off should be able to be expressed as some relationship between  $N$  and  $M_{\text{Max}}$  (and likely  $M_{\text{Min}}$ ). If it is possible to understand this behaviour, then it might mean we are

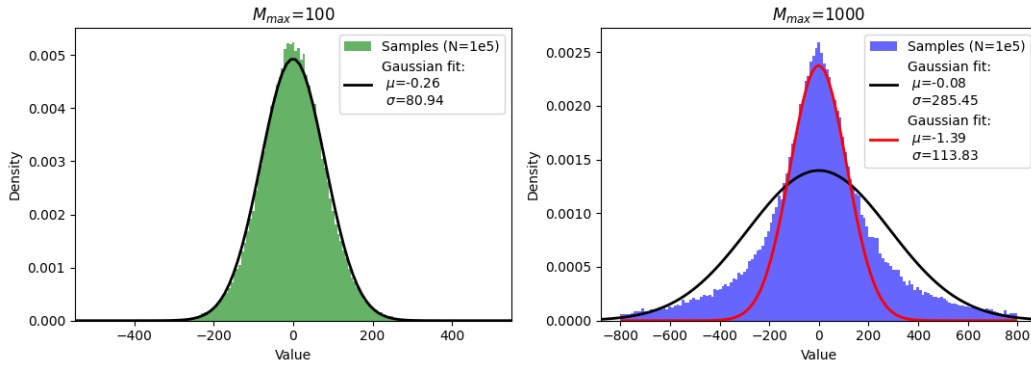


**Figure 4.1:** This illustration shows two histograms of ten thousand samples. Each sample is the sum of a hundred (bounded) Pareto distributed variables with upper bound  $M_{\text{Max}}$  and scale  $\alpha = 1$ . For the left histogram, this bound is  $M_{\text{Max}} = 100$ , while for the right the bound is  $M_{\text{Max}} = 1000$ . It is clear the left histogram is very close to a Gaussian, while the right histogram only looks Gaussian for smaller values. This might indicate that some of the largest masses only affect the tails and so can be disregarded when only looking at the Gaussian part of the deflection function.

able to find an effective mass,  $M_*$ , which should be considered a new upper bound. To try and describe this effect, it has been tried to devise a new framework of the random star-field. This framework considers the probability density distribution of a deflection,  $P(\phi)$  as the ratio of two random variables: The mass ( $m$ ) and the impact parameter ( $b$ ), rather than only considering the impact parameter distribution. This allows for the discreteness of the halo-field to be taken into account.

<sup>1</sup>They have also been made 2D by multiplying them with cosine to a random angle

### 4.1.1 A new formalism for stochastic scattering

The impact parameter distribution can be defined through its cumulative distribution (3.1.6):

$$g(b) = \frac{d}{db}G(B) = \frac{d}{db}\left(\frac{b^2}{R^2}\right) = \frac{2b}{R^2} \quad , \quad b \in [0, R] \quad (4.1.1)$$

Whereas the mass spectrum can be defined through  $\frac{dN}{dM}$ , which is a quantity that has been found through large-scale dark matter simulations (See e.g. [34, eq. 4]):

$$f(m) = \frac{m_0}{m^\beta} \quad , \quad m \in [M_{\text{Min}}, M_{\text{Max}}] \quad (4.1.2)$$

where  $m_0$  is a normalization constant. In this specific case it is equal to  $m_0 \approx (\beta-1)M_{\text{Min}}^{\beta-1}$ . To find the probability distribution of  $\phi = \frac{m}{b}$ , the ratio distribution needs to be found. The ratio distribution of the random variable  $Z$ , which is the ratio of the two random variables  $X$  and  $Y$  is the probability of picking  $X, Y$  s.t.  $Z = \frac{X}{Y}$ . For a given  $Z$ , we therefore wish to sum up all combinations of  $X$  and  $Y$ , which gives this value. This is the intuition behind the following formula for the ratio distribution<sup>2</sup>:

$$\begin{aligned} f_Z(z) &= \int_{-\infty}^{\infty} dy \int_{-\infty}^{\infty} dx f_X(x) f_Y(y) \delta\left(z - \frac{x}{y}\right) = \int_{-\infty}^{\infty} dy \int_{-\infty}^{\infty} dx f_X(x) f_Y(y) |y| \delta(yz - x) \\ &= \int_{-\infty}^{\infty} dy f_X(yz) f_Y(y) |y| , \end{aligned}$$

where in the second step the scaling relation of the delta function was used  $\delta(\alpha x) = \frac{\delta(x)}{|\alpha|}$ . This means the ratio distribution can be written:

$$P(\phi) = \int_{b_1}^{b_2} db f(b\phi) g(b) |b| , \quad (4.1.3)$$

where the limits have intentionally been left as undetermined. These limits have to be determined using the intervals of the two probability distributions (4.1.1) and (4.1.2). Particularly it holds:

$$M_{\text{Min}} \leq m \leq M_{\text{Max}} \quad \implies \quad \frac{M_{\text{Min}}}{\phi} \leq b \leq \frac{M_{\text{Max}}}{\phi} , \quad (4.1.4)$$

which has to be used in addition to the requirement  $b \in [0, R]$ . This splits the probability distribution  $P(\phi)$  into two regimes.

---

<sup>2</sup>See e.g. [31] page 644 for a derivation of the product distribution. A similar argument can easily be used for the ratio distribution

- **For small deflections** ( $\phi < \frac{M_{\text{Max}}}{R}$ )

Then it will hold that  $R < \frac{M_{\text{Max}}}{\phi}$ , which therefore implies that  $b \in [\frac{M_{\text{Min}}}{\phi}, R]$

- **For large deflections** ( $\phi \geq \frac{M_{\text{Max}}}{R}$ )

Then it will instead hold that  $R \geq \frac{M_{\text{Max}}}{\phi}$ , which means  $b \in [\frac{M_{\text{Min}}}{\phi}, \frac{M_{\text{Max}}}{\phi}]$

A quick sanity check shows that any deflection,  $\phi < \frac{M_{\text{Min}}}{R}$ , would not be possible, as this would invalidate the interval in the first case. This now means that the ratio distribution can be computed:

$$P(\phi) = \int_{b_1}^{b_2} db \frac{m_0}{(b\phi)^\beta} \frac{2b}{R^2} = \frac{2m_0}{R^2\phi^\beta} \int_{b_1}^{b_2} db b^{2-\beta} = \frac{2m_0}{R^2\phi^\beta} \left[ \frac{b^{3-\beta}}{3-\beta} \right]_{b_1}^{b_2}. \quad (4.1.5)$$

Inserting the boundaries then gives:

$$P(\phi) = \begin{cases} \frac{2m_0}{(3-\beta)R^2} \left[ \frac{R^{3-\beta}}{\phi^\beta} - \frac{M_{\text{Min}}^{3-\beta}}{\phi^3} \right] & \frac{M_{\text{Min}}}{R} \leq \phi < \frac{M_{\text{Max}}}{R} \\ \frac{2m_0}{(3-\beta)R^2} \frac{1}{\phi^3} \left[ M_{\text{Max}}^{3-\beta} - M_{\text{Min}}^{3-\beta} \right] & \frac{M_{\text{Max}}}{R} \leq \phi < \infty \end{cases}. \quad (4.1.6)$$

This can be written more elegantly using a few relations. Since  $M_{\text{Max}} \gg M_{\text{Min}}$ , then the  $M_{\text{Min}}$  term in the large deflection case may be ignored. It can also be inserted that  $m_0 = (\beta - 1)M_{\text{Min}}^{\beta-1}$ . Finally, by defining  $\phi_{\text{Min}} = \frac{M_{\text{Min}}}{R}$  and making the change of variables to  $x = \frac{\phi}{\phi_{\text{Min}}}$  the above formula can be rewritten into:

$$P(x)dx = \begin{cases} \frac{2(\beta-1)}{(3-\beta)} \left[ \frac{1}{x^\beta} - \frac{1}{x^3} \right] dx & x < \frac{M_{\text{Max}}}{M_{\text{Min}}} \\ \frac{2(\beta-1)}{(3-\beta)} \left( \frac{M_{\text{Max}}}{M_{\text{Min}}} \right)^{3-\beta} \frac{dx}{x^3} & x \geq \frac{M_{\text{Max}}}{M_{\text{Min}}} \end{cases}. \quad (4.1.7)$$

Since ( $x > 1$ ), then we may, to a good approximation, think of the above function as:

$$P(x)dx \approx \begin{cases} \frac{2(\beta-1)}{(3-\beta)} \frac{dx}{x^\beta} & x < \frac{M_{\text{Max}}}{M_{\text{Min}}} \\ \frac{2(\beta-1)}{(3-\beta)} \left( \frac{M_{\text{Max}}}{M_{\text{Min}}} \right)^{3-\beta} \frac{dx}{x^3} & x \geq \frac{M_{\text{Max}}}{M_{\text{Min}}} \end{cases}, \quad (4.1.8)$$

in this case, it should be very clear that the probability density distribution is biased towards smaller deflections, as it is less steep for  $x < \frac{M_{\text{Max}}}{M_{\text{Min}}}$  than it is otherwise. The interpretation of the above formula is that deflections below the scale  $\frac{M_{\text{Max}}}{M_{\text{Min}}}$  can be achieved both through variations in mass and impact parameter, while deflections above this scale can only be obtained with a small impact parameter. In addition, the fact that deflections below the scale  $\frac{M_{\text{Max}}}{M_{\text{Min}}}$  can be closely approximated as  $\frac{1}{x^\beta}$  indicates that the impact parameter distribution has a negligible effect in this range. The reason is due to the mass distribution being less steep than the impact parameter distribution.

Interestingly, making the distributions more similar in terms of steepness will make the final result more dependent on the lower-mass spectrum. This is considered in the next section.

Following the procedure of the random star field, in order to find  $P_N(\phi)$  the integral has to be computed:

$$\tilde{\rho}_1 = \frac{2(\beta - 1)}{(3 - \beta)} \int_1^{\frac{M_{\text{Max}}}{M_{\text{Min}}}} dx J(cx) \left( \frac{1}{x^\beta} - \frac{1}{x^3} \right) \quad (4.1.9)$$

$$\tilde{\rho}_2 = \frac{2(\beta - 1)}{(3 - \beta)} \left( \frac{M_{\text{Max}}}{M_{\text{Min}}} \right)^{3-\beta} \int_{\frac{M_{\text{Max}}}{M_{\text{Min}}}}^\infty dx \frac{J(cx)}{x^3}, \quad (4.1.10)$$

with  $c = k \left( \frac{4GM_{\text{Min}}}{Rc^2} \right)$ . The above characteristic functions have been separated into two, because a given event may only fall within one of the cases of (4.1.7). The probability to fall within the second case is then given by  $p = \frac{I_2}{I_1 + I_2}$  with  $I_1$  and  $I_2$  being the integrals of the two cases respectively (i.e. (4.1.7)). For any event that falls in the first case a random variable is generated from  $I_1$ , while if it falls into the second case it will be generated by  $I_2$ . This therefore justifies why  $\tilde{\rho}_N$  should take the form of a binomial:

$$\tilde{\rho}_N = \sum_{n=1}^N \binom{N}{n} (1-p)^n p^{N-n} [\tilde{\rho}_1]^n [\tilde{\rho}_2]^{N-n}, \quad (4.1.11)$$

where  $N$  is the total number of events,  $n$  is the number of events falling into the first case and  $p$  is the probability of this occurring. The above formula holds as long as the random variables in either case are properly normalized:

$$I_1 = \frac{2(\beta - 1)}{(3 - \beta)} \int_1^{\frac{M_{\text{Max}}}{M_{\text{Min}}}} dx \left[ \frac{1}{x^\beta} - \frac{1}{x^3} \right] \approx 1 - \frac{2}{(3 - \beta)} \left( \frac{M_{\text{Max}}}{M_{\text{Min}}} \right)^{1-\beta} + o\left( \frac{M_{\text{Min}}}{M_{\text{Max}}} \right)$$

$$I_2 = \frac{2(\beta - 1)}{(3 - \beta)} \left( \frac{M_{\text{Max}}}{M_{\text{Min}}} \right)^{(3-\beta)} \int_{\frac{M_{\text{Max}}}{M_{\text{Min}}}}^\infty \frac{dx}{x^3} = \frac{(\beta - 1)}{(3 - \beta)} \left( \frac{M_{\text{Max}}}{M_{\text{Min}}} \right)^{1-\beta}$$

Thus  $\tilde{\rho}_1$  can be considered normalized, while  $\tilde{\rho}_2$  cannot. This means  $\tilde{\rho}_2$  should be divided by  $I_2$ . The probability itself to select events in the second case can be found simply as:

$$p = \frac{I_2}{I_1 + I_2} \approx \frac{\beta - 1}{3 - \beta} \left( \frac{M_{\text{Min}}}{M_{\text{Max}}} \right)^{\beta-1}, \quad (4.1.12)$$

where it was assumed that  $\frac{M_{\text{Max}}}{M_{\text{Min}}} \gg 1$ . This tells exactly that in the case  $N \left( \frac{M_{\text{Min}}}{M_{\text{Max}}} \right)^{\beta-1} < 1$ , then (practically) all samples are expected to fall within the first case. It is therefore instructive to see what happens in this regime.

### 4.1.2 The non-Gaussian behaviour for small N

In this regime  $\tilde{\rho}_N$  can be taken as  $\tilde{\rho}_N = [\tilde{\rho}_1]^N$ . This therefore only requires us to focus on  $\tilde{\rho}_1$ . To fourth order we may write  $\tilde{\rho}_1$  as:

$$\tilde{\rho}_1 \approx 1 - c^2 \frac{45}{121} \left( \frac{M_{\text{Max}}}{M_{\text{Min}}} \right)^{\frac{11}{10}} + \frac{45}{5456} c^2 \left( \frac{M_{\text{Max}}}{M_{\text{Min}}} \right)^{\frac{31}{10}} + o(c^6). \quad (4.1.13)$$

The second-order expression is responsible for the Gaussian behaviour of the smaller deflection angles, while higher-order terms mostly affect the tail of the distribution. It is therefore interesting to see how the next-to-leading order term affects the Gaussian. To see this  $\tilde{\rho}_N$  is found:

$$\tilde{\rho}_N \approx \exp \left[ - \frac{45}{121} N c^2 \left( \frac{M_{\text{Max}}}{M_{\text{Min}}} \right)^{\frac{11}{10}} \left( 1 - \frac{11}{496} c^2 \left( \frac{M_{\text{Max}}}{M_{\text{Min}}} \right)^2 \right) \right] \quad (4.1.14)$$

This can be Taylor expanded for  $c \ll 1$ :

$$\tilde{\rho}_N \approx \exp \left[ - \frac{45}{121} N c^2 \left( \frac{M_{\text{Max}}}{M_{\text{Min}}} \right)^{\frac{11}{10}} \right] \left( 1 + N \frac{45}{5456} c^4 \left( \frac{M_{\text{Max}}}{M_{\text{Min}}} \right)^{\frac{31}{10}} \right) \quad (4.1.15)$$

Finally, an inverse-Fourier transform must be deployed to find  $P_N(\phi)$ :

$$\begin{aligned} P_N(\phi) &= \frac{1}{2\pi} \int_0^\infty k dk J_0(k\phi) \exp \left[ - \frac{45}{121} N k^2 \phi_{\text{Min}}^2 \left( \frac{M_{\text{Max}}}{M_{\text{Min}}} \right)^{\frac{11}{10}} \right] \left( 1 + N \frac{45}{5456} k^4 \phi_{\text{Min}}^4 \left( \frac{M_{\text{Max}}}{M_{\text{Min}}} \right)^{\frac{31}{10}} \right) \\ &= \frac{1}{2\pi \phi_0^2} \int_0^\infty x dx J_0\left(x \frac{\phi}{\phi_0}\right) \exp(-x^2) \left( 1 + \frac{11x^4}{496N} \left( \frac{M_{\text{Max}}}{M_{\text{Min}}} \right)^{\frac{9}{10}} \right) \\ &\approx \frac{\exp(-\frac{\phi^2}{4\phi_0^2})}{4\pi \phi_0^2} \left[ 1 + \frac{0.06}{N} \left( \frac{M_{\text{Max}}}{M_{\text{Min}}} \right)^{\frac{9}{10}} - \frac{0.03\phi^2}{N\phi_0^2} \left( \frac{M_{\text{Max}}}{M_{\text{Min}}} \right)^{\frac{9}{10}} + \frac{0.004\phi^4}{N\phi_0^4} \left( \frac{M_{\text{Max}}}{M_{\text{Min}}} \right)^{\frac{9}{10}} \right], \end{aligned}$$

Where in the second step the change of variable  $x = k\phi_0$  was conducted. While the above result only holds approximately, it proposes a range for when the Gaussian description starts breaking down. Particularly setting the third term equal to<sup>3</sup>  $\frac{1}{4}$ , then we may extrapolate a value by solving for  $\phi$ :

$$\phi_{\text{cut}} \approx \left[ 8.33 \phi_0^2 N \left( \frac{M_{\text{Min}}}{M_{\text{Max}}} \right)^{\frac{9}{10}} \right]^{\frac{1}{2}} \approx \left( \frac{4G}{c^2} \right) \frac{1.76 N M_{\text{Max}}^{\frac{1}{10}} M_{\text{Min}}^{\frac{9}{10}}}{R}, \quad (4.1.16)$$

where  $\phi_0^2 = \frac{45}{121} N \phi_{\text{Min}}^2 \left( \frac{M_{\text{Max}}}{M_{\text{Min}}} \right)^{\frac{11}{10}}$ .

<sup>3</sup>The value of  $\frac{1}{4}$  is maybe a bit ad-hoc. It was chosen because it seems to fit well with the simulations. Any reasonable value should however give a fair order of magnitude estimation. The importance of the below equation however is the scaling of the cut-off and not the particular position of the actual cut-off. Therefore this is not a very pressing problem.

I have tested this formula for four different combinations of  $M_{\text{Min}}$ ,  $M_{\text{Max}}$ ,  $R$  and  $N$  in a simulation of the ratio probability distribution. The results are showcased in Figure 4.2. The values in the legend have been used to find the cut-off using the equation (4.1.16) and then only the bins within this cut-off have been used to fit the displayed Gaussians. All of the fits look fine, however, there might be a tendency for some of the Gaussians to be wider than they should be, especially the last two. The cut-off equation itself seems to agree well with the simulation results and serves as a decent estimate for the location of the different cut-offs. However, far more importantly, the cut-off does seem to scale according to the equation above, as seen by the vastly different parameter combinations.

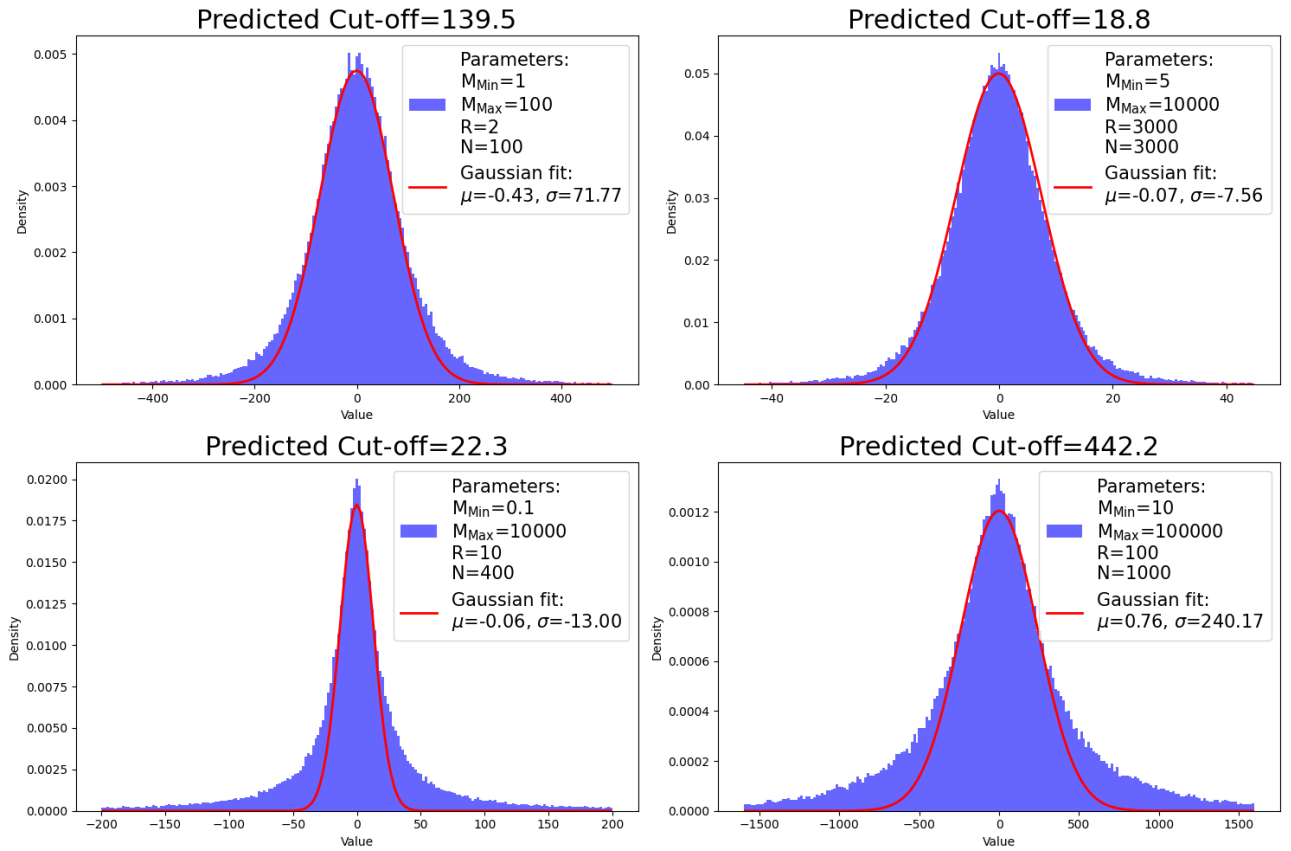


**Figure 4.2:** A simulation using the impact parameter distribution and mass spectrum distribution from the previous section has been used for various combinations of  $M_{\text{Min}}$ ,  $M_{\text{Max}}$ ,  $R$  and  $N$ . All of the histograms include  $10^6$  samples. For the predicted cut-off a Gaussian has been fitted to all of the bins that lie within the cut-off. As can be seen from the plots this seems to match the Gaussian behaviour for small deflection very well.

The above analysis only works in the regime, where  $N\left(\frac{M_{\text{Min}}}{M_{\text{Max}}}\right)^{\beta-1} \lesssim 1$ , so it cannot be extrapolated far beyond this region. However, the fact that the cut-off is very weakly dependent on  $M_{\text{Max}}$  suggests that as long as  $N\left(\frac{M_{\text{Min}}}{M_{\text{Max}}}\right)^{\beta-1}$  stays small, then there is not

much difference in the cut-off even if  $M_{\text{Max}}$  is changed by orders of magnitudes. This tells exactly that the larger masses may not be expected to contribute much to the diffuse (Gaussian) part of  $P_N(\phi)$ . Extrapolating this then means an effective upper bound,  $M_*$ , should be picked when working in the high-optical depth case, so as to not overestimate the total deflection.

To put the above consideration into context. Dark matter subhalos may get as heavy as  $10^{11} - 10^{12} M_\odot$ , but the amount of these subhalos is quite limited. It is therefore extremely unlikely that such large subhalos should contribute to the diffuse microlensing component. Using the above argument, it can therefore be assumed that the actually relevant subhalos might have lower masses than  $M_{\text{Max}}$ . Using the values from Springel *et al.* [34], then  $N \sim \frac{10}{9} \frac{a_0 m_0^{1.9}}{M_{\text{Min}}^{0.9}}$ , which means:

$$N \left( \frac{M_{\text{Min}}}{M_{\text{Max}}} \right)^{0.9} = \frac{10}{9} \frac{a_0 m_0^{1.9}}{M_{\text{Max}}^{0.9}} \approx 4.2 \cdot 10^9 \left( \frac{M_\odot}{M_{\text{Max}}} \right)^{0.9}, \quad (4.1.17)$$

this therefore seems to suggest the highest relevant subhalos for high-optical depth microlensing have masses around  $M_{\text{eff}} = 10^9 - 10^{10} M_\odot$ . This will significantly impact the results, as microlensing in the previous section was shown to depend on  $N \langle M^2 \rangle$ , which is solely determined by the largest masses. Consequently, microlensing would not be as pronounced as it would be if the mass spectrum were directly inserted into the random star field model.

### 4.1.3 The high N-behaviour

For large  $N$  it will not, in general, be possible to assume  $N \left( \frac{M_{\text{Min}}}{M_{\text{Max}}} \right)^{\beta-1} < 1$ . Therefore the contribution of  $\tilde{\rho}_2$  to  $\tilde{\rho}_N$  has to be taken into account. Since  $\tilde{\rho}_N$  is described by a binomial distribution, then for large  $N$ , it can be approximated using a normal distribution:

$$\tilde{\rho}_N = \int dn \frac{\exp\left(-\frac{(n-\mu)^2}{2\sigma^2}\right)}{\sqrt{2\pi\sigma^2}} [\tilde{\rho}_1]^n [\tilde{\rho}_2]^{N-n} \quad \mu = N(1-p), \sigma^2 = Np(1-p) \quad (4.1.18)$$

To compute the above integral the two characteristic functions have to be found, where  $\tilde{\rho}_2$  has to be properly normalized:

$$\tilde{\rho}_1 \approx 1 - c^2 \frac{45}{121} \left( \frac{M_{\text{Max}}}{M_{\text{Min}}} \right)^{\frac{11}{10}} + o(c^4) \quad (4.1.19)$$

$$\tilde{\rho}_{2,\text{norm.}} = \frac{\tilde{\rho}_2}{I_2} \approx \left[ 1 - \frac{c^2}{2} \left( \frac{M_{\text{Max}}}{M_{\text{Min}}} \right)^2 \log \left( \frac{3.05}{c} \frac{M_{\text{Min}}}{M_{\text{Max}}} \right) \right] + o(c^4). \quad (4.1.20)$$

I will drop the subscript for  $\tilde{\rho}_{2,\text{norm.}}$  and just call it  $\tilde{\rho}_2$  from now on. Using the relation  $\log(1+x) \approx x$ , then we may write:

$$\begin{aligned}\tilde{\rho}_N &= [\tilde{\rho}_1]^n [\tilde{\rho}_2]^{N-n} \approx \exp \left[ n \log(\tilde{\rho}_1) + (N-n) \log(\tilde{\rho}_2) \right] \\ &= \exp \left[ -nc^2 \frac{45}{121} \left( \frac{M_{\text{Max}}}{M_{\text{Min}}} \right)^{\frac{11}{10}} - (N-n) \left( \frac{c^2}{2} \left( \frac{M_{\text{Max}}}{M_{\text{Min}}} \right)^2 \log \left( \frac{3.05}{c} \frac{M_{\text{Min}}}{M_{\text{Max}}} \right) \right) \right] \\ &= \exp \left[ -An - B(N-n) \right],\end{aligned}$$

Finally this allows for the calculation of  $\tilde{\rho}_N$  by inserting the above expression into the Gaussian integral:

$$\tilde{\rho}_N = \exp \left[ \frac{(A-B)^2 \sigma^2}{2} \right] \exp \left[ -A\mu - B(N-\mu) \right]. \quad (4.1.21)$$

$\mu$  and  $\sigma$  can be expressed in terms of  $N$  and  $p$ . Now  $q = 1 - p$  with  $p = \frac{\beta-1}{3-\beta} \left( \frac{M_{\text{Min}}}{M_{\text{Max}}} \right)^{\beta-1}$  and so it can be assumed that  $p^2 \approx 0$ . This means the above expression can be simplified into:

$$\tilde{\rho}_N = \exp \left[ \frac{(A-B)^2 Np}{2} \right] \exp \left[ -AN(1-p) - BNp \right]. \quad (4.1.22)$$

For completion the calculation for this is included in the appendix, however, it is unclear whether it is of much use. Interestingly, to leading order, it seems to predict a Gaussian with a slightly larger standard deviation than the random star-field. This however is not a very large effect, so it can most likely be ignored. It does however seem to stem from the discreteness of the distribution. This can be seen as the expression from Katz *et al.* [21] shows up in the limit  $N \rightarrow \infty$ , as would also be expected. In this case, you may argue that the contributions from  $\tilde{\rho}_1$  become non-leading due to the logarithm in  $\tilde{\rho}_2$ . As such if we completely ignore the contribution from  $\tilde{\rho}_1$  we will end up with (setting  $\beta = 1.9$ ):

$$\begin{aligned}\tilde{\rho}_N &\approx \exp \left[ -B(N-\mu) \right] = \exp \left[ -N \frac{c^2}{2} \frac{9}{11} \left( \frac{M_{\text{Max}}}{M_{\text{Min}}} \right)^{\frac{11}{10}} \log \left( \frac{3.05}{c} \frac{M_{\text{Min}}}{M_{\text{Max}}} \right) \right] \\ &= \exp \left[ -N \frac{c^2}{2} \frac{\langle M^2 \rangle}{M_{\text{Min}}^2} \log \left( \frac{3.05}{c} \frac{M_{\text{Min}}}{M_{\text{Max}}} \right) \right] = \exp \left[ -\frac{x^2}{2} \log \left( \frac{3.05 N^{\frac{1}{2}} \langle M^2 \rangle^{\frac{1}{2}}}{x M_{\text{Min}}} \frac{M_{\text{Min}}}{M_{\text{Max}}} \right) \right] \\ &= \exp \left[ -\frac{x^2}{2} \log \left( \frac{3.05 f N^{\frac{1}{2}}}{x} \right) \right],\end{aligned}$$

where  $f = \frac{\langle M^2 \rangle^{\frac{1}{2}}}{M_{\text{Max}}}$ . Therefore this is exactly the result from Katz *et al.* [21]. This makes sense, since in the limit  $N \rightarrow \infty$  all discreteness of the problem is removed and thus we would expect to recover the result from the random star-field.



## 4.2 Non-uniformity of impact parameter distribution

As was noted when deriving the scattering probability function,  $P(x)$ , in the ratio distribution formalism (4.1.7), the impact parameter distribution barely matters for the small mass perturbers. This is because the regime  $x \leq \frac{M_{\text{Max}}}{M_{\text{Min}}}$  is mostly comprised of variations in the mass distribution, due to the unlikeliness that a small mass perturber is projected close enough to the LOS to make up for its small mass. This however starts changing if the impact parameter distribution is made less steep. In particular, if it becomes somewhat similar, in terms of steepness, to the mass distribution then suddenly the small mass perturbers play a much larger role. To see this in the original framework of Katz *et al.* [21], we only have to change one assumption. The primary assumption they had when building the probability distribution  $P(\phi)$  is that the perturbers are placed uniformly around the LOS within the area  $\pi R^2$ . In order for this to occur the amount of perturbers placed within the area  $\pi b^2$  has to match the area ratio  $\frac{b^2}{R^2}$ . This therefore exactly describes how their CDF of the impact parameter distribution behaves.

The simplest way to try and produce a non-uniform placement of the perturbers is to follow the exact procedure from before but this time consider the ratio  $\left(\frac{b}{R}\right)^n$ . From the perspective of the LOS, then we know that  $n = 2$  means that the perturbers will be placed uniformly around the LOS within the area  $\pi R^2$ . It then follows that, depending on the value of  $n$ , this will either push an abundance of the perturbers toward the LOS or push an abundance of them away. In the case where  $n < 2$ , then we have an abundance of perturbers closer to the LOS, while the opposite is true when  $n > 2$ . This should be somewhat reminiscent of the discussion of the power spectrum back in chapter one. Following the procedure laid out in the microlensing section, then the cumulative distribution function can be found as:

$$F(b) = \left(\frac{b}{R}\right)^n = \left(\frac{\phi_{\text{Min}}}{\phi}\right)^n, \quad (4.2.1)$$

in which case  $P(\phi)$  can be written as:

$$P(\phi) = \frac{n\phi_{\text{Min}}^n}{\phi^{n+1}}. \quad (4.2.2)$$

This eventually leads to the calculation of the following integral:

$$\tilde{\rho}_1 = n \int_1^\infty dx \frac{J_0(ax)}{x^{n+1}} \approx \begin{cases} 1 + c_0 a^n \log(a) + c_2 a^2 + o(a^3) & n \text{ even} \\ 1 + c_1 a^n + c_2 a^2 + o(a^3) & n \text{ odd} \end{cases}, \quad (4.2.3)$$

where  $n$  is an integer. The above integral can be done analytically, but here it is Taylor expanded, as we recall the smallest power in  $a$  will play the most significant role in the description of small deflections. For  $n > 2$  we can immediately see that the leading term will always be  $a^2$ . This  $a^2$ -term is responsible for the Gaussian deflection and so it is no wonder that this shows up for all the distributions with finite variance, since according to the central limit theorem, these should always become Gaussian given enough samples. Now the values of  $n < 2$  are somewhat more interesting, as these suggest that the deflections should not become Gaussians. This ends up fundamentally changing the dependence on the mass distribution as well. This can be seen by finding the characteristic function  $\tilde{\rho}_N$  to leading order:

$$\tilde{\rho}_N = \exp \left[ - \int dM n(M) \frac{c_1 \phi_{\text{Min}}^n k^n}{2} \right]. \quad (4.2.4)$$

This is in particular sensitive to the mass moment:

$$N \langle M^n \rangle = \int_{M_{\text{Min}}}^{M_{\text{Max}}} n(M) M^n dM = m_* \left( \frac{M_{\text{Max}}^{n-0.9} - M_{\text{Min}}^{n-0.9}}{n - 0.9} \right). \quad (4.2.5)$$

Anything sensitive to  $N \langle M \rangle$  is interesting in terms of subhalos since this quantity is not immediately known in simulations [10]. It could therefore, for instance, be used to test the accuracy of these simulations. Additionally, if  $n \sim 1$ , then the dependence on the lower bound of the mass spectrum also starts creeping in. This would also have implications in terms of subhalos, since it could help distinguish between different dark matter models. This difference is however small for  $n = 1$  and sits somewhere around a factor  $\sim 1.3$  depending on  $M_{\text{Max}}$  and  $M_{\text{Min, WDM}}$ .

It should be noted that, although this analysis has only been done for integer values of  $n$ , it can in principle be extended to any positive real number. The reason it was only done for integers is because it looks cleaner and expresses the same points.

Now let's assume  $n = 1$ . In this case, the deflection probability  $P_N(\phi)$  can actually be found:

$$P_N(\phi) = \frac{1}{2\pi\phi_0} \int_0^\infty x dx J_0\left(x \frac{\phi}{\phi_0}\right) \exp\left(-\frac{x}{2}\right) \quad , \quad \phi_0 = c_1 \frac{4G}{c^2} \frac{N\langle M \rangle}{R}, \quad (4.2.6)$$

This in particular has the solution:

$$P_N(\phi) = \frac{1}{2\pi} \frac{4\phi_0^2}{(4\phi_0^2 + \phi^2)^{\frac{3}{2}}}. \quad (4.2.7)$$

The above probability density function is somewhat similar to a 3-dimensional Cauchy distribution. For  $\phi \lesssim \phi_0$  it behaves much like a Gaussian with standard deviation  $\sigma^2 = 2\phi_0$ . However, as expected, its tail behaviour is vastly different and does not behave like a Gaussian due to the breakdown of the central limit theorem. Since we only care about the high optical depth limit, then we can to a very good approximation assume the probability density function  $P_N(\phi)$  is a Gaussian with standard deviation  $\sigma^2 = 2\phi_0$ . In this case, the dependence on the surface brightness fluctuations is dependent on microlensing through  $\sigma^2$ . This therefore leads to an observable, which is directly dependent on  $N\langle M \rangle$ . Interestingly, this also suggests the strength of high-optical depth microlensing will be smaller:

$$\frac{\sigma_{n=1}}{\sigma_{\text{uniform}}} \propto \sqrt{\frac{\langle M \rangle^2}{\langle M^2 \rangle}} \leq 1 \quad (4.2.8)$$

On the other hand, the chance to undergo low-optical depth microlensing will actually grow, due to the larger tails of (4.2.6). An interesting way to test the non-uniformity could therefore be to experimentally assess the rarity of low-optical depth microlensing events.

The importance of this section is naturally predicated on whether non-uniformity actually plays a role in experimental observations. While this may not be the case, then it still remains an interesting takeaway that non-uniformity could lead to potentially exciting observables.

## 4.3 An order of magnitude estimation of substructure microlensing

From the previous chapter on microlensing, we know the strength of microlensing is encapsulated in the ratio  $\frac{\sigma_{\text{ML}}}{\sigma_{\text{W}}}$ . In this case  $\sigma_{\text{W}}$  is the apparent size of the source, whereas  $\sigma_{\text{ML}}$  pertains solely to the microlensing strength of the star-field/halo-field.

The strongest microlensing effect is therefore seen if the size of the source is small and far away. This naturally leads us to consider Quasars, which are the brightest sources at high redshift and also have a significantly smaller apparent size than galaxies. In their paper Deguchi and Watson [12] states a realistic value of the apparent size of a source could be  $\sigma_{\text{W}} = 0.1\text{mas}$ . If we assume a distance to the source on the order of Gpc, then we can approximate the apparent size as:

$$\sigma_{\text{W}} \sim 3.0 \times 10^{18} \text{ cm} \times \left( \frac{D_s}{\text{Gpc}} \right) \quad (4.3.1)$$

Let's assume the lens is placed at the midpoint between the source and the observer. If this is the case, then the effective distance can be approximated<sup>4</sup> as merely  $D = \frac{1}{2}D_s$ . Assuming the values specified in the parenthesis, the microlensing standard deviation is given by (3.2.5):

$$\begin{aligned} \sigma_{\text{ML, stars}} &= 5.3 \times 10^{16} \text{ cm} \times \left( \frac{M_{\text{Max}}}{100 \text{ M}_{\odot}} \right)^{\frac{11}{20}} \left( \frac{R_{\text{Gal}}}{20 \text{ kpc}} \right)^{-1} \left( \frac{N}{1 \times 10^{11}} \right)^{\frac{1}{2}} \left( \frac{D}{0.5 \text{ Gpc}} \right) \\ \sigma_{\text{ML, subhalo}} &= 2.9 \times 10^{19} \text{ cm} \times \left( \frac{M_{\text{Max}}}{10^9 \text{ M}_{\odot}} \right)^{\frac{11}{20}} \left( \frac{R_{\text{Halo}}}{200 \text{ kpc}} \right)^{-1} \left( \frac{m_0}{2.75 \times 10^7 \text{ M}_{\odot}} \right)^{\frac{19}{20}} \\ &\quad \times \left( \frac{a_0}{3.26 \times 10^{-5} \text{ M}_{\odot}^{-1}} \right)^{\frac{1}{2}} \left( \frac{D}{0.5 \text{ Gpc}} \right), \end{aligned}$$

with  $a_0$  and  $m_0$  given by the paper Springel *et al.* [34] and I chose the smallest value of  $M_{\text{Max}}$  that was argued in section 4.1.2. The squared ratios  $(\frac{\sigma_{\text{ML}}^2}{\sigma_{\text{W}}^2})$  consequently become:

$$\text{Stars:} \quad \sim 3.2 \cdot 10^{-4} \quad (4.3.2)$$

$$\text{Subhalos:} \quad \sim 84 \quad (4.3.3)$$

<sup>4</sup>This is not true due to the curvature of spacetime. However, as an order of magnitude estimate, this should be an okay approximation

According to these numbers, the high-optical depth microlensing by subhalos should be a hundred thousand times as powerful as by stars. The model constructed here therefore unequivocally tells us that subhalos are expected to dominate high-optical depth microlensing. While it may be that the effect is exaggerated in this model due to potentially troubling assumptions, see the discussion, then it suggests the study of substructure through the lens of high optical depth microlensing is very warranted.

# Discussion and outlook

The previous section discussed what should be considered when attempting to extend the microlensing model to include microlensing by substructure. It was noticed how, due to the wide and steep nature of the mass spectrum, we can likely exclude the largest subhalos from our mass spectrum. This was done on purely statistical grounds, but it can also be argued from a physics point of view. Since there are only expected to be very few of the largest subhalos in a given galaxy, then these are also the least randomly placed. It therefore stands to reason that these should not appear in the stochastic part of the lens equation. In case they have a significant impact on the deflection, they should instead be incorporated into the main lens.

However, even if the largest subhalos do not contribute to microlensing, it was still determined that microlensing by subhalos should be significantly stronger than microlensing by stars. This is one of the main results of this thesis and ideally, it should be tested by simulations. If time had permitted a more thorough investigation, then ray-tracing techniques would have been brought out to test the model as a whole. This could in particular grant insight into, whether some of the simplifying assumptions made in this thesis are actually physically correct. These assumptions include:

- Disregarding that dark matter subhalos should be distributed across a broader segment of the light trajectory. This assumption was particularly made in section 2.3, where it was assumed that all perturbers could be put into the same lens plane.
- Disregarding possible correlation between impact parameter distribution and the mass distribution.
- Disregarding the actual physical extent of subhalos. This assumption is implicitly made when using the random star-field as a template for a substructure lensing model.

Accounting for any of these effects in an analytical model poses significant challenges. The first one undoubtedly introduces non-linearity into the problem. While the last

two likely require the deflection probabilities to be made more sophisticated. These effects are therefore most suited to be studied through simulations. Nevertheless, we will proceed to try and address each of these issues, starting with the third.

An attempt at addressing the problem of the physical extent of perturbers was actually tried during the project. This was put into the appendix in order to showcase the conclusion drawn from it. In short, it proposed to dampen the deflection if the light ever entered into the perimeter of the substructure. Effectively, this made an upper bound on the size of all deflections, which meant a Gaussian probability function,  $P_N(\phi)$ , was expected by the central limit theorem. It seems however that the chance to enter into the perimeter of the substructure is such a rare event that it isn't expected to affect high-optical depth microlensing at all. The extent of the substructure therefore appears to primarily influence low-optical depth microlensing, and as such, it does not seem to be a large issue to neglect it in our case. This also makes physical sense, we would expect the point-mass approximation to be decent, as long as all perturbers are situated far enough away from the line of sight.

The second assumption could potentially introduce some very interesting effects. In particular, if it is the case that larger halos typically are further away from the line-of-sight, then this would make the smaller subhalos have a larger contribution to the total deflection and subsequently the magnification. This is somewhat analogous to why a less steep impact parameter distribution places greater emphasis on the smaller subhalos discussed in section 4.2. However if the inverse was found to be true, then it would likely cement that the largest subhalos completely dominate the deflection. This is already the case when perturbers are spread uniformly around the line-of-sight, but in this case, it would likely also extend to non-uniform distributions. As a result, it would probably negate any minor mass dependencies identified in the study of non-uniformity. Insights into such correlations would have to be found in dark matter simulations. Therefore an interesting avenue to pursue would be to learn if such correlations existed and then, if they did, try to include it in the model. Although incorporating a correlation between the impact parameter and the mass spectrum in the original approach by Katz *et al.* [21] appears challenging, it may be feasible using the ratio-distribution formalism introduced in section 4.1. This presents a promising direction for possible extensions of this work.

Finally, the first assumption, I consider this the most pressing issue. Subhalos are spread out in a much larger volume than stars. This was addressed in the previous section by merely picking a larger value for  $R$  (the characteristic impact parameter). This might

however not account for all of the effects. For microlensing by stars assuming that all deflections occur in the same plane is a reasonable approximation, as stars are expected to be contained within the galaxy, which is small compared to the light's trajectory from distant quasars. However, in the case of dark matter, subhalos are not restricted to the galaxy but can occupy a much larger region. This implies that a deflection by a subhalo occurring early (or late) in the light's trajectory could have a significantly greater impact on the overall deflection than our model suggests. Especially, if that subhalo was heavy and thus made a large deflection. The exact extent of the physical effect this introduces remains uncertain. However, this is likely the most important thing to be checked by a ray-tracing simulation.

Another related thing worth discussing is what the characteristic impact parameter  $R$  should be for the star-field and halo-field. Since it is known that galaxies are much denser at their core, then it might, for instance, be unfair, to set  $R$  as the radius of the galaxy itself. It likely should be smaller, which would make microlensing by stars and subhalos slightly more comparable. In this way, it might be important to understand the mass distribution of the galaxy or the halo itself to assess, which value of  $R$  makes the most sense in either situation. Investigating this could also help clarify whether non-uniformity plays a significant role, making it a subject worth further exploration.



# Appendix

## 6.1 The ratio-distribution deflection function for any N

We want to simplify the expression:

$$\tilde{\rho}_N = \exp \left[ \frac{(A - B)^2 N p}{2} \right] \exp \left[ -AN(1 - p) - BNp \right], \quad (6.1.1)$$

where:

$$A = \frac{45}{121} c^2 b^{\frac{11}{10}}, \quad B = \frac{c^2}{2} b^2 \log\left(\frac{3.05}{cb}\right), \quad p = \frac{9}{11} b^{-0.9}$$

and it has been defined that  $b = \left(\frac{M_{\text{Max}}}{M_{\text{Min}}}\right)$ . Since  $b \gg 1$ , then this can be used to simplify the coming expressions:

$$\begin{aligned} (A - B)^2 &= A^2 + B^2 - 2AB \\ &= c^4 b^{2.2} \left(\frac{2025}{14641}\right) + \frac{c^4}{4} b^4 \log\left(\frac{3.05}{cb}\right)^2 - \frac{45}{121} c^2 b^{\frac{11}{10}} \log\left(\frac{3.05}{cb}\right) \\ &\approx \frac{c^4}{4} b^4 \log\left(\frac{3.05}{cb}\right)^2 - \frac{45}{121} c^2 b^{\frac{11}{10}} \log\left(\frac{3.05}{cb}\right) \end{aligned}$$

Adding this into the expression for  $\tilde{\rho}_N$  gives:

$$\begin{aligned} \tilde{\rho}_N &\approx \exp \left( -N \left[ -\frac{9}{11} \frac{c^4}{4} b^{3.1} \log\left(\frac{3.05}{cb}\right)^2 + c^2 b^{1.1} \log\left(\frac{3.05}{cb}\right) \frac{405}{1331} + \frac{45}{121} c^2 b^{1.1} + \frac{9}{11} \frac{c^2}{2} b^{1.1} \log\left(\frac{3.05}{cb}\right) \right] \right) \\ &= \exp \left( -N \left[ \frac{c^2}{2} b^{1.1} \left( \frac{1899}{1331} \log\left(\frac{3.05}{cb}\right) + \frac{90}{121} \right) - \frac{9}{11} \frac{c^4}{4} b^{3.1} \log\left(\frac{3.05}{cb}\right)^2 \right] \right) \\ &= \exp \left( -N \left[ \frac{c^2}{2} b^{1.1} \frac{1899}{1331} \log\left(\frac{6.41}{cb}\right) - \frac{9}{11} \frac{c^4}{4} b^{3.1} \log\left(\frac{3.05}{cb}\right)^2 \right] \right) \\ &= \exp \left( -N \left[ \frac{k^2}{2} \langle M^2 \rangle \frac{211}{121} \log\left(\frac{6.41}{cb}\right) - \frac{31}{11} \frac{k^4 \langle M^4 \rangle}{4} \log\left(\frac{3.05}{cb}\right)^2 \right] \right), \end{aligned}$$

where it was used that:

$$\langle M^2 \rangle = \frac{9}{11} M_{\text{Min}}^{0.9} M_{\text{Max}}^{1.1} \quad , \quad \langle M^4 \rangle = \frac{9}{31} M_{\text{Min}}^{0.9} M_{\text{Max}}^{3.1}$$

Interestingly, the result for  $\tilde{\rho}_N$  includes a fourth order term.

## 6.2 Extended substructure lensing

We consider some galaxy with radius 'R'. As a light ray moves, from some distant source, through the galaxy it will be scattered by all the structure within that galaxy. Following the procedure of Katz *et al.* [21], we need to determine the probability to deflect with the angle  $\phi$ ,  $P(\phi)$ . It will now be argued why the following expression

$$P(\phi) = \begin{cases} \frac{\phi_{\text{Min}}^2}{\phi_E^2} \delta(\phi - \phi_H) + \frac{2\phi_{\text{Min}}^2}{\phi^3} H(\phi - \phi_E) & (\phi \geq \phi_{\text{Min}}) \\ 0 & (\phi < \phi_{\text{Min}}) \end{cases}, \quad (6.2.1)$$

should be considered a generalization of eq.1 from Katz *et al.* [21] to extended objects.

- First we note that the eq. 1 from K86 is obtained by sending  $\phi_E \rightarrow \infty$ . This is a necessary requirement, since  $\phi_E \propto 1/R_E$ , so when  $R_E \rightarrow 0$  then this should mean we were looking at point masses, as in K86.
- Second, outside the radius of an extended object, it can be taken to be a point mass according to the shell theorem. Therefore, whenever  $\phi \leq \phi_E$ , we would expect the expression from K86 to hold. This is why the second term has a step-function attached. Inside the object, the deflection angle is taken to be that of the singular isothermal sphere, constant. Therefore it will always deflect with  $\phi_H$ .
- Third, the probability of being inside a sphere should be  $\frac{R_E^2}{R^2} = \frac{\phi_{\text{Min}}^2}{\phi_E^2}$ . This is the reason for the constant in front of the first term.
- Finally, it can be shown that  $\int P_1(\phi) d\phi = 1$ , as one would expect for a PDF.

## 6.2.1 Fourier transform

It can be shown quite simply that:

$$\begin{aligned} \int_1^{\frac{\phi_E}{\phi_{\text{Min}}}} \frac{J_0(cx)}{x} dx &= \log\left(\frac{\phi_E}{\phi_{\text{Min}}}\right) + \sum_{m=1}^{\infty} \frac{(-1)^m \left(\frac{c}{2} \frac{\phi_E}{\phi_{\text{Min}}}\right)^{2m}}{2m(m!)^2} - \sum_{m=1}^{\infty} \frac{(-1)^m \left(\frac{c}{2}\right)^{2m}}{2m(m!)^2} \\ &= \log\left(\frac{\phi_E}{\phi_{\text{Min}}}\right) + \sum_{m=1}^{\infty} \frac{(-1)^m \left(\frac{c}{2}\right)^{2m} \left(\left(\frac{\phi_E}{\phi_{\text{Min}}}\right)^{2m} - 1\right)}{2m(m!)^2}. \end{aligned}$$

It then will hold in the limit  $\phi_E \rightarrow \infty$ :

$$\lim_{\phi_E \rightarrow \infty} \left( \log\left(\frac{\phi_E}{\phi_{\text{Min}}}\right) + \sum_{m=1}^{\infty} \frac{(-1)^m \left(\frac{c}{2}\right)^{2m} \left(\left(\frac{\phi_E}{\phi_{\text{Min}}}\right)^{2m} - 1\right)}{2m(m!)^2} \right) = -\gamma + \log\left(\frac{2}{c}\right) - \sum_{m=1}^{\infty} \frac{(-1)^m \left(\frac{c}{2}\right)^{2m}}{2m(m!)^2}.$$

Now we have to do the same integration by parts as Katz *et al.* [21], but here there is going to be a few boundary terms that can't be neglected. So we have:

$$\begin{aligned} \int_1^{\frac{\phi_E}{\phi_{\text{Min}}}} \frac{J_0(cx)}{x^3} dx &= \left[ -\frac{J_0(cx)}{2x^2} \right]_1^{\frac{\phi_E}{\phi_{\text{Min}}}} + \int_1^{\frac{\phi_E}{\phi_{\text{Min}}}} dx \frac{J_0'(cx)}{2x^2} \\ &= \frac{-J_0(c \frac{\phi_E}{\phi_{\text{Min}}})}{2(\frac{\phi_E}{\phi_{\text{Min}}})^2} + \frac{J_0(c)}{2} - \frac{c}{2} \int_1^{\frac{\phi_E}{\phi_{\text{Min}}}} dx \frac{J_1(cx)}{x^2} \\ &= \frac{J_0(c)}{2} - \frac{\phi_{\text{Min}}^2}{2\phi_E^2} J_0\left(c \frac{\phi_E}{\phi_{\text{Min}}}\right) - \frac{c}{2} \left[ \left[ \frac{-J_1(cx)}{x} \right]_1^{\frac{\phi_E}{\phi_{\text{Min}}}} + \frac{c}{2} \int_1^{\frac{\phi_E}{\phi_{\text{Min}}}} dx \frac{J_0(cx) - J_2(cx)}{x} \right] \\ &= \frac{J_0(c)}{2} - \frac{cJ_1(c)}{2} - \frac{\phi_{\text{Min}}^2}{2\phi_E^2} J_0\left(c \frac{\phi_E}{\phi_{\text{Min}}}\right) + \frac{c}{2} \frac{\phi_{\text{Min}}}{\phi_E} J_1\left(c \frac{\phi_E}{\phi_{\text{Min}}}\right) \\ &\quad - \frac{c}{4} \left[ \frac{J_1(cx)}{x} \right]_1^{\frac{\phi_E}{\phi_{\text{Min}}}} - \frac{c^2}{4} \int_1^{\frac{\phi_E}{\phi_{\text{Min}}}} dx \frac{J_0(cx)}{x} \\ &= \frac{J_0(c)}{2} - \frac{cJ_1(c)}{4} - \frac{\phi_{\text{Min}}^2}{2\phi_E^2} J_0\left(c \frac{\phi_E}{\phi_{\text{Min}}}\right) + \frac{c}{4} \frac{\phi_{\text{Min}}}{\phi_E} J_1\left(c \frac{\phi_E}{\phi_{\text{Min}}}\right) - \frac{c^2}{4} \int_1^{\frac{\phi_E}{\phi_{\text{Min}}}} dx \frac{J_0(cx)}{x}. \end{aligned}$$

Finally if we set  $\phi_H = \phi_E$ , then the Fourier transform would be:

$$\tilde{\rho}_1 = J_0(c) - \frac{c}{2} \left[ J_1(c) - \frac{\phi_{\text{Min}}}{\phi_E} J_1\left(c \frac{\phi_E}{\phi_{\text{Min}}}\right) \right] - \frac{c^2}{2} \left[ \log\left(\frac{\phi_E}{\phi_{\text{Min}}}\right) + \sum_{m=1}^{\infty} \frac{(-1)^m \left(\frac{c}{2}\right)^{2m} \left(\left(\frac{\phi_E}{\phi_{\text{Min}}}\right)^{2m} - 1\right)}{2m(m!)^2} \right]. \quad (6.2.2)$$

It should also be very clear that (6.2.2) resembles Katz *et al.* [21, eq. 2 and eq. 3], when  $\phi_E \rightarrow \infty$ .

## 6.2.2 Probability density function for N-deflections

In order to turn  $\tilde{\rho}_1$  into a probability density function it first has to be raised to the  $N$ 'th power, giving us  $\tilde{\rho}_N$ . This is done through Taylor-expanding in  $c$ . In order to expand in equation (6.2.2) one has to think about the ratio  $\frac{\phi_E}{\phi_{\text{Min}}}$ . Now it always holds that  $\phi_E > \phi_{\text{Min}}$ , however if  $\phi_E \sim \phi_{\text{Min}}$  (i.e. within a few orders of magnitude), then the argument from Katz et al will permit us to expand in  $a$  without any worries. However, if  $\phi_E \gg \phi_{\text{Min}}$ , then the hypergeometric term in (6.2.2) needs to be accounted for and in this case, we will end up with exact same equation as in Katz et al. So moving forward, we will assume  $\phi_E \sim \phi_{\text{Min}}$ . In this case we have:

$$\tilde{\rho}_1 = 1 - \frac{c^2}{2} \left( \frac{1}{2} + \log\left(\frac{\phi_E}{\phi_{\text{Min}}}\right) \right) + o(c^4). \quad (6.2.3)$$

This will give us:

$$\tilde{\rho}_N = \left[ 1 - \frac{c^2}{2} \left( \frac{1}{2} + \log\left(\frac{\phi_E}{\phi_{\text{Min}}}\right) \right) \right]^N \approx \exp\left(\frac{-Nc^2}{2} \left( \frac{1}{2} + \log\left(\frac{\phi_E}{\phi_{\text{Min}}}\right) \right)\right).$$

Transforming it back gives:

$$\begin{aligned} P_N(\phi) &= \frac{1}{2\pi} \int_0^\infty k dk J_0(k\phi) \exp\left(-\frac{Nk^2\phi_{\text{Min}}^2}{2} \left( \frac{1}{2} + \log\left(\frac{\phi_E}{\phi_{\text{Min}}}\right) \right)\right) \\ &= \frac{1}{2\pi} \int_0^\infty \frac{k}{\phi_0^2} dk J_0\left(\frac{k\phi}{\phi_0}\right) \exp\left(-\frac{k^2}{2} \left( \frac{1}{2} + \log\left(\frac{\phi_E}{\phi_0} N^{\frac{1}{2}}\right) \right)\right) \\ &= \frac{1}{2\pi\phi_0^2 \left( \frac{1}{2} + \log\left(\frac{\phi_E}{\phi_0} N^{\frac{1}{2}}\right) \right)} \exp\left(-\frac{\phi^2}{2\phi_0^2 \left( \frac{1}{2} + \log\left(\frac{\phi_E}{\phi_{\text{Min}}}\right) \right)}\right) \\ &= \frac{1}{2\pi\sigma^2} \exp\left(-\frac{\phi^2}{2\sigma^2}\right) \quad , \quad \sigma^2 = N\phi_{\text{Min}}^2 \left( \frac{1}{2} + \log\left(\frac{\phi_E}{\phi_{\text{Min}}}\right) \right). \end{aligned}$$

So in conclusion:

$$P_N(\phi) = \frac{1}{2\pi\sigma^2} \exp\left(-\frac{\phi^2}{2\sigma^2}\right) \quad , \quad \sigma^2 = N\phi_{\text{Min}}^2 \left( \frac{1}{2} + \log\left(\frac{\phi_E}{\phi_{\text{Min}}}\right) \right). \quad (6.2.4)$$

This result is quite obvious, as it expresses that if there is some upper-limit to the size of our deflections, then we are expected to see a gaussian due to the CLT. It therefore seems that the effects of extended substructure mostly affects low-optical depth microlensing.

# Bibliography

- [1] N. Aghanim, Y. Akrami, M. Ashdown, *et al.* „Planck2018 results: VI. Cosmological parameters“. In: *Astronomy & Astrophysics* 641 (Sept. 2020), A6. DOI: 10.1051/0004-6361/201833910.
- [2] C. Alcock *et al.* „The MACHO project: Microlensing results from 5.7 years of LMC observations“. In: *Astrophys. J.* 542 (2000), pp. 281–307. DOI: 10.1086/309512. arXiv: astro-ph/0001272.
- [3] Matthias Bartelmann and Peter Schneider. „Weak gravitational lensing“. In: *Physics Reports* 340.4–5 (Jan. 2001), pp. 291–472. DOI: 10.1016/s0370-1573(00)00082-x.
- [4] Martin Bauer and Tilman Plehn. *Yet Another Introduction to Dark Matter*. 2018. arXiv: 1705.01987 [hep-ph].
- [5] Daniel Baumann. *Cosmology*. Cambridge University Press, July 2022. DOI: 10.1017/9781108937092.
- [6] Gianfranco Bertone and Dan Hooper. „History of dark matter“. In: *Reviews of Modern Physics* 90.4 (Oct. 2018). DOI: 10.1103/revmodphys.90.045002.
- [7] A. Boyarsky, M. Drewes, T. Lasserre, S. Mertens, and O. Ruchayskiy. „Sterile neutrino Dark Matter“. In: *Progress in Particle and Nuclear Physics* 104 (Jan. 2019), pp. 1–45. DOI: 10.1016/j.ppnp.2018.07.004.
- [8] Sean M. Carroll. *Spacetime and Geometry: An Introduction to General Relativity*. Cambridge University Press, July 2019. DOI: 10.1017/9781108770385.
- [9] S. Chandrasekhar. „Stochastic Problems in Physics and Astronomy“. In: *Rev. Mod. Phys.* 15 (1 Jan. 1943), pp. 1–89. DOI: 10.1103/RevModPhys.15.1.
- [10] E. Contini, G. De Lucia, and S. Borgani. „Statistics of substructures in dark matter haloes: Statistics of substructures in DM haloes“. In: *Monthly Notices of the Royal Astronomical Society* 420.4 (Feb. 2012), pp. 2978–2989. DOI: 10.1111/j.1365-2966.2011.20149.x.
- [11] Liang Dai and Massimo Pascale. *New Approximation of Magnification Statistics for Random Microlensing of Magnified Sources*. 2021. arXiv: 2104.12009 [astro-ph.GA].

- [12] Shuji Deguchi and William D. Watson. „An Analytic Treatment of Gravitational Microlensing for Sources of Finite Size at Large Optical Depths“. In: *ApJ* 335 (Dec. 1988), p. 67. DOI: 10.1086/166906.
- [13] F. W. Dyson, A. S. Eddington, and C. Davidson. „A Determination of the Deflection of Light by the Sun’s Gravitational Field, from Observations Made at the Total Eclipse of May 29, 1919“. In: *Phil. Trans. Roy. Soc. Lond. A* 220 (1920), pp. 291–333. DOI: 10.1098/rsta.1920.0009.
- [14] Elisa G. M. Ferreira. „Ultra-light dark matter“. In: *The Astronomy and Astrophysics Review* 29.1 (Sept. 2021). DOI: 10.1007/s00159-021-00135-6.
- [15] A.L. Fetter and J.D. Walecka. *Theoretical Mechanics of Particles and Continua*. Dover Books on Physics. Dover Publications, 2003.
- [16] Pierre Fleury, Julien Larena, and Jean-Philippe Uzan. „Line-of-sight effects in strong gravitational lensing“. In: *Journal of Cosmology and Astroparticle Physics* 2021.08 (Aug. 2021), p. 024. DOI: 10.1088/1475-7516/2021/08/024.
- [17] K. Freese. „Review of Observational Evidence for Dark Matter in the Universe and in upcoming searches for Dark Stars“. In: *EAS Publications Series* 36 (2009), pp. 113–126. DOI: 10.1051/eas/0936016.
- [18] C.S. Frenk and S.D.M. White. „Dark matter and cosmic structure“. In: *Annalen der Physik* 524.9–10 (Sept. 2012), pp. 507–534. DOI: 10.1002/andp.201200212.
- [19] T. Harmark. *General relativity and Cosmology lecture notes*. Niels Bohr insititute. 2021.
- [20] Kimmo Kainulainen and Valerio Marra. „New stochastic approach to cumulative weak lensing“. In: *Physical Review D* 80.12 (Dec. 2009). DOI: 10.1103/physrevd.80.123020.
- [21] N. Katz, S. Balbus, and B. Paczynski. „Random Scattering Approach to Gravitational Microlensing“. In: *ApJ* 306 (July 1986), p. 2. DOI: 10.1086/164313.
- [22] Charles R. Keeton. *Gravitational lensing with stochastic substructure: Effects of the clump mass function and spatial distribution*. 2009. arXiv: 0908.3001 [astro-ph.CO].
- [23] Mariangela Lisanti. „Lectures on Dark Matter Physics“. In: *Theoretical Advanced Study Institute in Elementary Particle Physics: New Frontiers in Fields and Strings*. 2017, pp. 399–446. DOI: 10.1142/9789813149441\_0007. arXiv: 1603.03797 [hep-ph].
- [24] M. Meneghetti. *Introduction to Gravitational Lensing: Lecture scripts*. Published through website. DOI: [https://www.ita.uni-heidelberg.de/~jmerten/misc/meneghetti\\_lensing.pdf](https://www.ita.uni-heidelberg.de/~jmerten/misc/meneghetti_lensing.pdf).

- [25] R. Benton Metcalf and Piero Madau. „Compound Gravitational Lensing as a Probe of Dark Matter Substructure within Galaxy Halos“. In: *The Astrophysical Journal* 563.1 (Dec. 2001), pp. 9–20. DOI: 10.1086/323695.
- [26] Przemek Mróz *et al.* „Microlensing Optical Depth and Event Rate toward the Large Magellanic Cloud Based on 20 yr of OGLE Observations“. In: *Astrophys. J. Suppl.* 273.1 (2024), p. 4. DOI: 10.3847/1538-4365/ad452e. arXiv: 2403.02398 [astro-ph.GA].
- [27] B. Neindorf. „A probability theoretical access to extragalactic microlensing“. In: *A&A* 404 (June 2003), pp. 83–92. DOI: 10.1051/0004-6361:20030098.
- [28] K. A. Olive *et al.* „Review of Particle Physics“. In: *Chin. Phys. C* 38 (2014), p. 090001. DOI: 10.1088/1674-1137/38/9/090001.
- [29] B. Paczynski. „Gravitational Microlensing at Large Optical Depth“. In: *ApJ* 301 (Feb. 1986), p. 503. DOI: 10.1086/163919.
- [30] B. Paczynski. „Gravitational Microlensing by the Galactic Halo“. In: *ApJ* 304 (May 1986), p. 1. DOI: 10.1086/164140.
- [31] K. F. Riley and M. P. Hobson. *Essential Mathematical Methods for the Physical Sciences*. Cambridge University Press, 2011.
- [32] Peter Schneider, Jürgen Ehlers, and Emilio E. Falco. *Gravitational Lenses*. 1992. DOI: 10.1007/978-3-662-03758-4.
- [33] Carolin Seitz and Peter Schneider. „Variability of microlensing light curves I. Autocorrelation method and the calculation of the correlated deflection probability.“ In: *A&A* 288 (Aug. 1994), pp. 1–18.
- [34] V. Springel, J. Wang, M. Vogelsberger, A. Ludlow, A. Jenkins, A. Helmi, J. F. Navarro, C. S. Frenk, and S. D. M. White. „The Aquarius Project: the subhaloes of galactic haloes“. In: *Monthly Notices of the Royal Astronomical Society* 391.4 (2008). DOI: 10.1111/j.1365-2966.2008.14066.x.
- [35] P. Tisserand, L. Le Guillou, C. Afonso, *et al.* „Limits on the Macho content of the Galactic Halo from the EROS-2 Survey of the Magellanic Clouds“. In: *Astronomy & Astrophysics* 469.2 (Apr. 2007), pp. 387–404. DOI: 10.1051/0004-6361:20066017.
- [36] D. Tong. *David Tong — Lectures on Cosmology 3: Structure formation*. Published through website. DOI: <https://www.damtp.cam.ac.uk/user/tong/cosmo/three.pdf>.

- [37] David H. Weinberg, James S. Bullock, Fabio Governato, Rachel Kuzio de Naray, and Annika H. G. Peter. „Cold dark matter: Controversies on small scales“. In: *Proceedings of the National Academy of Sciences* 112.40 (Feb. 2015), pp. 12249–12255. DOI: 10.1073/pnas.1308716112.